Enhanced Nuclear Waste Assay

Thesis submitted in accordance with the requirements of the

University of Liverpool for the degree of

Doctor of Philosophy

by

Kevin Alan Tree

Oliver Lodge Laboratory

June 2019

Contents

List of Figures

List of Tables

Glossary

ADL Agata Detector Library. 43

AGATA The Advanced GAmma Tracking Array. 44

BEGe A sub type of HPGe detectors, a Broad Energy Germanium detector is a high Z, high density semiconductor detector with high resolution covering the energy range of 3keV to 3Mev. 9, 37

BGO Bismuth Germanium Oxide is a high Z, high density scintillation detector with high efficiency. 17, 57

CCFE Culham Centre for Fusion Energy, the UK centre for fusion research including the Joint European Tokomak facility. 17

DCSA Digital Compton Suppression Algorithm - algorithm based technique for Compton suppression. 8

HLW Intermediate Level Waste with an activity level of >4000 Bq/g α, >12000 Bq/g β & γ.. 2

HPGe Germanium detector with high purity in the detector crystal. 8

HRGS High Resolution Gamma Spectroscopy using detectors such as the BEGe. 12

ILW Intermediate Level Waste with an activity level of >4000 Bq/g α, >12000 Bq/g for β & γ.. 2

LLW <4000 Bq/g for α and <12000 Bq/g for β & γ.. 2

LLWR Low Level Waste Repository is the UK storage facility for VLLW and LLW located at Drigg, Cumbria. 7

MDA Minimum Detectable Activity for a detector. 9, 102

NDA Nuclear Decommissioning Authority - a non departmental government body with overall responsibility for sites such as Sellafield and the Low Level Waste Repository. 3

nda Non-Destructive Assay is the assay of materials using non destructive techniques. 6, 14

RM A plot showing the distribution of risetimes in a plane as a function of radial position.. 78

TGS Tomographic Gamma Scan - technique to generate a 3D image of a sample, such as a waste drum, using multiple scans with a HPGe and an attenuation-correction source. 15

VLLW Very Low Level Waste with an activity level of <200 Bq/g. 2

Abstract

The accountancy of all radioactive waste held in the UK continues to present challenges to the Nuclear Industry in terms of the regulatory, verification and international safeguards criteria. Characterisation of radioactive waste is an important part of the accountancy process. Current methods of characterisation include passive and active γ-ray spectroscopy techniques which involve expensive and resource intensive procedures.

This thesis investigates an alternative to mechanical Compton suppression systems that are used to suppress the Compton Continuum in the context of non-destructive assay of radioactive waste using γ-ray spectroscopy. This is achieved by using a single broad energy germanium detector in conjunction with a Digital Compton Suppression Algorithm. The aim is to improve the Minimum Detectable Activity and to negate the use of hardware systems that use mechanical suppression, thereby reducing the overall cost and improving efficiency.

The Digital Compton Suppression Algorithm has been developed with the aid of a theoretical charge signal database. The database was also used to perform electric field and weighting potential simulations. The algorithm was validated against an experimental data set using ^{241}Am and ^{137}Cs sealed sources. As a comparison, further tests were conducted at National Nuclear Laboratory Central Laboratory The results of the validation and comparison experiments show that the Digital Compton Suppression Algorithm has been

successfully developed and that an improvement of (41.0±5) % in the Minimum Detectable Activity of the detector is achieved for the 60 keV peak of ^{241}Am in the presence of a variety of isotopes.

Declaration

DECLARATION I hereby certify that this dissertation constitutes my own product, that where the language of others is set forth, quotation marks so indicate, and that appropriate credit is given where I have used the language, ideas, expressions or writings of another. I declare that the dissertation describes original work that has not previously been presented for the award of any other degree of any institution.

Signed,

Kevin Alan Tree

Acknowledgements

I would to express my thanks my thanks to my supervisory team of Dr Laura Harkness-Brennan and Dr Helen Boston for their continued support and guidance throughout my PhD.

I would also like to thank Dr Carl Unsworth and Dr Dan Judson for their invaluable help and support throughout the work of this thesis and general help in the laboratory. My sincere thanks to my fellow Nuclear Group colleagues for the stimulating discussions and for all the fun we have had in the last four years. Also I thank my friends in the Next Generation Nuclear CDT, in particular, Alex, Daniel, and Lee for their guidance and support.

This thesis work would not have been possible without the help and support provided by Beth Ripper, UK Radioactive Waste Inventory Manager, Nuclear Decommissioning Authority, Dr Gary Bolton and Dr Mark Sarsfield, National Nuclear Laboratory, and Mirion (formerly Canberra UK and Canberra Inc. USA). I would also like to thank ESPRC and Nuclear Decommissioning Authority for their financial support.

Last but not the least, I would like to thank my wife for her support and encouragement throughout the last 7 years, and to my family: my parents, my children my brother and sister for supporting me throughout my studies and my life in general.

Chapter 1

Introduction

Radioactive waste is produced from a number of areas including the operation of nuclear power stations, hospitals, universities, industry, military activities and the decommissioning of nuclear power stations. Many radionuclides can be found in the radioactive waste stream, including: ^{55}Fe, ^{59}Ni, ^{60}Co, ^{90}Sr, ^{137}Cs, $^{238/234}$U and ^{241}Am. These decay towards stability through varying combinations of radioactive decay processes including charged particle and gamma ray emissions. Measurement of these emissions allows for the identification and characterisation of radioactive waste. After characterisation, radioactive waste may then be disposed of according to prescribed methods set out in regulations [1, 2]. The aim of this thesis is to develop an algorithm to improve the characterisation of nuclear waste using gamma ray detectors.

1.1 UK Radioactive Waste

Radioactive waste in the UK is characterised by the level of radioactivity of the waste as defined by legislation [1, 2]. The categories for radioactive waste and the relevant activities of each, are set out as follows [1, 2]:

- **Very Low Level Waste** (VLLW)< 200 Bq/g for alpha, beta and gamma
- **Low Level Waste** (LLW) < 4 kBq/g for alpha and < 12 kBq/g for beta and gamma.
- **Intermediate Level Waste** (ILW) > 4 kBq/g alpha, > 12 kBq/g for beta and gamma without any heat generation.
- **High Level Waste** (HLW) > 4 kBq/g alpha, > 12 kBq/g beta and gamma and heat generating.

It is further classified as being either old or new waste. Old waste originates from legacy or decommissioning activities, whereas new waste is produced by ongoing operations, such as power generation. An outline of the different stages of the nuclear fuel cycle for power generation and the resultant waste stream is shown in Figure 1.1 (adapted from [3]).

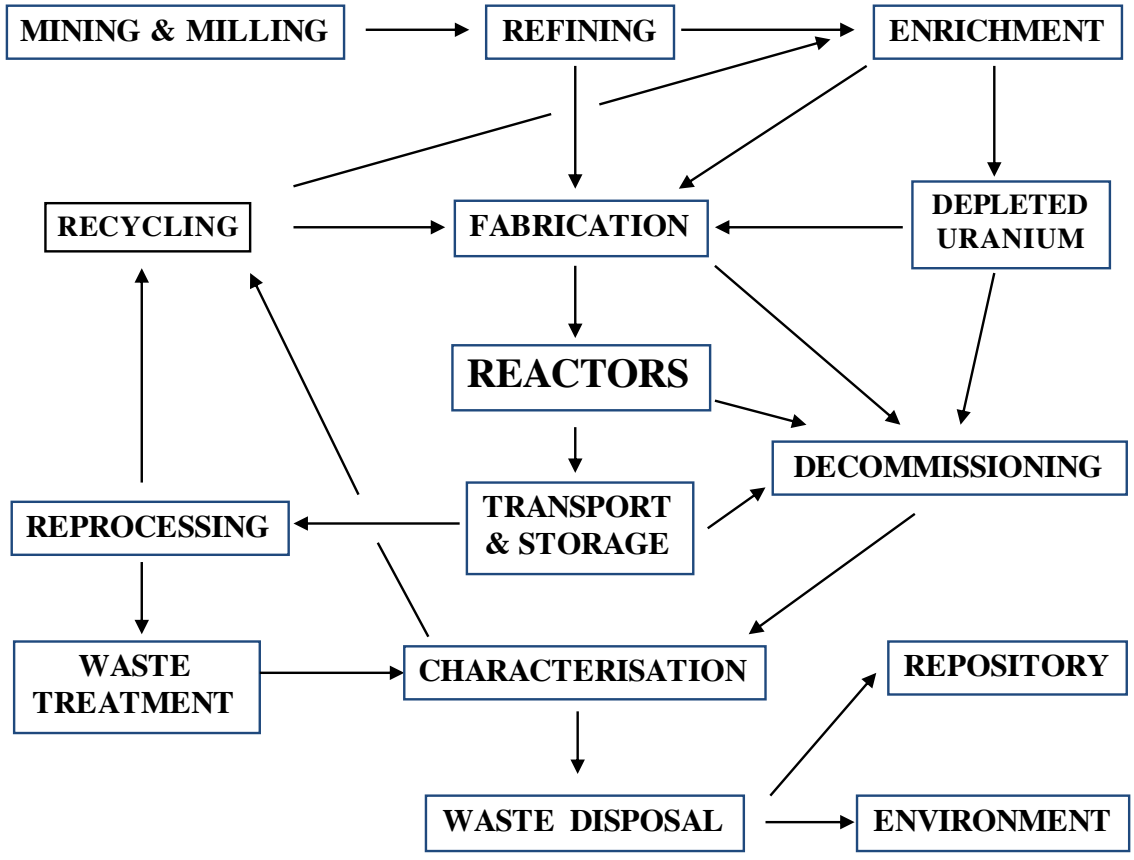

Figure 1.1: Flow chart of the elements of the closed nuclear fuel cycle (adapted from [3]). Characterisation is the focus of this thesis.

The figure shows the sequence of activities needed to manufacture nuclear fuel from uranium ore (refining, enrichment, fuel fabrication), to generate electricity in nuclear reactors and, by reprocessing the spent (i.e. used) fuel, to recycle nuclear materials (uranium, plutonium) for fabricating new fuel. Waste that is not suitable for reprocessing is sent for characterisation and disposal which may be recycling or permanent disposal. Waste from decommissioning activities falls within the remit of the Nuclear Decommissioning Authority (NDA) which is a non-departmental government body of the Department for Business, Energy and Industrial Strategy, formed by the Energy Act 2004. Under the Act the responsibilities of the NDA are defined and include but not limited to:

- Decommissioning and cleaning up of nuclear facilities.
- Ensuring that all waste products, both radioactive and non-radioactive, are safely managed.
- Implementing policy on the long-term management of nuclear waste.
- Developing UK-wide strategy and plans for nuclear Low Level Waste (LLW).
- Scrutinising the decommissioning plans of EDF Energy, who own and operate the fleet of Advanced Gas Cooled Reactor (AGR) nuclear power stations.

The responsibilities held by NDA are delivered through Site Licence Companies, four of which are funded directly from the NDA budget: Dounreay Site Restoration Limited, Low Level Waste Repository Limited, Magnox Limited and Sellafield Limited.

1.2 UK Radioactive Waste Inventory

The NDA maintains the *UK Radioactive Waste & Materials Inventory* (or simply referred to as the Inventory)[4]. The Inventory contains information about radioactive wastes that

Reported volumes and masses					
	HLW[1]	ILW[3]	LLW[4]	VLLW[5]	Totals
Volume (m3)	1080	286000	1370000	2840000	4490000
Mass (tonnes)	2900	310000	1700000	2900000	4900000

[1] HLW conditioned volume and mass do not include waste from reprocessing overseas spent fuel that will be exported to the country of origin, and assume substitution arrangements are implemented.
[2] ILW includes 8,090m^{3}3 (7,000te) of waste that are expected to become LLW as a result of decontamination or decay storage.
[3] LLW includes 32,800m3 (47,000te) held in Vaults 8 and 9 at the LLWR, as well as 33,600m^3 (∼33,600te) previously disposed at Dounreay that is to be retrieved and repackaged. It does not include waste already disposed in the trenches and in Vault 8 at the LLWR.
[4] LLW includes 227,000m^3 (370,000te) of mixed VLLW/LLW at Springfields.
[5] Includes 2,760,000m^3 (2,760,00te) from facility decommissioning at Sellafield. However the current best estimate, albeit based on limited decommissioning experience, is that 70% of this material may be 'out of scope'of regulatory control (i.e. not radioactive for the purposes of UK legislation).
[6] Volumes are those reported by the waste producers. They are for untreated or partly treated wastes, apart from wastes that are conditioned where the conditioned volume is reported. For HLW conditioned volume and mass are reported.

Table 1.1: Volumes and masses of all UK radioactive waste as at 1 April 2016 and estimated for future arisings [4].

exist now or that will arise in the future. It also contains radioactive materials that are not classed as waste now but may be in the future if no further use can be found for them. According to the figures published by the NDA, the totals by volume of UK radioactive waste as of 1 April 2016 and estimated future arisings from all sources was 4,490,000m^3. Of this waste, 93.5% by volume is VLLW/LLW, 6.4% is ILW (286,000m^3) and less than 0.1% is HLW (1,080m^3) and about 74% of all waste is generated at Sellafield [4]. The masses for each volume and an illustration of the radioactive waste producers in the UK are given in Table 1.1 [5].

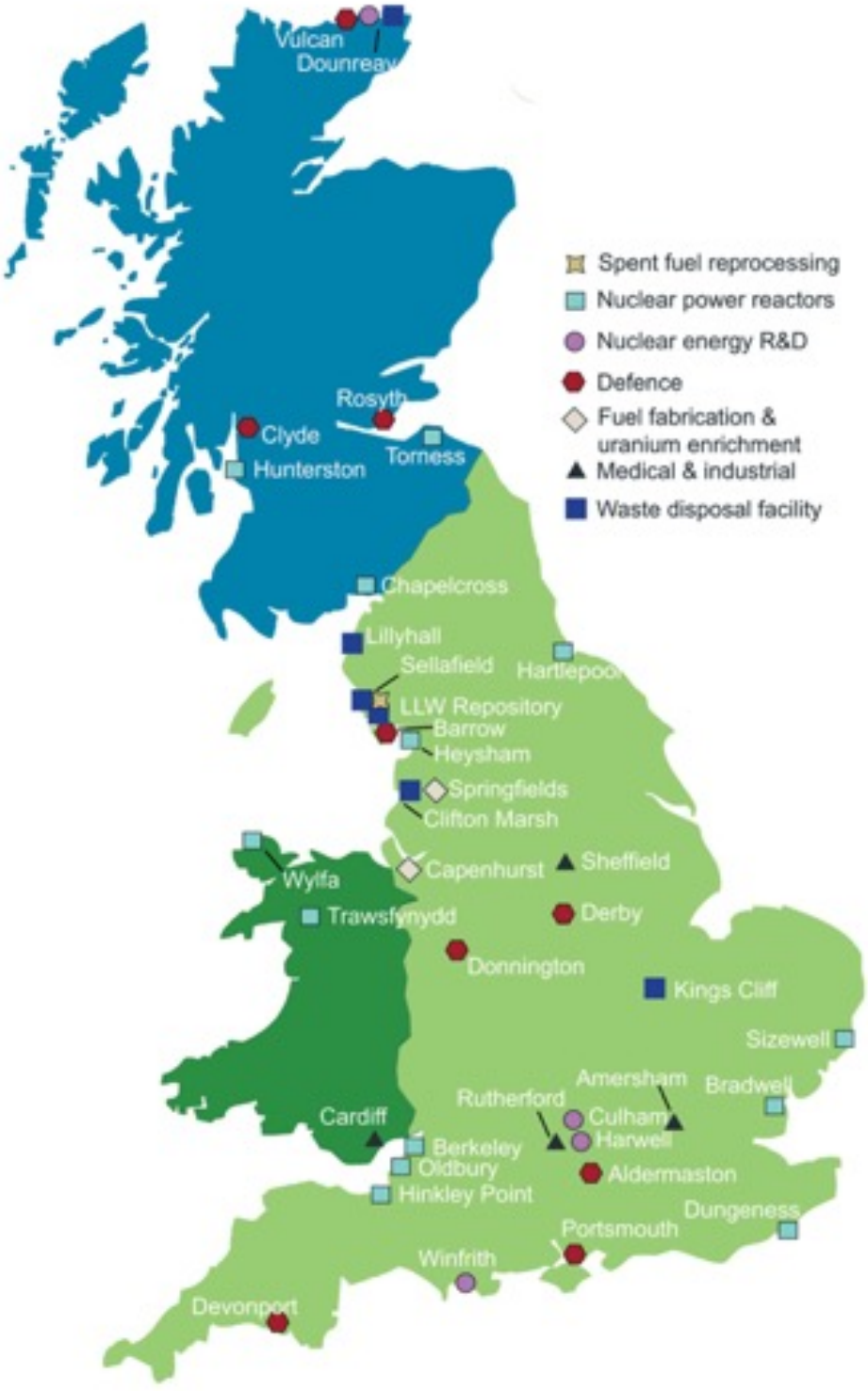

Figure 1.2: Map of the locations currently used for the storage and producers of radioactive waste in the UK. A graphical representation of the type of waste at each location is shown [5].

Waste producers are responsible for characterising their own waste by using the following methods [1, 2, 6]:

- Using records to collect information about how, when and where the waste was produced.
- Using non-destructive assay (nda) to ascertain the types of radiation emitted from the waste.
- Taking samples of the waste for analysis in laboratories.
- Interpreting data about the radiological, chemical and physical properties of the waste.

There are regulatory implications for waste producers if waste is incorrectly characterised into a category lower than appropriate but also it is a waste of (tax payers) money to store waste in a higher classification than necessary. Regulations [2] allow for the imposition of sanctions, including financial penalties such as fines and/or the loss of licence, against users who underestimate the activity present in waste. This has resulted in waste producers being cautious in their characterisation techniques, particularly for waste that is close to the boundary between LLW and VLLW [7]. A pie chart of the various types of LLW that are in the UK inventory together with the relative percentages for each type is shown in Figure 1.3[4].

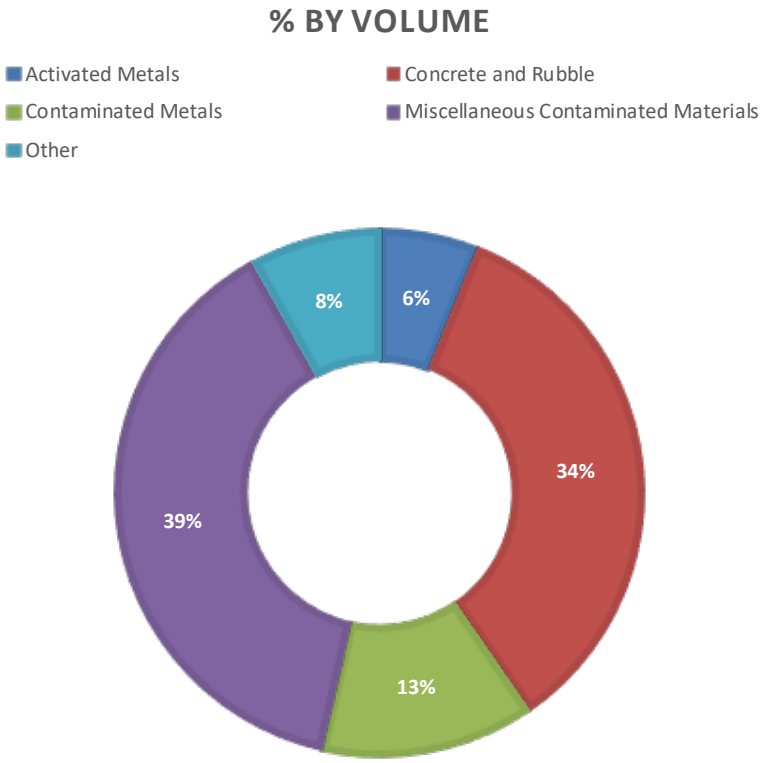

Figure 1.3: Pie chart of the different forms of LLW in the UK showing the relative percentages for each type by volume (adapted from [4]).

Solid LLW is transported by rail in ISO freight containers and ultimately stored at the Low-Level Waste Repository (LLWR) in Cumbria. An aerial photograph of the repository is shown in Figure 1.4. The current storage area is shown in the foreground and illustrates that there is a finite storage capacity. It has been determined by Government that there is a need for a reduction in the overall volume of LLW sent for storage by adopting sustainable LLW management practices [8]. Methods used for the characterisation of LLW at the repository will be outlined inSection 2.1 but include assay using gamma ray detectors. As a consequence, the NDA and LLWR have initiated a number of research projects which aim to reduce the overall volume of waste that is unnecessarily sent to the repository by waste producers. One such project is to make improvements in the radiation detection methods used in the characterisation of LLW and this is encompassed in this thesis.

Figure 1.4: Aerial photograph of the Low Level Waste Repository in Cumbria, with Sellafield in the distance. The current storage vault is in the foreground. [9].

Regulations require that periodic checks are made on waste that is sent to the LLWR. These checks may be carried out at LLWR or, in the case of an increasing number of sites (currently 7 at customer sites and 7 at service provider sites [6]), on site monitoring is performed. An incentive to encourage LLWR users to characterise their waste correctly is the cost of disposal, which, for 2018/2019 is £3292 m^{-3} for LLW [6]. A variety of techniques are used to monitor the waste which arrives at the repository, one such method is gamma ray spectroscopy. High Purity Germanium (HPGe) detectors would typically be used for these measurements due to their excellent energy resolution, which facilitates isotope identification. However, to improve the accuracy of the measurements further without increasing counting time, it is necessary to suppress background counts.

1.3 Thesis Outline

The work presented in this thesis is the development, validation and optimisation of a Digital Compton Suppression Algorithm (DCSA). The algorithm will be used to suppress

gamma ray interactions occurring in regions of a Broad Energy Germanium (BEGe) detector by exploiting the position dependent charge collection response of the detector. This will be based on the knowledge that low energy gamma rays, such as those from ^{241}Am, will only interact in the surface of the detector, whilst higher energy gamma rays from the background and sources in the waste stream (i.e. ^{60}Co and ^{137}Cs) will interact throughout the volume of the detector and as such, position dependent charge collection is suitable for use in the non destructive assay of LLW. Chapter 2 discusses methods used for the non destructive assay of radioactive waste in the United Kingdom. Chapter 3 outlines the fundamentals of gamma ray spectroscopy and in particular, the interactions with matter applicable for the scope of this thesis and the charge collection processes that give rise to the position dependent output. Chapter 4 describes the generation and validation of a theoretical signals database for a Broad Energy Germanium detector (BEGe) using the Agata Detector Library software [10]. Chapter 5 presents the development of the DCSA and demonstrates improvements in the Minimum Detectable Activity (MDA) of a BEGe detector. Chapter 6 discusses the analysis of experimental test data acquired using the BEGe detector with ^{241}Am and ^{137}Cs at the University of Liverpool and using more complex waste matrices at the National Nuclear Laboratory Central Laboratory. The optimisation of the DCSA is also discussed in this chapter. Chapter 7 presents the conclusions and recommendations that arise from this thesis.

Chapter 2

Non-Destructive Assay of Radioactive Waste

Although the processing methods used for radioactive waste differs according to the category of the waste, the requirement that is common to all waste types is the need for its characterisation. There are numerous methods for this characterisation including alpha/beta -particle and gamma ray spectroscopy. In the UK, the categories of radioactive waste are predominantly classified according to the activity of the waste in question (Chapter 1) with the following descriptive additions [1, 2]:

- **VLLW** can be safely disposed of by incineration or included with municipal, commercial or industrial waste but only at specified landfill sites in line with regulations. Incineration effectively dilutes the activity leaving waste that is out of the scope of the regulations.
- **LLW** can be any material that has been activated or contaminated by radioactivity. After characterisation at the user's site, LLW is ultimately stored at the LLWR.
- **ILW** is any material that has been activated or contaminated by radioactivity. ILW may be in the form of a solid, sludge or effluent and does not generate heat.

ILW arises mainly from the reprocessing of spent fuel, from general operations, maintenance and decommissioning of a radioactive plant. Currently ∼70% of the UK's ILW is stored within purpose made facilities at the Sellafield plant, Cumbria, the remainder is stored at power plants, research facilities and defence establishments.

- **HLW** is generated as a by-product during the reprocessing of spent fuel from nuclear reactors and also from the spent fuel itself. It has a high temperature due to its high levels of radioactivity. HLW is stored in purpose made facilities at Sellafield.

In line with other industries and domestic households, the NDA has implemented a waste hierarchy system. The purpose of the hierarchy is to minimise the amount of waste that is disposed of from all waste streams by encouraging the waste producers to investigate new approaches to waste management (Figure 2.1) [4]. As the figure suggests, in the first instance the preferred option is the prevention of waste, thereafter, in decreasing desirability, reduction in waste production, re-use, recycling, with the final recourse being that of disposal. This thesis will concentrate on gamma ray spectroscopy and its use in the characterisation of LLW as part of the NDA mission to reduce the overall volume sent for disposal and this falls within the waste minimisation tier of the hierarchy.

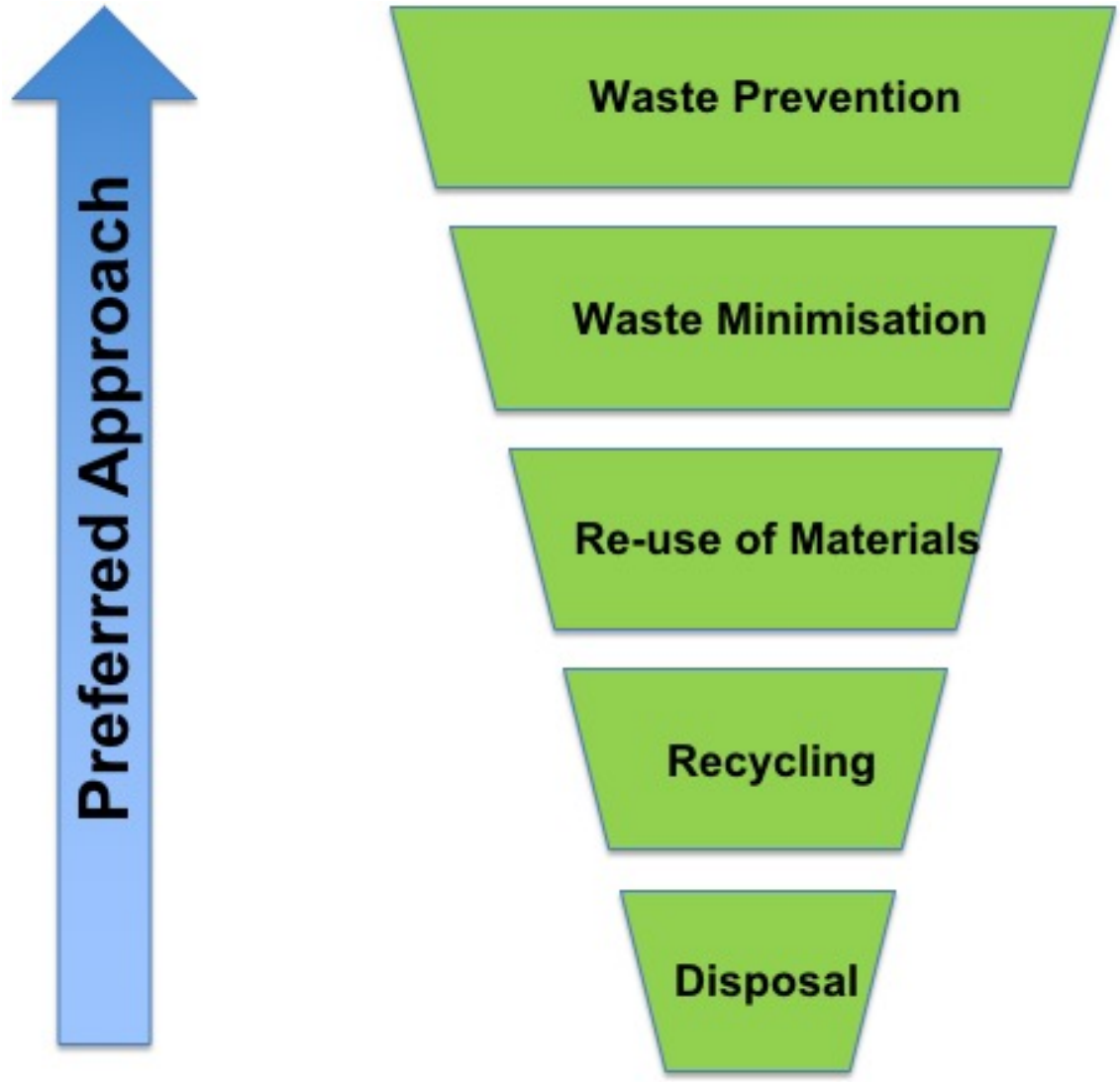

Figure 2.1: The waste hierarchy used by the UK nuclear industry, adapted from [4]

2.1 Methods used for Non-Destructive Assay

Upon reception at the LLWR, ISO freight containers are characterised using a High-Resolution Gamma Scan (HRGS) (Figure 2.2). The HRGS is conducted using HPGe in-situ portable gamma ray detectors such as the Ortec Transpec [7]. To accomplish the HRGS, the detector is positioned at 8 locations, 3 along each long vertical side and 1 at each end of the shipping container and a scan taken at each of these location. By combining the data from these 8 scans, a 3D map of the activity within the container is constructed. This map is used to assess the overall activity/kg of the container and, where possible, the identification of the nuclides present. However, this type of scan does have

some inherent problems:

- Attenuation due to the composition of the waste constituents is not accounted for.
- Radionuclides of interest may be masked by Compton scattering events from other radionuclides, particularly in the case of low energy gamma emitters such as ^{241}Am (60 keV) in the presence of high energy gamma emitters such as ^{137}Cs (662 keV), this will be discussed in Section 3.1.6.
- Long measurement times are required to enable quantification of relative activities.

Although not usually the case, in an effort to overcome some of these challenges, further scans may be carried out with longer counting times which provide higher statistics to then enable the identification of radionuclides with lower activities that may be present [6]. After characterisation, to reduce the stored volume, waste from several of the containers can be combined by compacting into drums at the LLWR on-site compaction plant. The drums are encapsulated in cement and returned to an ISO freight container before the whole container is finally capped with another layer of cement. The cap acts as both shielding and as a stabilisation medium.

Figure 2.2: Image of an Ortec Transpec detector being employed to monitor an LLW ISO freight container received at LLWR [7].

It should be noted that non-destructive assay (nda) techniques are not exclusively the realm of gamma ray spectroscopy, indeed there are other methods that may be more appropriate depending on:

- radiation type
- activity
- energy of emission
- the medium that the waste is encased within

For example, in situations that involve radioisotopes emitting gamma rays at low energies, the use of X-ray synchrotron radiation techniques [11] are more practical. Another example is in the assay of 210 L waste drums containing α emitting isotopes, such as ^{239}Pu, encapsulated in a concrete matrix. A more appropriate method in this scenario would be the use of active and passive neutron assay techniques[12]. However,

these scenarios are outside the remit of this thesis.

To overcome some of the challenges in characterising radioactive waste using an HRGS, an alternative method used at some facilities is the use of Tomographic gamma ray Scanning (TGS) technology, such as that illustrated in Figure 2.3a. TGS theory was introduced in the early 1990's as a follow on from Computerised Axial Scans from the 1970's [13]. TGS apparatus has since been developed to reduce the uncertainties due to gamma ray attenuation in materials located in the intervening spaces between active radionuclides. For example, in waste matrices that are held in standard 210 L drums, which may contain a mix of active and non-active waste. TGS can be carried out using HPGe detectors in conjunction with an attenuation-correction source, such as ^{75}Se (Figure 2.3b). This is used to infer the attenuation of the intervening material in the drum. To generate a 3D map, multiple scans are made with the detector at different heights and the drum rotating on a turntable. Corrections for attenuation are made in the scan control software. The corrected map gives information as to the radionuclides present in the drum together with their activities [13–16].

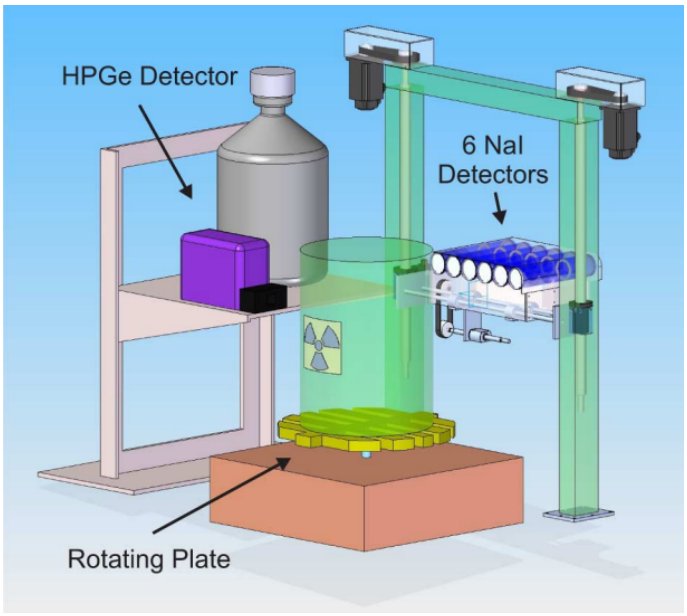

(a)

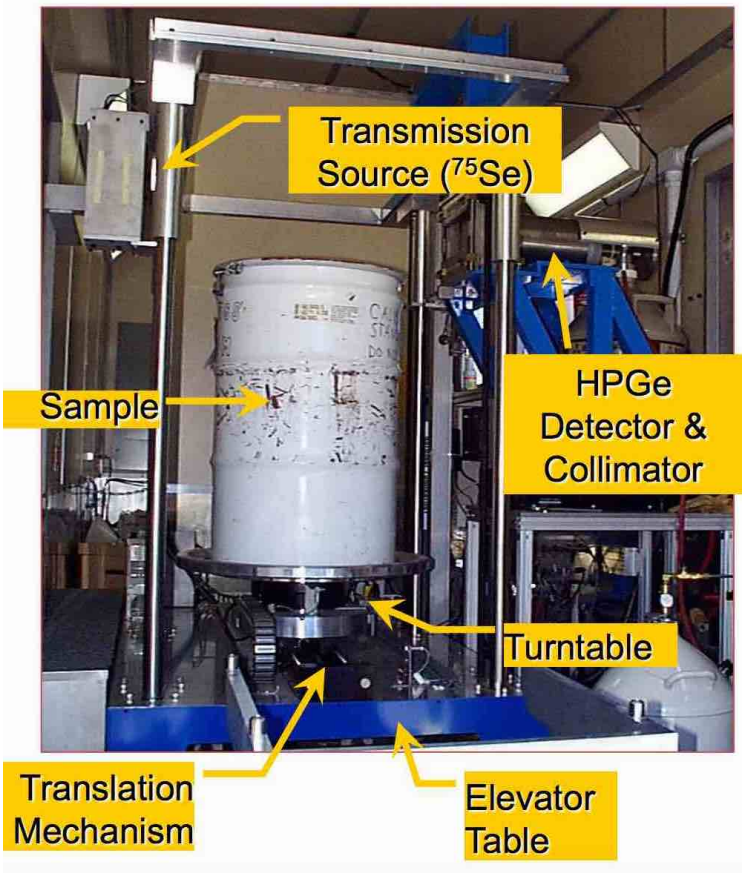

(b)

Figure 2.3: (a) Diagram of the concept of a TGS configuration and (b) TGS system showing the HPGe on the right with the ^{75}Se attenuation - correction source on the left of the drum developed at Los Alamos National Laboratory, USA and licensed to Antech [13]

A complimentary approach to TGS detectors is the use of Compton suppression

systems for spectroscopy. These typically use a BEGe primary detector together with a ring of auxiliary Bismuth Germanium Oxide (BGO) scintillation detectors. Compton suppression systems are used to reduce the background due to Compton scattering events and will be discussed together with Compton suppression itself in more detail in Section 3.1.6. An example Compton suppression system is in use at the Adriana Waste Assay Laboratory, Culham Centre for Fusion Energy, Oxfordshire (CCFE) (Figure 2.4), which is used for nda measurements of LLW arising from the activities of CCFE. The use of Compton suppression systems provides waste producers with technology that can accurately characterise LLW close to the boundary with VVLW by correctly identifying which radionuclides are present in a waste stream and quantifying the overall activity. The goal of this project is to develop an algorithm that will enable waste producers to use a single BEGe detector system to efficiently characterise waste with the same performance, negating the use of auxiliary detectors. As a consequence, the complexity and cost of the system will be significantly reduced and the systems will be more portable.

(a)

(b)

Figure 2.4: Photograph of a Compton suppression system used at the Adriana waste assay laboratory, Culham Centre for Fusion Energy. (a) Exterior view of Compton suppression system which is housed within a castellan of lead and copper shielding. A liquid nitrogen recycling/cooling system is evident to the right. (b) Internal view of a Compton suppression ring comprising of 7 BGO scintillation detectors. The central BEGe detector is not visible but located beneath the BGO's.

Chapter 3

Principles of Gamma-Ray Spectroscopy

3.1 Gamma-ray Interactions in Matter

Gamma rays interact with matter through the transfer of all or some of the their energy to electrons within atoms. As a result of these interactions, gamma rays can be observed in radiation detectors. The output signal from the detector is proportional to the energy transferred to the electrons in these interactions. This thesis will concentrate on germanium detectors which provide a spectroscopic response by the transfer of energy from gamma rays to electrons in the detector material via three methods of interaction: photoelectric absorption, Compton scattering and pair production.

The cross section is proportional to the atomic number, Z, of the detector material for each of these processes but to varying powers and has an effect on which of the three interaction processes are more probable to occur. The cross-section for photoelectric absorption σ_p, is proportional to Z^m, where m is in the range 4 - 5. For Compton scattering, the cross-section σ_C is proportional to Z and for pair production, the

cross-section σ_{pp} is proportional to Z^2 [17, 18].

For germanium, the photoelectric effect is the dominant interaction for gamma rays with energies less than 150 keV whilst for energies between $\sim$ 150 keV to $\sim$ 4.5 MeV, Compton scattering is the dominant interaction. The gamma ray energy regime of this thesis is less than 2 MeV, where Photoelectric absorption and Compton scattering processes dominate. The most probable processes for two of the radioisotopes used in this thesis are the photoelectric effect that dominates for the 59.6 keV gamma ray from ^{241}Am, and for ^{137}Cs Compton scattering dominates for the 662 keV gamma ray. Summaries of each of these and, for completeness, a summary of pair production are presented below.

3.1.1 Attenuation

The energy of the gamma ray has a bearing on which process will dominate and is illustrated in Figure 3.1 (adapted from [19]). This shows how the mass attenuation coefficient for the three interaction processes vary as a function of gamma ray energy (adapted using data from [19]). The mass attenuation coefficient, μ, is defined as being the linear attenuation coefficient, μ_l (see equation 3.2) divided by density, ρ:

$$\mu = \frac{\mu_l}{\rho} \tag{3.1}$$

For a beam of monoenergetic gamma rays striking a detector crystal (illustrated in Figure 3.2), the gamma rays will either (a) pass through the crystal without any interactions taking place, (b) be absorbed by photoelectric absorption, (c) undergo a Compton scattering event and be scattered away from the beam direction, or (d) undergo pair production. The number of gamma rays that interact with the detector crystal depends on the probability of occurrence per unit length in the crystal of each of

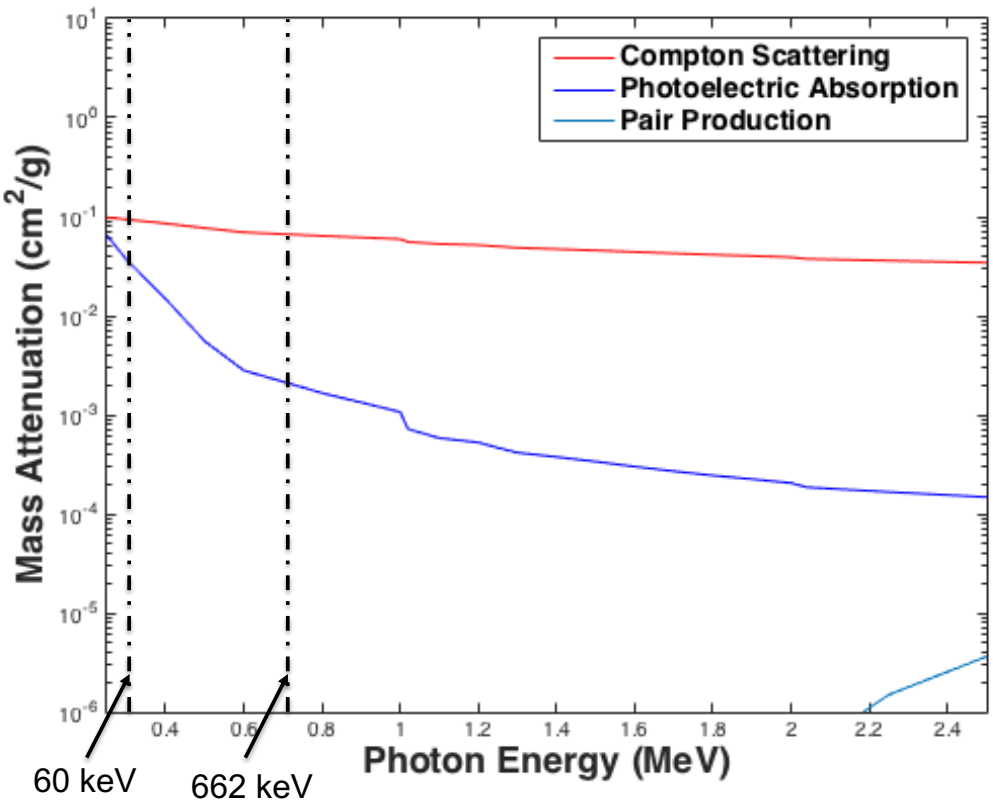

Figure 3.1: Mass attenuation of gamma rays interacting with germanium as a function of the gamma ray energy. In the energy range of this thesis between 150 keV and 2 MeV, the probability of interactions via Compton scattering dominates (Adapted using data from [19]). The two vertical lines indicate the energies of 60 keV for ^{241}Am and 662 keV for ^{137}Cs.

these interactions.

The linear attenuation coefficient, μ_l, is the sum of these probabilities and gives the probability per unit length that the gamma ray may be removed from the beam given by:

$$\mu = \tau + \sigma + \kappa, \tag{3.2}$$

where τ, σ and κ are the probabilities per unit length that the gamma ray is removed from the beam by photoelectric absorption, Compton scattering and pair production, respectively. The intensity of the transmitted beam I_x, after travelling through a material of thickness x, can be stated as [20]:

$$I_x = I_0 e^{-\mu x}. \tag{3.3}$$

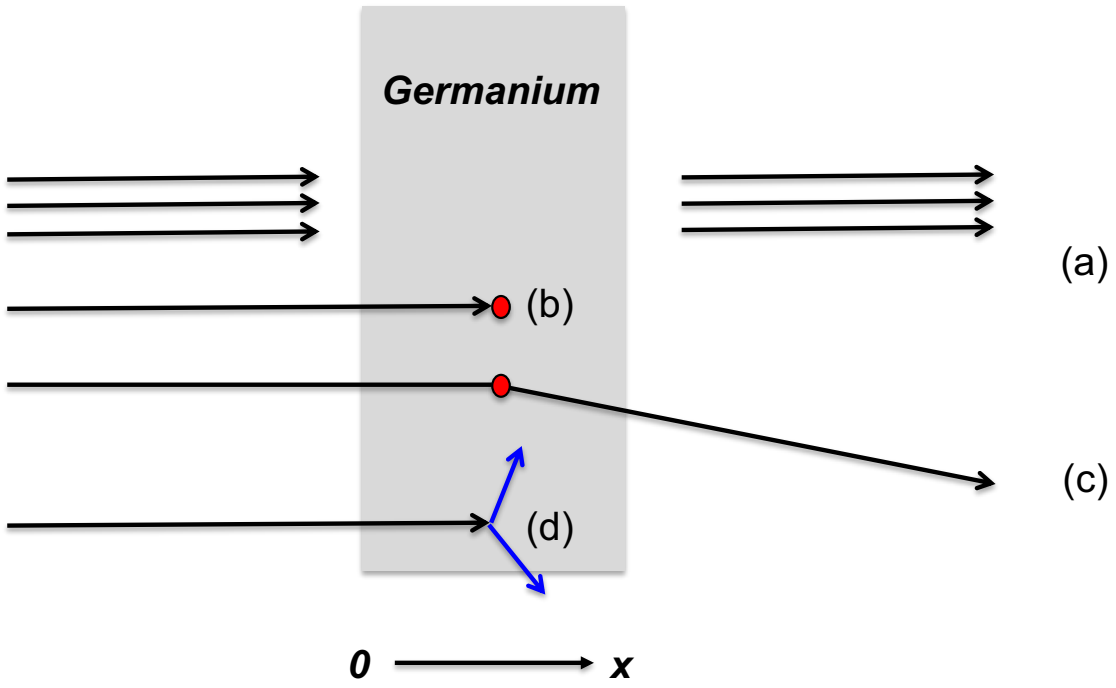

Figure 3.2: A beam of gamma rays with initial intensity I_0 enters an absorbing material with atomic number Z. The gamma rays may either (a) pass unimpeded through the detector, (b) deposit their full energy via photoelectric absorption, (c) undergo Compton scattering or (d) pair production (subsequent interactions of the pair are not shown).

where I_0 is the intensity of the original beam. Using a value of $\mu = 10.769$ cm^{-1} for ^{241}Am [21] in germanium, the distance at which 90% of the 60 keV gamma rays are removed from the beam (i.e. 10% of the beam is transmitted) is calculated as $x = 0.21$ cm using:

$$x = \frac{ln(10)}{\mu}. \tag{3.4}$$

In comparison, for 662 keV gamma rays emitted from ^{137}Cs and using $\mu = 0.396$ cm^{-1} [21], the calculated value of x is 5.80 cm in germanium. Figure 3.3 shows the attenuation plots for gamma ray beams with energies of 60 keV (^{241}Am) and 662 keV (^{137}Cs) with the positions of the face (top) and base (bottom) of the detector indicated, together with the distance at which 90% of the photons have been removed from the beam.

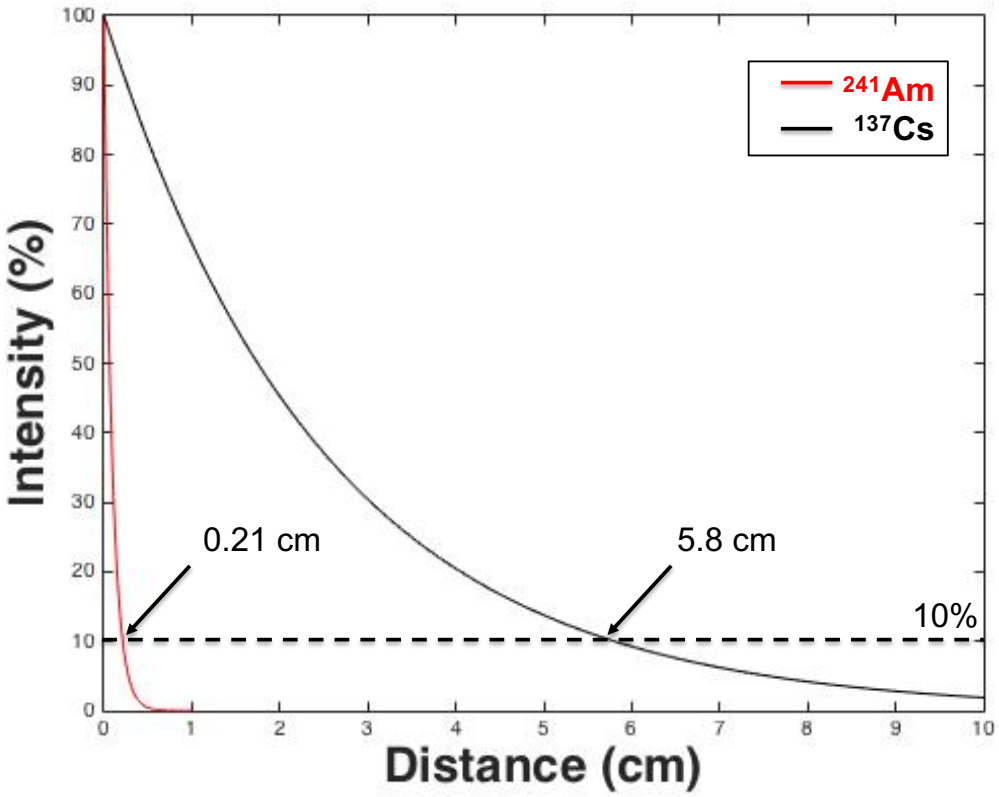

Figure 3.3: Intensity of a gamma ray beam as a function of distance travelled in germanium for (a) 60 keV gamma rays emitted by ^{241}Am and (b) 662 keV gamma rays emitted by ^{137}Cs. The distance at which the loss of 90% of the original intensity (0.214 cm for ^{241}Am and 5.804 cm for ^{137}Cs) has taken place is indicated.

3.1.2 Photoelectric Absorption

A gamma ray may be absorbed by a bound electron in an atom via the photoelectric effect [22] (Figure 3.4). The shell within which this takes place is determined by the energy of the gamma ray but, because the cross section is much larger for tightly bound electrons rather than weakly bound electrons, this typically takes place in the K shell. The binding energy of a K-shell electron is 11.1 keV, at gamma ray energies below this, the process may involve an L or M shell electron of the electron cloud [23]. The corresponding binding energies for the L and M binding energies in germanium are 1.41 and 0.180 keV respectively [24]. The result is that an electron is ejected from the orbital shell [25] with an energy given by equation 3.5.

$$E_{e^-} = E_\gamma - E_b, \tag{3.5}$$

where E_{e^-} is the kinetic energy of the ejected electron, E_γ is the energy of the incident γ-ray and E_b is the binding energy for the K-shell electron. After the interaction, the atom is left in an excited state and may return to equilibrium by re-distributing the excess energy to other electrons in the electron cloud of the atom, which can lead to Auger electrons being released. Alternatively, the excited atom may return to equilibrium by an electron with higher energy filling the hole left by the ejected electron. This results in the ejection of a fluorescence X-ray which may then also undergo absorption.

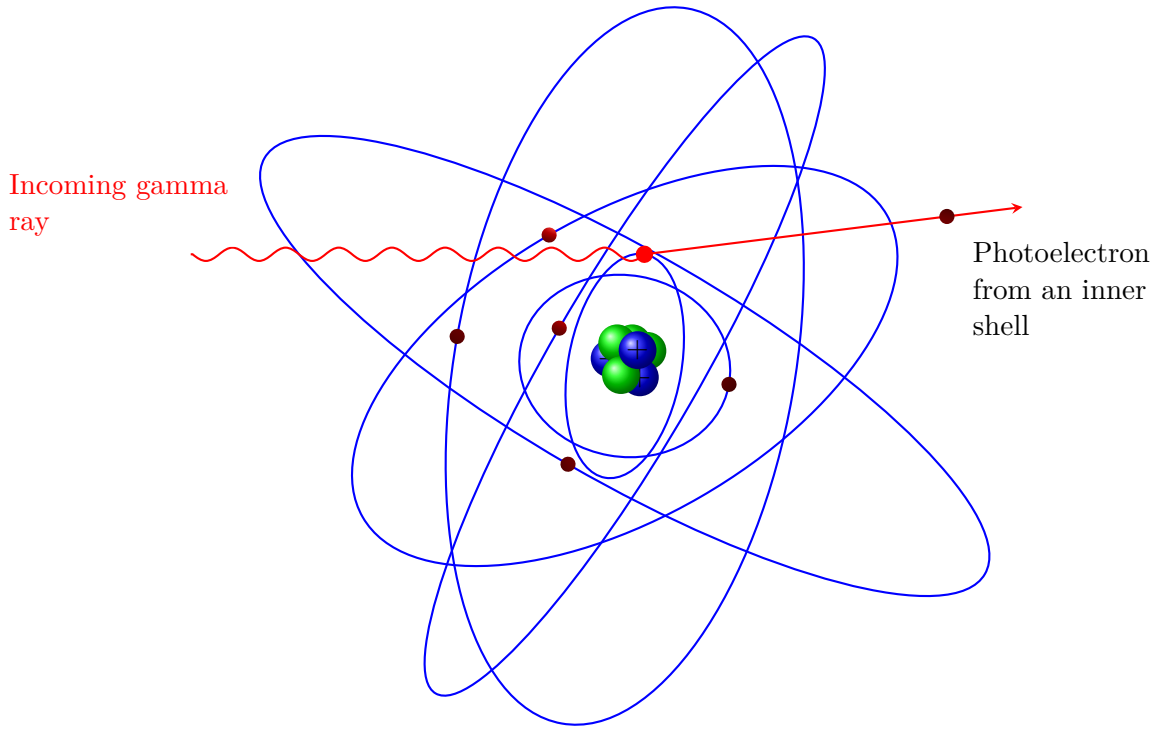

Figure 3.4: Schematic illustration of the photoelectric effect showing a gamma ray that is absorbed by the atom resulting in an orbiting electron being ejected from the electron cloud.

3.1.3 Compton Scattering

Compton scattering is the interaction of a gamma ray, with energy E_γ, and an electron in an atom of the material [26]. However, in contrast to photoelectric absorption, the gamma ray will scatter at an angle θ and the loosely bound electron will recoil from the atom as

depicted in Figure 3.5.

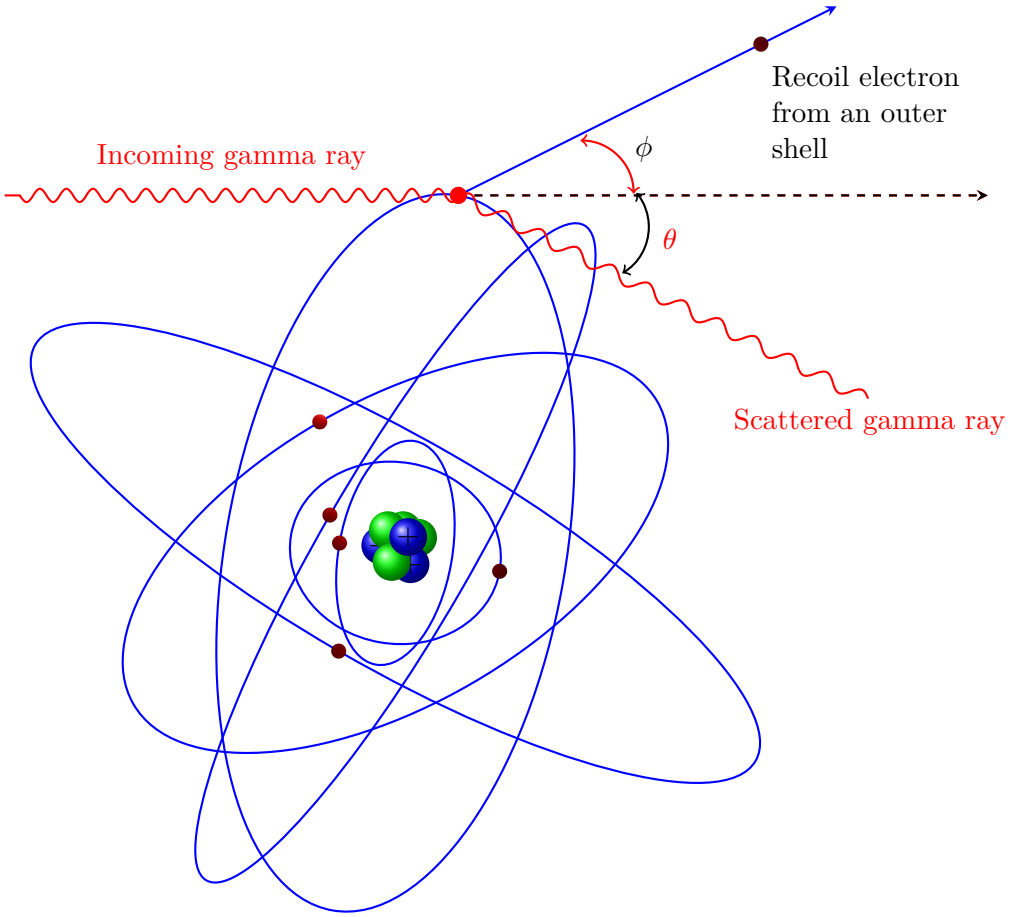

Figure 3.5: Schematic illustration of the Compton Scattering process showing a gamma ray interacting with an orbiting electron, the electron is ejected at at angle (ϕ). The gamma ray is scattered through an angle (θ)

.

E_γ is distributed between the recoil electron and the scattered gamma ray with energy $E_{\gamma'}$. The scattered gamma ray may either exit the detector or undergo further scattering events until its energy is lost through photoelectric absorption.

Compton scattering leads to a continuum of energies being transferable to the electron, the energy of the recoil electron (E_{e^-}) is given by [23]:

$$E_{e^-} = E_\gamma \left(1 - \frac{1}{(1 + E_\gamma[1 - cos(\theta)]/m_0c^2)}\right), \tag{3.6}$$

and m_0c^2 is the rest mass energy of the electron. This gives rise to a maximum energy transfer when $\theta = \pi$ and results in the Compton edge in a gamma ray spectrum. The gap

between the full energy peak and the Compton edge is given by E_C in:

$$E_C = \left[\frac{E_\gamma}{1 + (2E_\gamma / m_0 c^2)} \right]. \tag{3.7}$$

A γ-ray spectrum will show the full energy peak(s) together with the Compton edge(s) and Compton continuum. A schematic of the relationship between these features and the full energy peak for a single energy is shown in Figure 3.6, this is for an ideal scenario where the effects of the detector are negated and it is assumed that there are no multiple scattering events.

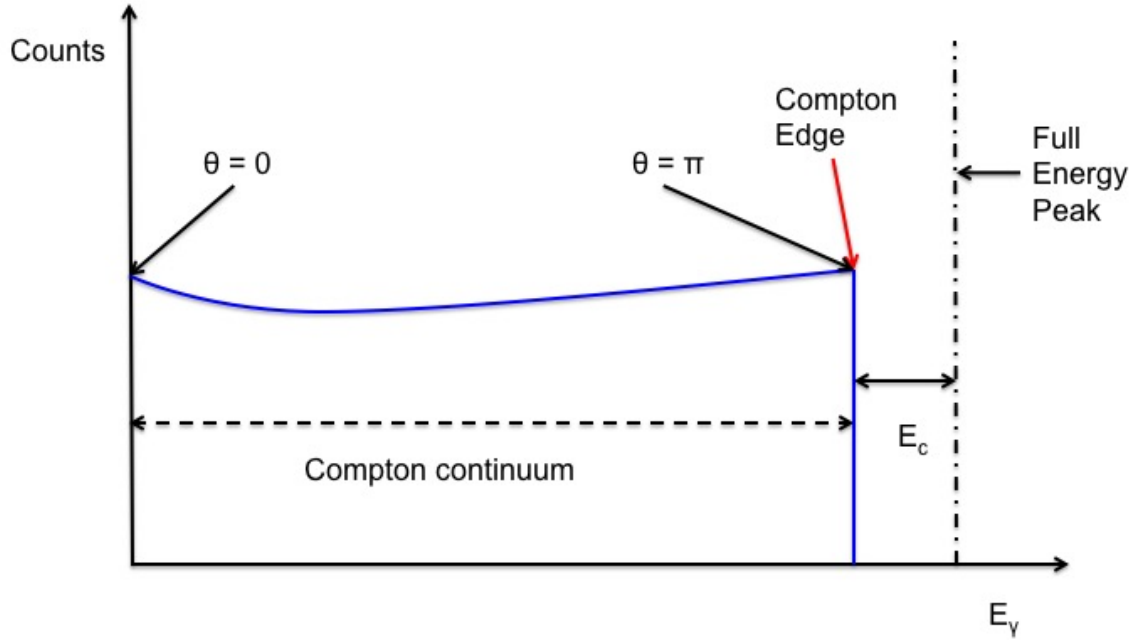

Figure 3.6: Diagram showing the relationship between the full energy peak, the Compton edge and the Compton continuum in a gamma ray spectrum. The diagram is for an ideal scenario and negates detector effects and also assumes that there are no multiple scattering events (adapted from [27]).

The Compton continuum can be mitigated by using an active veto shield, which was introduced in Section 2.1 and will be discussed further in Section 3.1.6. When using gamma ray spectroscopy for the assay of LLW, it is particularly challenging to detect isotopes that emit low energy gamma rays (i.e. ^{241}Am) if the LLW contains radionuclides that emit gamma rays at higher energies, (i.e. ^{137}Cs). The Compton continuum from ^{137}Cs will reduce the signal to noise ratio of a ^{241}Am 60 keV peak. This requires longer

counting times to detect the ^{241}Am with a particular confidence level, increasing the cost of waste assay using gamma ray spectroscopy.

3.1.4 Pair Production

In cases where the gamma ray energy exceeds twice the rest-mass energy of an electron (1.02 MeV), the process of an electron-positron pair production is possible and given by [25]:

$$\gamma + (nucleus) \rightarrow e^{+} + e^{-} + (nucleus). \tag{3.8}$$

The process takes place in the Coulomb field of the nucleus and the gamma ray is replaced by an electron-positron pair. The produced pair share the energy of the incident gamma ray in excess of 1.02 MeV as kinetic energy given in:

$$E_{\gamma} = (T_{-} + m_0c^2) + (T_{+} + m_ec^2), \tag{3.9}$$

where T_{-} and T_{+} are the kinetic energies of the electron and positron respectively [28]. After production, the distance that the positron travels is dependent on the Z value of the material. The positron will usually only travel a few mm within the germanium detector before thermalising and annihilating with another electron. Following annihilation, two 511 keV photons are produced, these travel along paths that are at 180° to each other (Figure 3.7).

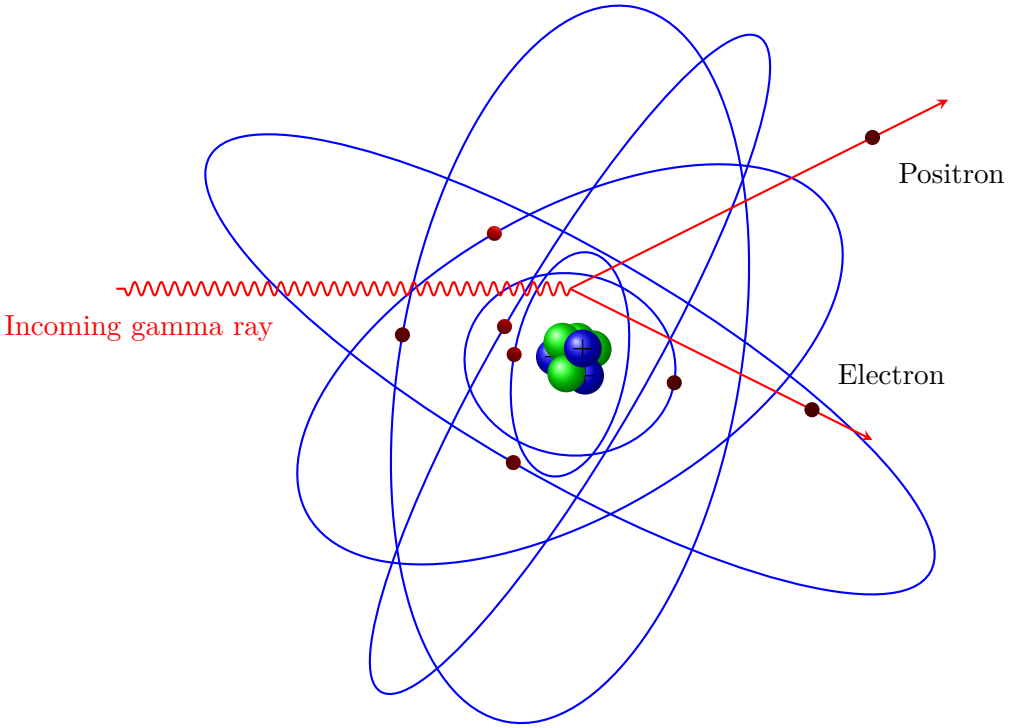

Figure 3.7: Diagram showing a gamma ray interacting with the Coulomb field of the nucleus, an electron/positron pair are produced.

3.1.5 BE6530 Geometry

The BEGe used for this work is a Mirion Technologies Inc. (formerly Canberra) BE6530 p-type shown in Figure 3.8. The contact on the outer face of the BE6530 crystal is of n-type material formed by direct ion implantation, the small p-type contact is produced by boron implantation; n- and p-type materials are discussed in Section 3.2.2. The BE6530 is a HPGe detector, with a crystal that measures 91 mm in diameter and 31 mm in depth, designed specifically to have excellent energy resolution across a broad energy range (3 keV $\longrightarrow$ 3 MeV), as applicable to LLW assay. As an example, the energy resolution at energies of 122 keV is quoted by Mirion as being 0.75 keV and 2 keV at energies of 1332 keV [29]. The crystal is mounted in a vacuum within an aluminium end cap with a carbon epoxy entrance window. The end cap also encapsulates the preamplifier and is directly mounted onto an electronic Cryopulse+ cooler which is controlled by an integrated controller/power supply [29].

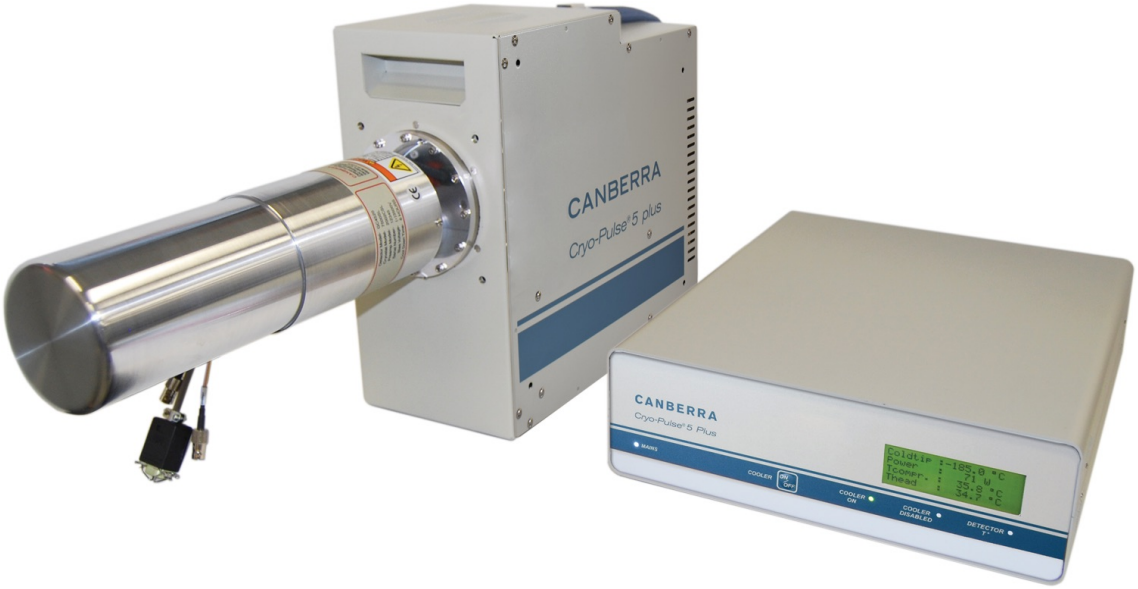

Figure 3.8: Photograph of Mirion (Canberra) HPGe detector cryostat with CP-5+ cryo-cooler and integrated controller/power supply[29].

The design of the BE6530 detector gives low capacitance which is inversely proportional to the depletion layer of the detector and proportional to the noise at the preamplifier [30]. The combination of low capacitance and the small anode technology used for this detector type results in a detector with good signal to noise ratio [30] giving good resolution in the spectrum at low and medium energies. It has been noted that due to attenuation, the distance from the edge of the detector crystal at which 90% of an incident beam of gamma rays from ^{241}Am are absorbed is 2 mm in germanium, this can be defined as the surface region. The remainder of the crystal can be defined as the bulk and gamma rays from higher energy sources such as ^{137}Cs may penetrate throughout the crystal volume. It is hypothesised that it will be possible to differentiate between pulse shapes that arise from interactions that take place within the surface region from those which are a result of interactions within the bulk region of the detector crystal, these regions are shown in Figure 3.9.

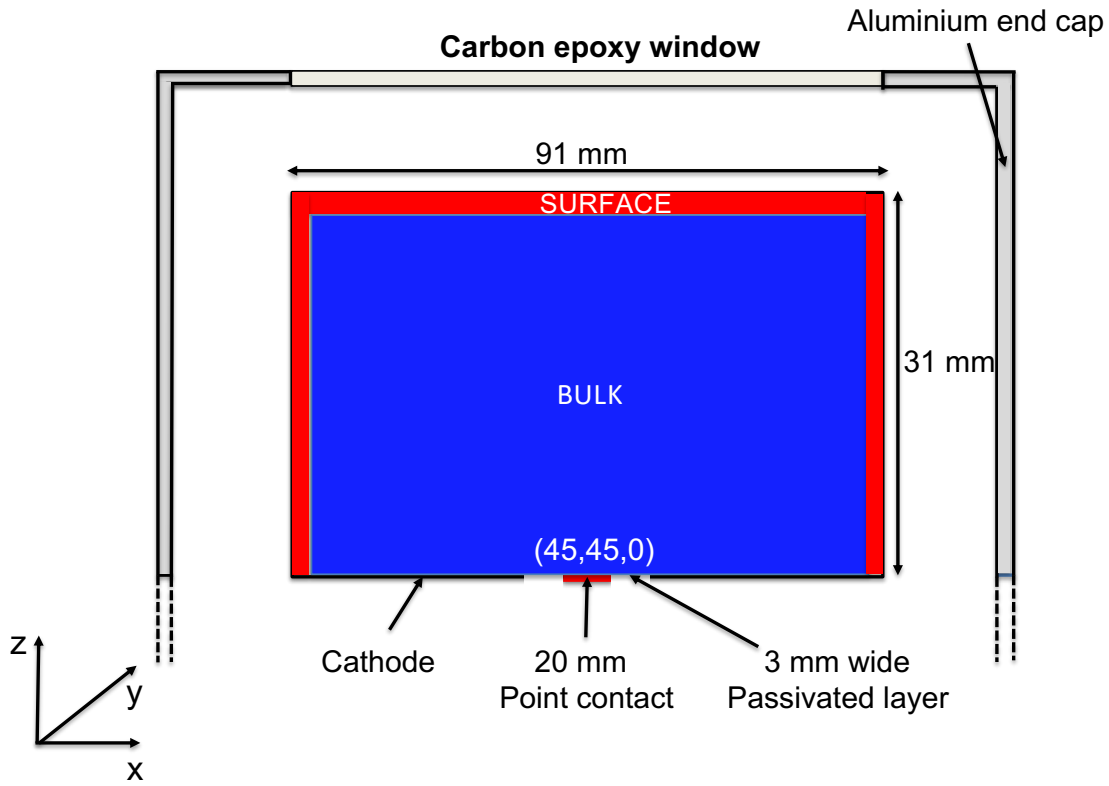

Figure 3.9: Schematic of surface and bulk regions within a BEGe detector, the (45,45,0) coordinate and coordinate system are shown.

3.1.6 Compton Suppression

As discussed in Section 2.1, Compton suppression is used in waste assay. This relies on coincident detection veto techniques with multiple detector. A timing gate is used to identify signals that are generated from the BEGe detector, and in an array of surrounding detectors. These events will be rejected from the germanium detector spectrum since they are as a result of the gamma ray depositing its energy across multiple detectors. For low singles rates, it is more probable that events that trigger both detector types are as a result of a scattering event from the primary detector rather than two uncorrelated events. However, in the case of high singles rates, a large number of random coincidence events will also occur. To be effective, any Compton suppression system should be able to account for scattering angles in all directions by having a 4π detection geometry [31]. A schematic illustration of a suppression detector setup using a BEGe detector surrounded

by a Compton suppression system of scintillator detectors is shown in Figure 3.10. A gamma ray is shown entering the BEGe from the bottom of the image, it then Compton scatters out of the BEGe. It subsequently enters the surrounding Compton shield to be vetoed from the germanium spectrum. Such an event would otherwise contribute to the Compton continuum in the spectrum.

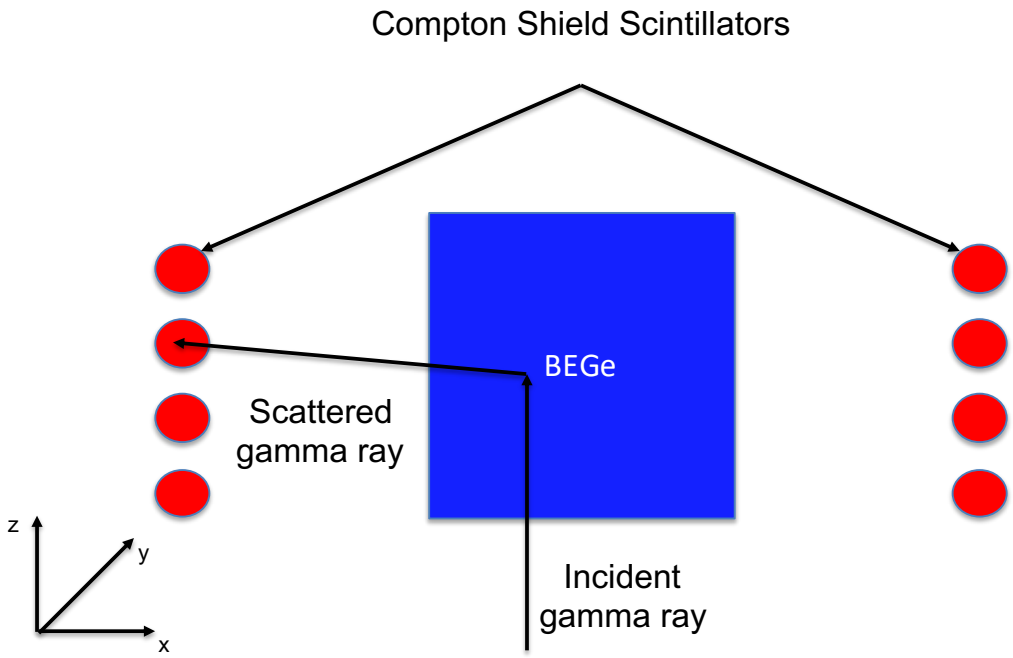

Figure 3.10: A schematic of a BEGe detector surrounded by a Compton suppression shield which comprises of scintillator detectors. A gamma ray is shown entering the BEGe from the bottom of the diagram, this then undergoes Compton scattering and exits the BEGe before entering the Compton shield.

3.2 Charge Induction Processes in Germanium Detectors

Germanium is widely used for gamma ray spectroscopy applications, Table 3.1 displays the key properties of intrinsic germanium [23].

Properties of Intrinsic Germanium

Property	Value
Atomic number (Z)	32
Density (77 K) (g/cm^{-3})	5.32
Band gap energy (77K)	0.67 eV
Dielectric constant	16.32
Ionisation energy per electron - hole pair (77 K)	2.96 eV
Electron mobility (77 K) (cm^{2}V^{-1}s^{-1})	3.6 x 10^4
Hole mobility (77 K) (cm^{2}V^{-1}s^{-1})	4.2 x 10^4

Table 3.1: The key properties of germanium [23].

A solid is made up of a crystalline structure, the atoms of which will each have one of a specific range of energy levels appropriate to the crystal. The grouping of the atoms into a crystal structure creates an energy band whose energy will be the range of the constituent atoms. These bands will be separated by a gap of energy levels which are forbidden to electrons. This band structure can be defined in terms of the upper *valence band*, the lower *conduction band* and forbidden zone or *bandgap*. Considering the model of the atom, the outer or valence electrons occupy the uppermost energy band. The crystal will be an insulator if the number of valence electrons in a cell of the crystal is an even integer. However, if the energy bands overlap then there may be two partly filled bands giving a metal. Germanium has two atoms, with four valence electrons each, whose energy bands do not overlap. Germanium is an insulator at absolute zero since the conduction band is empty. As the temperature of the crystal rises, electrons are thermally excited from the valence band to the conduction band where they are then mobile. Germanium is a semiconductor at temperatures above absolute zero. The excited electrons will leave *holes* in the valence band [32, 33]. A brief description of the different material types follows with a schematic shown in Figure 3.11.

- **Conductor** - the conduction and valence bands overlap or the conduction band is not filled. Only a small amount of kinetic energy from thermal excitation is needed for valence electrons to be promoted to the conduction band because there is no

band gap.

- **Insulator** - has a minimum band gap of greater than 5 eV. Thermal excitations are not sufficient to promote valence electrons to the conduction band.
- **Semiconductor** - has a small band gap less than 1 eV. Thermal excitations are sufficient to allow valence electrons to move to the conduction band.

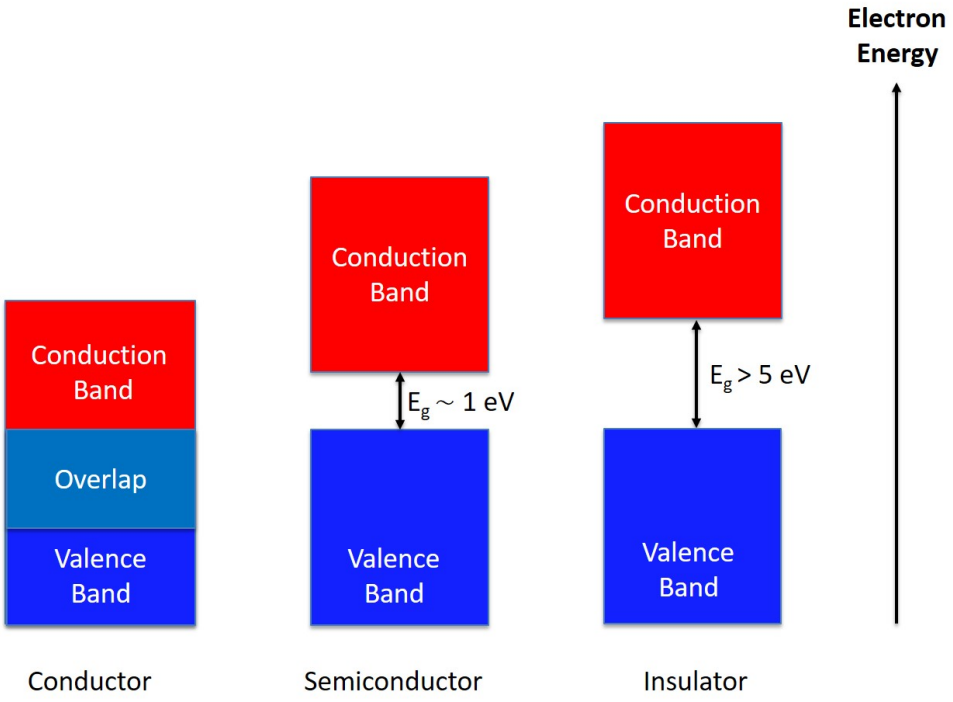

Figure 3.11: Schematic illustration showing the changes in the relative band gaps for conductors, semiconductors and insulators.

The intrinsic conductivity and carrier concentrations are largely controlled by the ratio of the energy of the band gap, E_g, to the temperature, T, $E_g/k_B T$ [32] where k_B is Boltzmann's constant. Conductivity will be low when this ratio is large because the concentration of intrinsic carriers will be low and conduction will be high when the ratio is small. The subsequent sections explain the principles in using semiconductors as radiation detectors.

3.2.1 Charge Carrier Generation

The interactions of gamma rays within the detector material may involve electrons with energies that are far greater than the excitation energies needed to promote from the valence to conduction band. These electrons may undergo a number of excitation events leading to an *electron-hole cascade*. The absorbed gamma ray energy E_{abs} is related to the number of electron-hole pairs produced, n, by equation 3.10 [23]:

$$n = \frac{E_{abs}}{\epsilon}, \tag{3.10}$$

where ϵ is the average energy required for an electron-hole pair to be produced. Eventually, the excited electrons will de-excite and return to the valence band. However, the presence of an electric field will produce a field gradient within the detector crystal. As a consequence, the excited electrons will move up the gradient whilst the holes will move down. The overall net migration of the electrons and holes is due to both the thermal motion and as a result of the drift velocity. Holes in the valence band may be filled by other electrons in the valence band which in turn leads to further holes. This process may be repeated many times giving the effect that the holes drift towards the cathode. As both electrons and holes are charged, both contribute to the overall conductivity of the material.

At low to moderate field intensities, the drift velocity (ν) of both the electrons and holes is proportional to the applied field. A mobility constant for both electrons (μ_e) and holes (μ_h) can be given by [27]:

$$\nu_e = \mu_e \overrightarrow{E}, \tag{3.11}$$

$$\nu_h = \mu_h \overrightarrow{E}, \tag{3.12}$$

where ν_e and ν_h are the drift velocities for electrons and holes respectively.

The temperature of the material will determine the number of electrons that are excited and promoted to the conduction band, with increasing temperature the mobility constants also reduce, i.e. in comparison to the values given in Table 3.1, at 300 K the constants are 3900 and 1900 cm^2/Vs for electrons and holes respectively. Drift velocity is a function of both temperature and energy [27]. However, with increasing temperature the loss in kinetic energy, due to an increase in the number of collisions between electrons and atoms, will mean that drift velocities will saturate once the electric field is greater than approximately 10^4 V/cm. At this field strength the change in mobility constant is proportional to $1/\overrightarrow{E}$ with corresponding drift velocity values of approximately 10^7 cm/s [34]. However, as we shall see in Section 3.2.4, detectors are operated at a voltage that ensures that drift velocities are saturated.

3.2.2 n and p Doping

Germanium semiconductors are classed as extrinsic semiconductors since their crystals will contain impurities to improve their conductivity, these impurities are the result of doping. The type of dopant alters the conductivity by either giving electrons (donors) to the conduction band or by creating holes (acceptors) in the valence band [33]. The *donor* impurity will determine whether the crystal is an n-type, for donors, or p-type, for acceptors. The impurities will add extra states either just above the valence band for p-type and just below the conduction band for n-type germanium as illustrated in Figure 3.12.

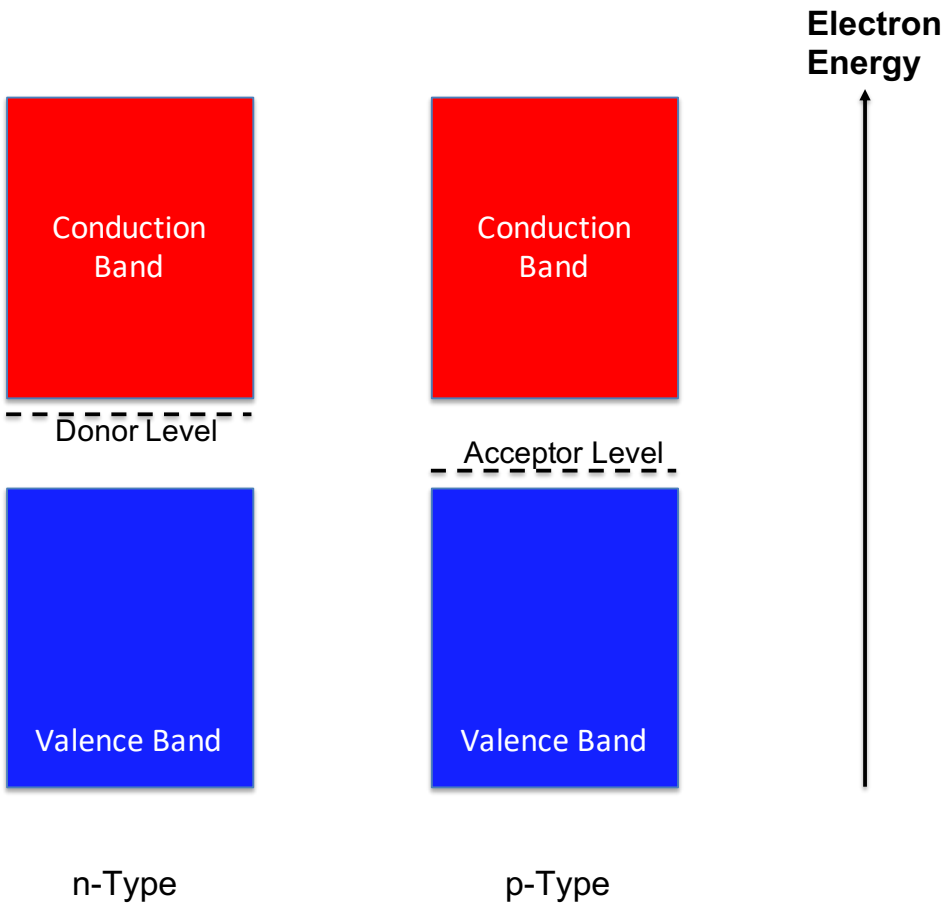

Figure 3.12: Illustration of the band structure in *n-type* and *p-type* semiconductors.

3.2.3 The p-n Junction

Since n-type materials are dominated by electrons with only a few holes and vice versa for p-type materials, a p-n junction can be created at the interface of these semiconductor materials when they are in contact and under thermal equilibrium. It is the p-n junction that enables semiconductors to be used as radiation detectors. A large carrier gradient exists at the boundary between the materials due to the composition of the n- and p-type materials. As a consequence there will be diffusion of holes from the p-side towards the n-type material with a diffusion of electrons in the opposite direction. As a result, a negative space charge will form on the p-side of the junction as negative acceptor ions ($N_A{}^-$) are left uncompensated and a positive space charge near the n-side due to the uncompensated positive donor ions ($N_D{}^+$). The region of space charge that is created at the p-n junction

is referred to as the *depletion layer*. Figure 3.13 is a schematic illustration of a p-n junction showing the relationship between the electrons, holes and depletion layer.

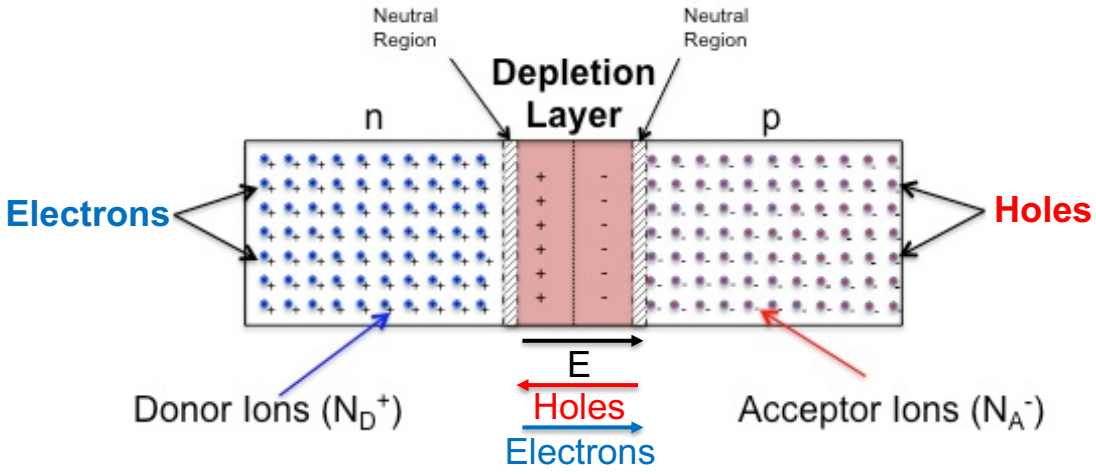

Figure 3.13: Illustration of the p-n junction showing the relationship between holes, electrons and the depletion layer, adapted from [35].

A built in potential, V_{bi}, gives rise to an electric field across the junction, which opposes the diffusion of holes and electrons. Detectors such as a BEGe use a p-n junction crystal and are operated with a reverse bias voltage.

3.2.4 Reverse Biasing of the p-n Junction

If a positive voltage V_R is applied to the n-side with respect to the p-side, the p-n junction becomes reverse-biased and the total electrostatic potential across the junction increases by V_R, that is, it is replaced by $V_{bi} + V_R$. The application of a reverse bias increases the depletion layer width. The p-junction is made negative with respect to the n-junction by applying a positive voltage to the n^+ contact.

The effect of this is to enhance the potential of the detector, the minority carriers within the material (electrons on the *n* side and holes on the *p* side) are attracted across the junction. Since the concentration of the minority carriers is small, the reverse current is low. The desired feature of this design is to allow the free flow of current in the forward

direction whilst limiting any reverse current.

If the bias voltage is high enough, a depletion region will extend across the entire detector. At this point a uniform electric field will be found with the only "dead" region being the n^+ contact itself [36]. If the voltage is sufficiently high, the electric field within the detector will be uniform and high enough to provide saturated drift velocities for the electron-hole pairs. The operating voltage of the detector is always greater than or equal to the depletion or bias voltage, usually detectors are operated at voltages much greater than the bias voltage. At the point where saturated drift velocities are achieved, small changes to the bias voltage will have little or no effect on the collection time of the charge carriers at the anode. Saturation velocities ensure minimum collection times and also minimise the adverse effects of carrier recombination and trapping (carriers that are trapped at or close to the surface of the junction). The depletion layer that originates from the p-n junction interface extends into the bulk of the detector as the voltage is increased, until, at the operating voltage, the full bulk of the crystal is depleted. The BE6530 is operated with a reverse bias of +4000 V applied to the n^+ surface with respect to the p^- contact, at this operating voltage drift velocities are saturated.

3.2.5 Signal Generation

The Shockley-Ramo theorem [37] demonstrates that the amplitude of any signal is independent of the location of the interaction, and can be used to determine the amount of induced charge on the electrode due to the movement of the charge carriers as detailed in Appendix A.

The weighting field of the detector depends only on its geometry and determines how the movement of charge carriers couples to a specific electrode. The electric field determines the charge trajectory and velocity of the charge carriers but as noted, saturated drift velocities are present when at operating voltage. In detectors with a

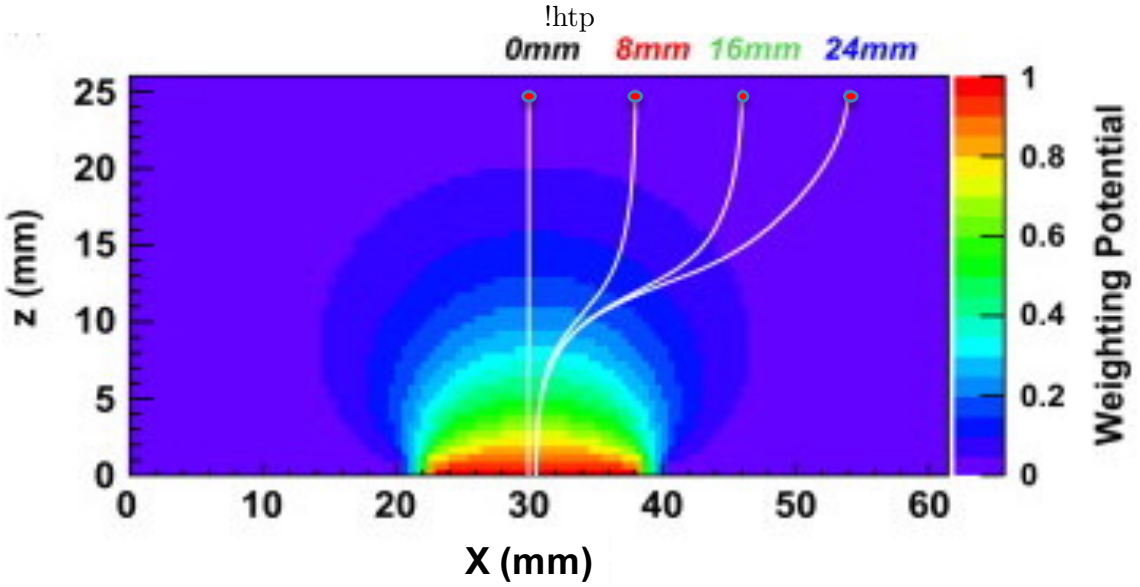

Figure 3.14: Simulated trajectories of holes for gamma ray interactions at 1 mm depth (shown as red circles), for 4 radial distances, overlaid on the calculated weighting potential. [40].

2-electrode configurations, such as the BE6530, the electric and weighting fields are of the same form. Interactions in the area of the anode result in a rapid induction of charge carriers and a signal shape with a characteristic sharp rise from the initial baseline [38, 39]. For interactions at a greater distance from the anode, the pulse shape will have a slow initial component with a longer period before a sharp rise of the signal from the baseline as the charge carriers approach the anode. The start time of an event is triggered when the holes are collected by the cathode on the cylinder surface. The end of such an event is triggered when the charge carriers reach the anode. As charge carriers drift into regions of higher weighting potential, the rate of induced charge increases. An overlay of expected drift paths on the weighting field for a BEGe detector at 4 (r,z) points is shown in figure Figure 3.14 [40]. The boundaries between colours represent the lines of weighting potential.

A signal is generated immediately after the commencement of the movement of the charge carriers and continues until all charge carriers have been collected. The signal is first processed by a preamplifier, which amplifies the signal to make it suitable for further processing. The charge from the detector is extracted by the preamplifier which

in turn gives an output voltage pulse exhibiting fast risetime and exponential decay (see Section 3.2.7). The risetime is dependent on the charge collection time and the decay tail of the signal is determined by the time constant (given by the product of the resistance and capacitance in the feedback circuit of the preamplifier). As long as the time constant is longer than the duration of the collection time, the output voltage pulse has a magnitude that is proportional to the energy deposited within the detector. An example of the output pulse from the preamplifier as a result of a 662 keV gamma ray from a ^{137}Cs point source incident on a BEGe detector is shown in Figure 3.15.

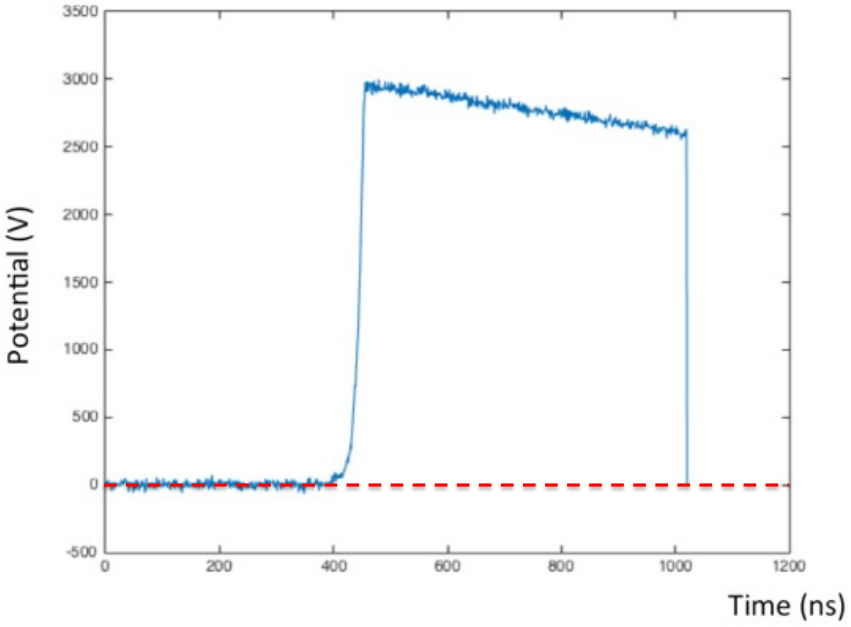

Figure 3.15: Example of a preamplifier pulse acquired from a BEGe detector, irradiated by a 662 keV incident gamma ray from a ^{137}Cs point source. The line of zero potential is shown for clarity.

3.2.6 Data Acquisition

The output from the preamplifier is processed by either analogue or digital electronics. In this thesis, data were acquired at the University of Liverpool using CAEN V1724 Digitiser

cards [41, 42]. These were chosen as, unlike analogue electronics, they offer the advantage of storing and processing the preamplifier pulses. This feature is essential as it enables the use of post-processing algorithms, such as the algorithm developed for this work. The preamplifier signal from the BE6530 is passed to a CAEN V1724 digitiser card mounted in a CAEN NIM powered crate. Signals from the V1724 digitiser are passed to a PC via a V2718 (VME to PCI Optical Link Bridge) and optical fibre connection, for online processing and storage onto disk for future offline processing. The data acquisition is controlled via a user interface on the PC, further details will be given in Section 5.2.2

3.2.7 Risetime

Throughout this thesis, the preamplifier signals will be characterised using a measurement of their risetime. The risetime of a preamplifier signal is calculated as the time taken for the signal to rise from the baseline to an arbitrary maximum of its height along the leading edge, we will use T(RT) to express risetime. Mathematically risetime is defined by:

$$T(RT) = t_{max} - t_{min} \tag{3.13}$$

where t_{min} and t_{max} are the start and finish points respectively. The value used for t_{min} can vary but for germanium detectors it is usually 5% to allow for the noise in the initial component of the preamplifier signal which is apparent in Figure 3.15 up to 420 ns. However, we will explore the values used for the calculation of T(RT) in a subsequent chapter. As an example, T90 equates to the time taken for a pulse to rise between a set value, which is typically t5%, and t90%. An illustration of a risetime calculation is shown in Figure 3.16. We can use risetime in order to parameterise the acquired data. Chapter 4 will explore employing the calculated risetime in the development of the Digital Compton Suppression Algorithm (DCSA).

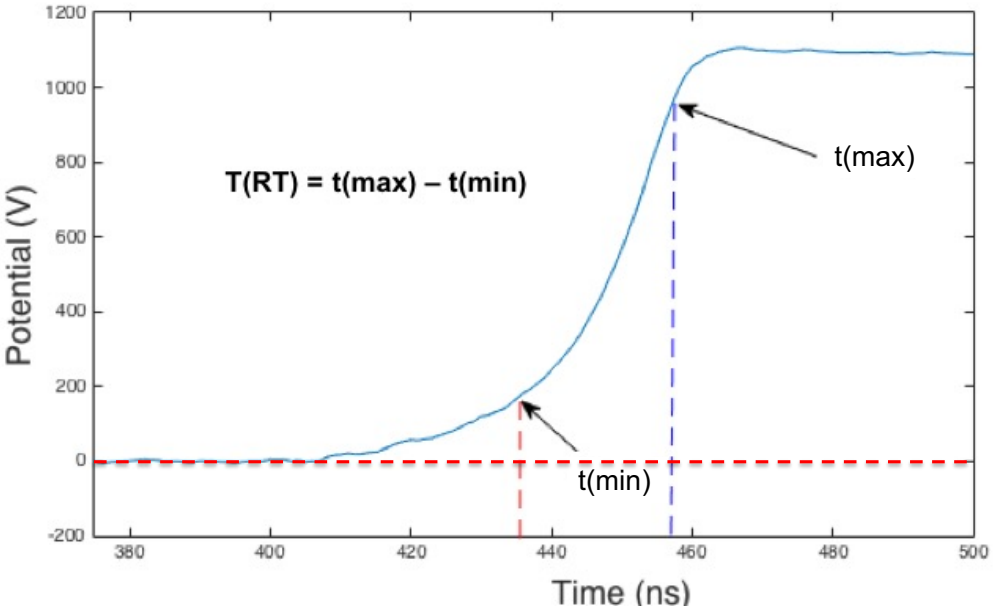

Figure 3.16: Risetime is calculated using the the time taken for the signal to rise between two values, t_{min} and t_{max} . The line of zero potential is shown for clarity.

Chapter 4

Generation of a BEGe Detector Signal Database

The DCSA will be used to enable the identification of the spatial origin of signals generated as a result of gamma ray interactions within a germanium detector. Signals that originate at different positions within the detector crystal will have dissimilar timing characteristics. The form of these shapes is dictated by the path taken by the charge carriers to their respective electrodes. An input to the DCSA is a database of signals at well known positions throughout the entire volume of the detector. Such a database of signals can be generated experimentally, however, to compile an experimental data set on a 0.5 mm^3 grid for a complete detector volume is very time consuming. As an alternative, this chapter presents the production of a theoretical signal database for the BE6530 detector using the Agata Detector Library (ADL) [10]. A subset of the signals from ADL has been experimentally validated.

4.1 Agata Detector Library

ADL was developed by the Advanced GAmma Tracking Array (AGATA) consortium to produce a theoretical signal database for germanium detectors used in the AGATA experiment. It has also been adapted and successfully used to simulate BEGe detectors [40, 43, 44]. ADL uses all of the physical principles necessary to model the generation of charge carriers, their transport through the detector and signal generation. ADL is comprised of a number of routines and the relationship between them is illustrated in Figure 4.1 (adapted from [10]). In this diagram, the blue boxes represent the user defined inputs, whilst the routines are shown in the red boxes with the final output shown in green. ADL includes an electric field solver to simulate the electric and weighting fields. To do this, the solutions to the Poisson equation introduced in Section 3.2.5 are calculated. Having generated the fields, the trajectories of the charge carriers from the user defined input positions to the electrodes can be determined.

The user inputs include parameters such as the crystal dimensions, crystal impurity doping concentration and the operating voltage of the detector. These are shown for the BE6530 detector in Table 4.2. Other parameters set in ADL include the drift velocities of the electrons and holes, which are set according to literature, as shown in Table 4.1 [45, 46]. Note that the hole mobility values along the $\langle 100 \rangle$ and $\langle 110 \rangle$ axes are different to account for the crystallographic axes of the crystal, this will be discussed further in Section 4.6. The inclusion of anisotropic mobility parameters is very important to account for the realistic behaviour in a germanium crystal [10]. The correct definition of all of these parameters is essential for the model to accurately calculate the fields, predict the trajectories of the charge carriers and the generation of the signals.

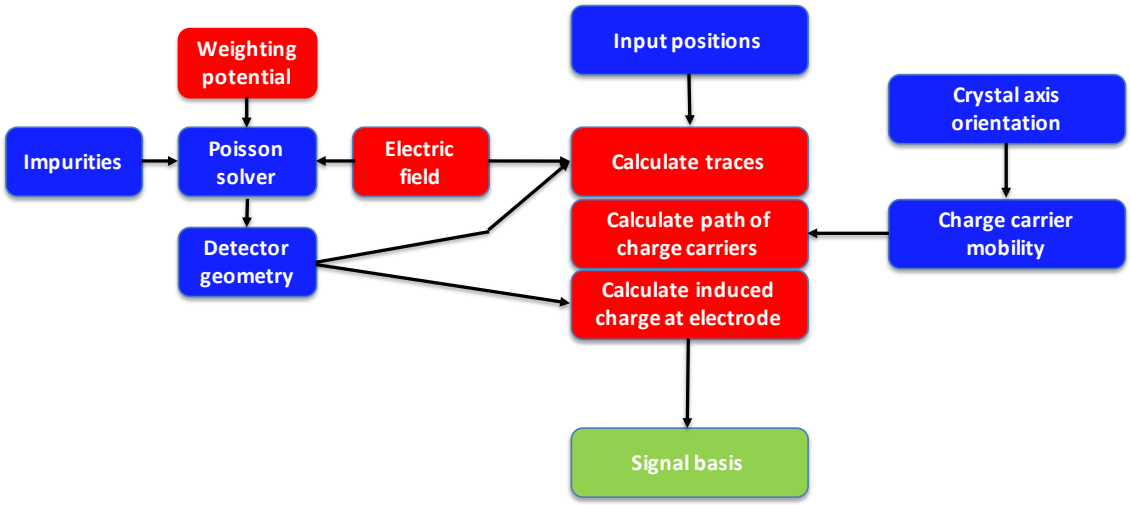

Figure 4.1: Diagram of the construction of a simulation in ADL. The routines are in red and user inputs are in blue with the final output shown in green (adapted from [10]).

ADL parameters	
Samples	1000
Sample interval	1 ns
Max number of iterations of Poisson solver	100000
Grid size	0.5 mm
Electron mobility along ⟨100⟩	
E_0 (V/cm)	507.7
μ_0 (cm^2/V s)	37165
Hole mobility along ⟨100⟩	
E_0 (V/cm)	181.9
μ_0 (cm^2/V s)	62934
Hole mobility along ⟨110⟩	
E_0 (V/cm)	143.9
μ_0 (cm^2/V s)	62383

Table 4.1: ADL parameters used where E_0 is the electric field parameter and μ_0 is the mobility fit parameter [45, 46].

4.2 Detector Geometry in ADL

For this work ADL v3.0 was used and this includes detector geometry templates for a number of detectors, including a BEGe detector. This template can be modified by the user to suit any BEGe type. The geometry for the BE6530 detector is depicted in Figure 4.2 and given in Table 4.2.

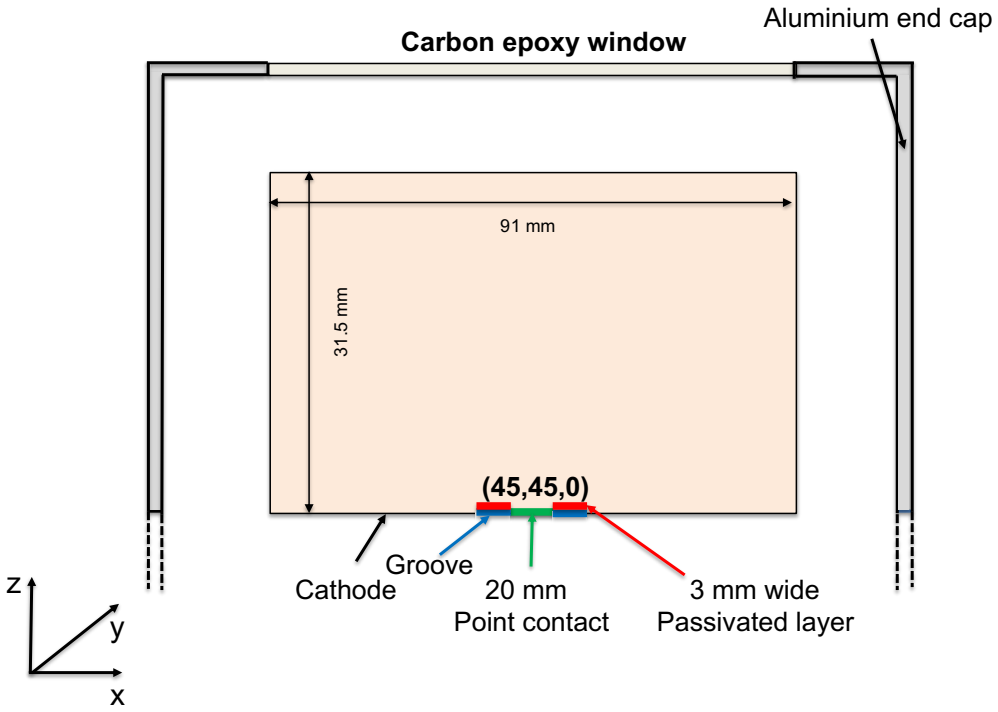

Figure 4.2: Schematic illustration of the cross section of a Mirion BE6530 Broad Energy germanium detector, the (45,45,0) coordinate and coordinate system are shown. (not to scale).

Doping type	p-type
Detector diameter	91.0 mm
Detector height	31.5 mm
Groove depth	2.5 mm
Groove inner diameter	20 mm
Groove outer diameter	26 mm
Point contact diameter	20 mm
Impurity doping concentration (top)	1.4 x 10^{10} cm^{-3}
Impurity doping concentration (bottom)	1.79 x 10^{10} cm^{-3}
Recommended operating voltage	+4000 V

Table 4.2: Geometry of the BE6530 detector.

The *Groove* refers to a passivated layer surrounding the point contact. The surface region of a germanium crystal that lies between the contacts may oxidise when exposed to oxygen or water. Such oxidised layers often contain a high density of electron states [47]. Whilst the crystals of BEGe detectors are mounted in a vacuum, manufacturers are careful to ensure that this oxidation cannot inadvertently take place during manufacture. To mitigate this situation, a chemically passivated layer is located above the insulation groove between the cathode and anode, this negates the need to manufacture the detector

in a clean nitrogen environment [48]. The manufacturer reported all of the parameters in Table 4.2 and stated that the uncertainties on the detector measurements are less than 1 mm. However, the impurity concentrations measured for the detector crystal are reported with a linear gradient but are not necessarily accurate as the manufacturer does not claim to measure the concentration accurately. This is investigated further in Section 4.4.2. Table 4.3 details the .txt files used by ADL to construct a model of a detector. Within these files, GEOMETRY.txt file includes the physical variables that are necessary for a simulation to be generated. By varying the z coordinate (relative to the point contact at the base of the detector), a 3-dimensional model can be be constructed using multiple 2-dimensional planes from the base to the top of the detector.

.tx file	Description
ADL	Main file used to set up the program and navigate to all other template files.
GEOMETRY	Defines the geometric variables used to create the geometry within the confines of the source files.
EVENT	Defines the event information.
FIELDS	Controls the electric and weighting fields and also points to location of necessary files.
DRIFT	Controls the drift parameters for the charge carriers.
READWRITE	Sets the read and write options.
TIME	Controls timing aspects of the simulation.
CONVL	Controls how the signals are convoluted with a transfer function.
TRACES	Sets up parameters used in calculating the traces.
TRAPPING	Correction parameters for trapping,

Table 4.3: Structure of ADL adapted from [10].

4.3 Weighting and Electric Potentials in ADL

In semiconductor detectors the weighting potential is described by Poisson's equation:

$$\nabla^2\varphi = \rho/\epsilon, \tag{4.1}$$

where

φ is the electric potential,

ρ is the charge density,

ϵ is the dielectric constant for the detector crystal.

However, under the application of a reverse bias there will be an absence of any trapped charges. Thus $\rho = 0$ and equation 4.1 will reduce to the Laplace equation:

$$\nabla^2\varphi = 0. \tag{4.2}$$

In orthogonal coordinates, the Laplace operator can be defined as:

$$\nabla^2 = \frac{\delta^2}{\delta x^2} + \frac{\delta^2}{\delta y^2} + \frac{\delta^2}{\delta z^2}.$$

In ADL, the electric field at any point is calculated by scaling the weighting potential of the point contact electrode by the applied bias voltage plus the field created by the space charge distribution, accomplished by taking the gradient of the electric potential at any point given by equation 4.3 [10].

$$E(x, y, z) = -\nabla\varphi(x, y, z). \tag{4.3}$$

The space charge is the uncompensated net impurity charge density of the germanium material and is calculated using the impurity doping concentration (see Section 4.2) and the potential calculated from the Shockley-Ramo theorem [37] detailed in Appendix A. The contribution of the space charge to the electric field is the calculated electric field of the distribution with the boundary electrodes set to 0V [10]. It is assumed that the impurity doping concentration has a linear gradient between the top and bottom of the crystal. As a consequence, the space charge will vary with this gradient and have an effect on the distribution of the electric field. If an assumption is made that there is no diffusion within the detector, then any charge carriers that are generated will follow the electric field lines from that point to the electrode. If a further assumption is made that the drift velocity of the charge carriers has reached a saturated level, then the position of the charge as a function of time can also be established [27].

Appendix A explains how the instantaneous induced current on an electrode is calculated and can be given by equation:

$$i = q\vec{v} \cdot \vec{E}_0, \tag{4.4}$$

where q is the charge of the carrier, $\vec{v}$ is the velocity of the charge carrier and $\vec{E}_0$ is the weighting field. In a germanium detector the weighting field is equivalent to the gradient of the weighting potential and this is calculated by ADL using a built-in 3D Poisson solver using equation [27]:

$$\vec{E}_0 = \frac{\delta^2\varphi}{\delta x^2} + \frac{\delta^2\varphi}{\delta y^2} + \frac{\delta^2\varphi}{\delta z^2} = \frac{-\rho(x,y,z)}{\epsilon_0}, \tag{4.5}$$

where $-\rho(x,y,z)$ is the space charge density and ϵ_0 is the dielectric constant for germanium. Again, because the space charge density will vary with the gradient of the impurity doping concentration, the distribution will follow this gradient.

The weighting potential, φ_0 is used to calculate the induced charge, Q on the electrode

given by equation [27]:

$$Q = q\Delta\varphi_0. \tag{4.6}$$

where $\Delta\varphi_0$ is the difference in the weighting potential from the beginning of the charge carrier path to its conclusion. The developers of ADL based this method on the technique of successive over-relaxation [49]. To achieve this, the volume of the detector, including the contacts, is divided into voxels. The weighting potential for an electrode is calculated by setting its voltage to 1 V and all other electrodes to 0 V. The solver examines a voxel and determines firstly if it is crystal material or an electrode. If it is crystal material, the solver calculates the average value of the 6 adjoining voxels plus a relaxation parameter and sets this as the new value for the voxel. The optimum solution is achieved when the value of the correction becomes constant as a function of iteration. Iterations are repeated until the defined convergence minimum is achieved. The user can specify either the minimum error or number of iterations that the solution can converge on. The iterative process stops when either criteria is met. If the voxel is an electrode, its value is left at either 0 V or 1 V.

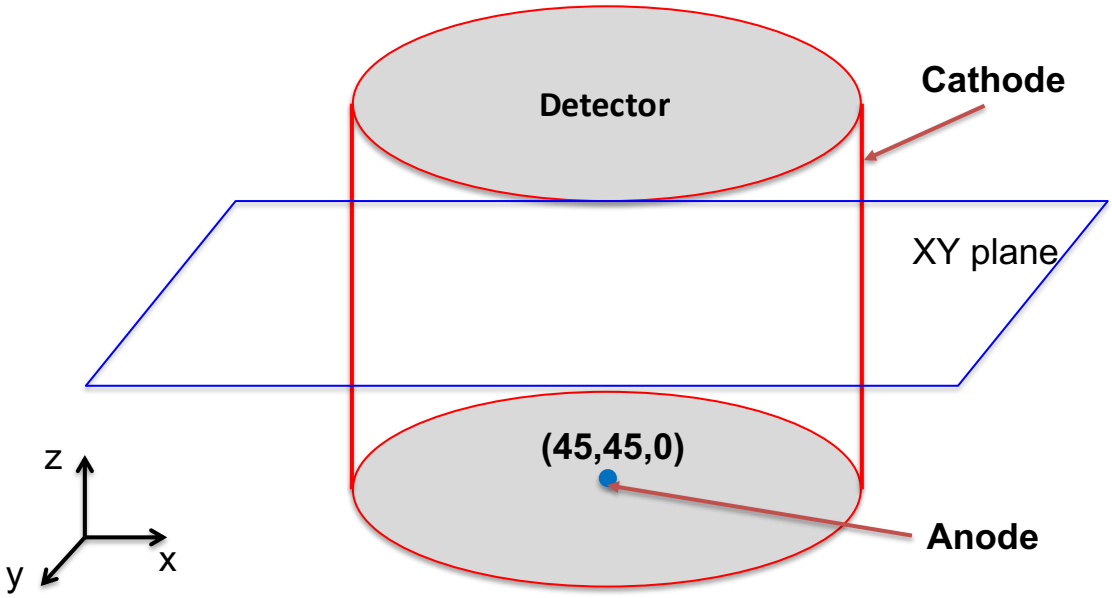

Figure 4.3: Diagram showing the coordinate system used for the ADL simulations with an (x, y) plane illustrated, the coordinate of the anode (45,45,0) and coordinate system are shown.

A diagram illustrating the coordinate system used in ADL and a sample (x,y) plane is shown in Figure 4.3. Examples of the visualised weighting potentials and electric potentials calculated using ADL for (x,z) and (x,y) planes are shown in Figures 4.4 and 4.5 respectively. The distribution that is evident in the potentials is attributable to the gradient of the impurity doping concentration, since this is used in the calculation of the space charge density, and also the electron configuration of the detector which affects the electric potential. If we first consider the weighting potential for the (x, y) plane at $z = 20$ mm (Figure 4.4b), the weighting potential is symmetrical radially about $x = 45$ mm and $y = 45$ mm. It is highest at the centre of the plane with a maximum of ~ 1.0, reducing to ~ 0.65 at a radius of 10 mm, in line with the radius of the point contact. Between the radii of the groove that surrounds the point contact, 10 - 13 mm, in which the weighting potential reduces to 0.5. Between radii of 13 and 45 mm the weighting potential drops to ~ 0.1 with an almost linear gradient. Similarly, the situation for the (x,z) plane at $y = 45$ mm is also symmetrical about $x = 45$ mm. At positions along $x = 45$ mm, the electric potential is highest at the bottom immediately above the point contact with a value of ~ 1.0, this region is slightly domed about the contact region. This domed region extends to the diameter of the point contact, 20 mm, and to a height of ~ 10 mm. Within the domed region the same rate of change as noted in the (x, y) plane exists dropping to ~ 0.65 in line with the outside of the groove. Outside of this region, the shape of the weighting potential lines takes on a bubble, the base of all of the weighting potential lines originates at the inner edge of the groove, at a radius of ~ 20 mm, with each successive bubble increasing in size. The weighting potential in these regions changes from ~ 0.65 to ~ 0.1. Similarly, the electric potential shown for the (x, y) plane through the centre of the detector in Figure 4.5b also has a complex shape being symmetrical about $x = 45$ mm and $y = 45$ mm. As expected, the potential is highest at the edge of the plane and equivalent to the operating voltage of 4000 V because the bias is applied to the cathode, diminishing with decreasing radius down to

zero. as the anode is maintained at 0V. However, the rate of change is not linear, indeed it could be described as undulating with wide regions of equal value followed by narrow regions.

This difference in rates of change between these two regions in both the weighting and electric potentials affects the charge collection characteristics in the BE6530 detector. In the outer region of the detector, the change in the drift velocity of the charge carries is low since the change in the weighting potential is small. As the charge carriers move into the region with a radius $<$ 20 mm, their path length decreases in line with the change in the weighting potential, reaching a minimum as they approach the point contact. This gives the characteristic signal that we saw in Figure 3.16, with a slow initial component followed by a steep rise. The length of the initial component is related to the distance of the origin to the point contact being shorter as the origin of the signal approaches the point contact. The BE6530 detector has a relatively large region where the weighting and electric potentials have a small rate of change. This has implications on the development of the DCSA because it creates a difficulty in distinguishing signals by their shape at radii greater than 20 mm. This will be discussed further in Chapter 5.

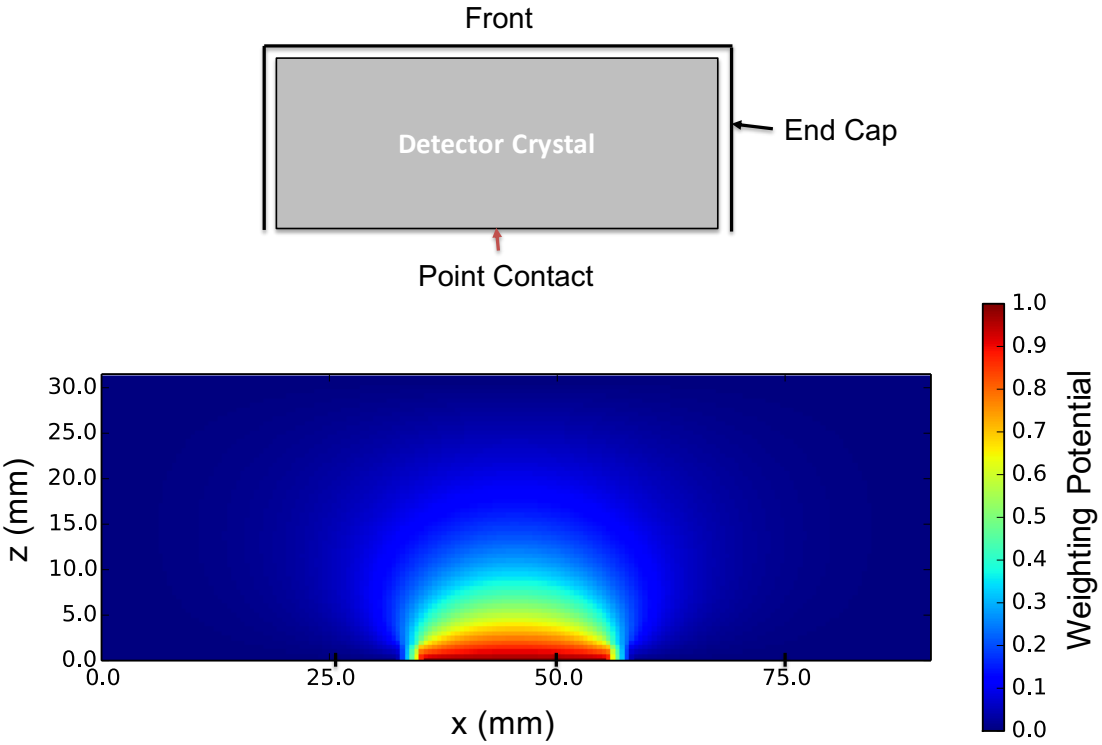

(a)

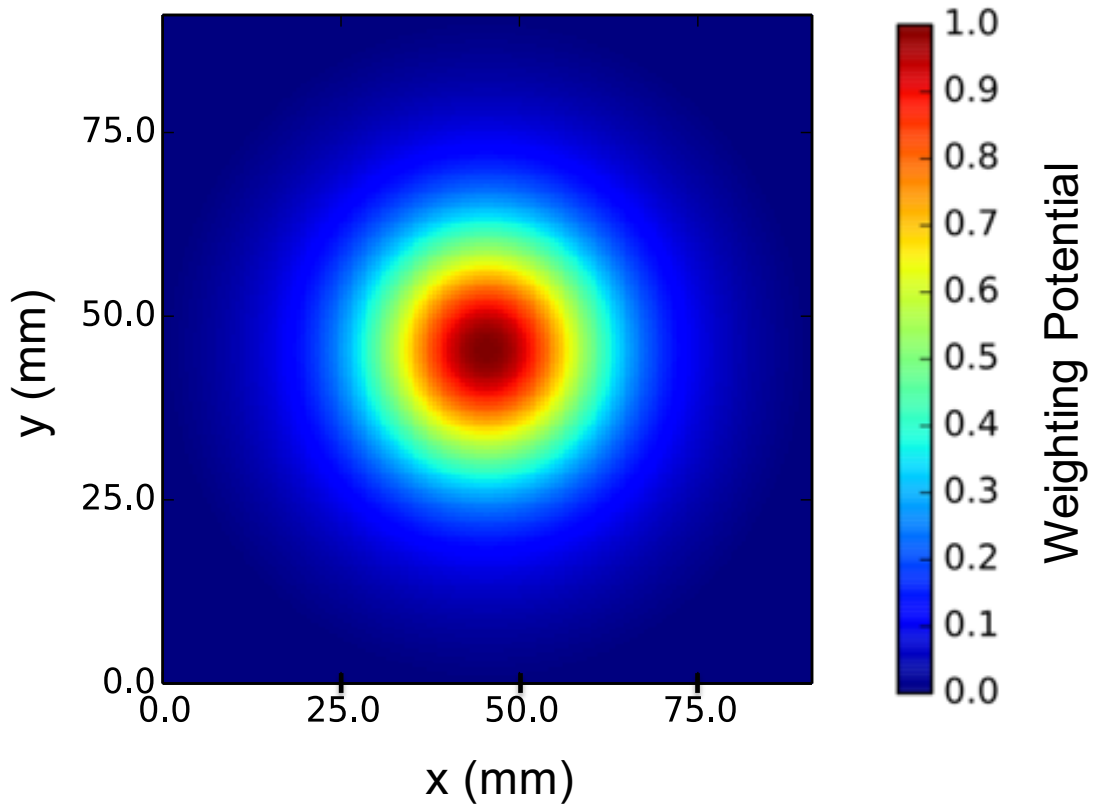

(b)

Figure 4.4: Weighting potentials calculated using ADL for (a) (x,z) plane through the centre of the detector at y = 45 mm and (b) (x, y) plane at $z = 20$ mm relative to the p^+ contact. The centre of the detector is at (45,45). A schematic of the detector is also included.

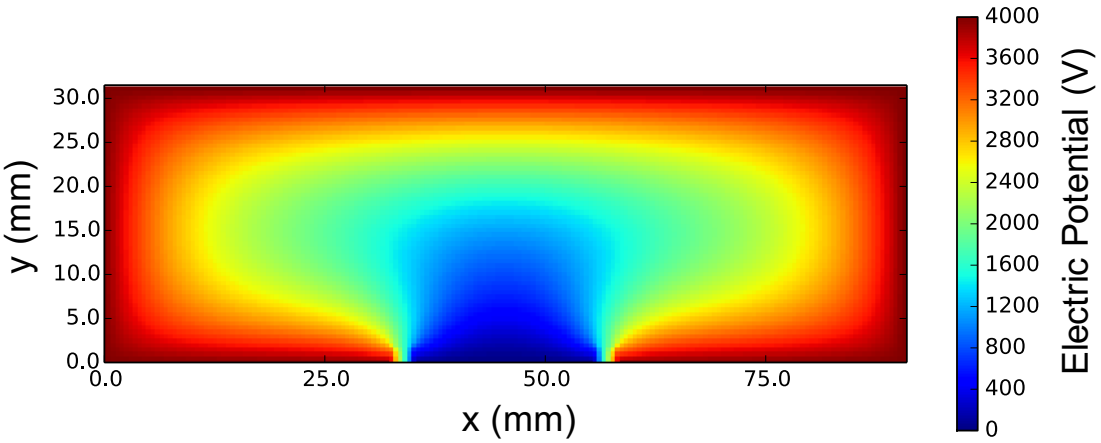

(a)

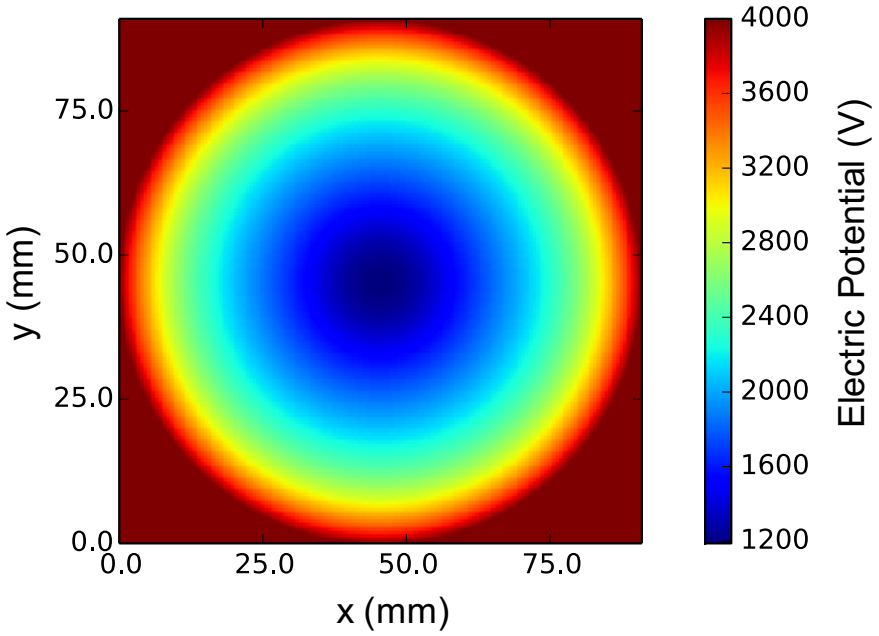

(b)

Figure 4.5: Electric potentials calculated using ADL for (a) (x, z) plane through the centre of the detector at y = 45 mm and (b) (x, y) plane at $z = 20$ mm relative to the p^+ contact. The centre of the detector is at (45,45).

4.3.1 Signal Generation

To calculate the trajectories of the electrons originating from a given (x, y, z) position, the weighting field is evaluated using the technique discussed previously. Then, for every sample interval defined in the parameters, the weighting field is calculated for the position of the electron and subtracted from the calculated value of the weighting field for the corresponding hole. The difference is multiplied by the calculated charge at this point. This process is repeated for every sample interval and for the duration of the sample length, the accumulated total forms the signal for the individual event. By repeating for signals at all positions, a complete database for the plane is generated. It is possible to develop this information for the entire volume of the detector by changing the z coordinate in the setup of ADL.

Figure 4.6 shows example signals produced using ADL representing signals originating in the bulk (blue), moving towards the surface region of the detector (green). The example signals have been produced at points along y = 45 mm for a plane through the detector at z = 20 mm. The blue plot is for a signal produced at a coordinate of (54,45), with subsequent plots at 9 mm increments along the x axis. As the value of x increases, the time at which the maximum amplitude is reached occurs later, this is because the charge carriers travel a greater distance to the point contact. For signals generated at x = 54, 63 and 72 mm, there are kinks at an amplitude of approximately 0.1 - 0.2, which is attributable to the sharp change in the electric potential around the central region, evident at a radius of 20 mm in Figure 4.4. The point at which the height of the signal begins to increase rapidly occurs later and the initial component lengthens. The sharp rise is as a consequence of the path length of the charge carriers decreasing as they approach the point contact due to the increase in the gradient of the weighting potential in this region.

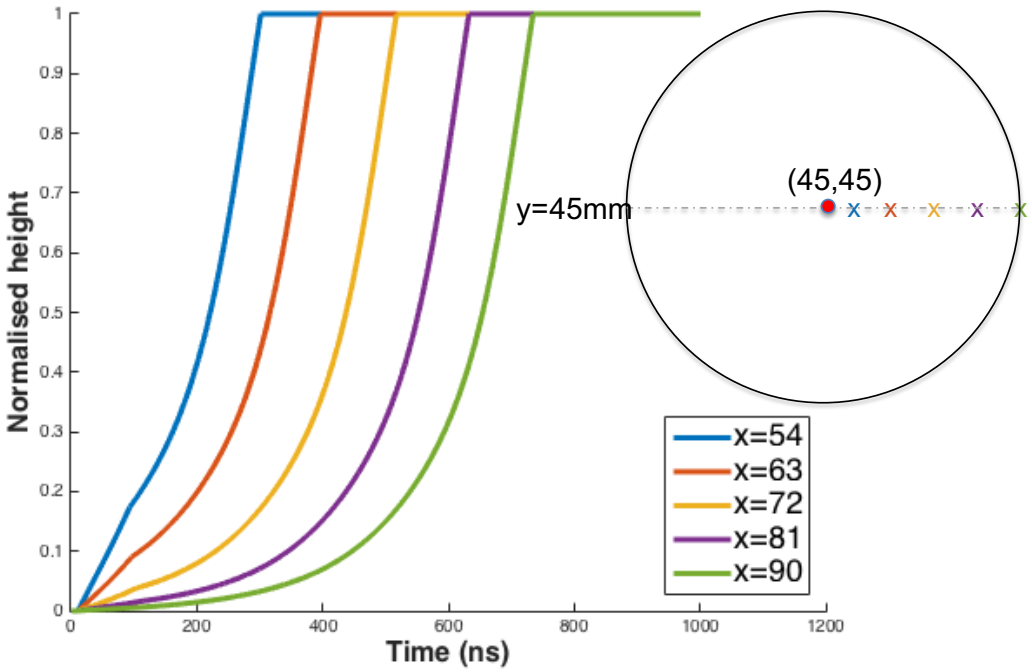

Figure 4.6: Examples of signals produced by ADL along the y = 45 mm axis in a plane at z = 20 mm above the point contact. The signal on the left originates at (54,45) with the remaining signals at 9 mm increments along the x axis. The centre of the detector is at (45,45).

4.4 Validation of ADL

The signals from ADL will now be validated using data acquired from an experimental coincidence scan of the BE6530 detector that was undertaken at the University of Liverpool by Dr C. Unsworth (University of Liverpool)

4.4.1 Experimental Coincidence Scan

Coincidence scans can be used to build an experimental database of signal shapes from a detector. This is achieved by using a primary and a secondary detector system to identify the signals, at known (x, y, z) positions, as a result of incident gamma rays that have interacted by 90° Compton scattering within the primary detector (described in Section 3.1.3). The secondary detectors are mounted around the primary. The detectors are operated in *coincidence*, such that a timing window is used to correlate any gamma

rays that interact in the two detectors. Since the photons travel at the speed of light and the close proximity of the array, the difference in time of detection is due to the timing resolution of the primary and secondary detectors. Therefore, the window must be sufficiently wide to account for the timing resolution in both detectors.

The BE6530 was used as a primary detector in a coincidence scanning system at the University of Liverpool. The BE6530 was operated at 4000 V and mounted vertically in a custom built frame, above and pointing towards a Parker precision scanning table [50]. Data acquisition was accomplished using digitisers (Section 3.2.6. A 1 GBq ^{137}Cs source was housed within a lead box with a 1 mm diameter hole in the top to act as a collimator and mounted upon the scanning table. MIDAS [51] was used to control the scanning table and act as the data acquisition software. MIDAS allows the user to define the step size and location of each scanning position together with the duration that the detector is at each position. In this way, a complete scan across the detector face may be obtained. In conjunction with the primary detector, a secondary set of Bismuth Germanium Oxide (BGO) scintillation detectors mounted in nine banks were used in the geometry shown in Figure 4.9. Each bank comprised of four BGO's mounted vertically above each other. The nine banks were placed at a fixed radius and at different azimuthal angles around the outside of the BE6530 crystal housing to give coverage across the full height of the primary detector. Each BGO was collimated by using semi-circular shaped pieces of lead separated with a 1 mm thick semi-circular shaped perspex sheet. The numbering system used for the BGO's was defined using the scheme in Table 4.4.

BGO Row #	Depth (mm)
1	29.5
2	13.5
3	20.5
4	5.5

Table 4.4: Numbering system used for BGO's in experimental coincidence scan with depths relative to the distance from the rear of the detector.

Figure 4.7 shows the layout of the equipment in the early stages of its construction. The BE6530 is visible at the top of the image whilst the lead box, containing the ^{137}Cs source and secured to the scanning table by means of chains, is visible at the bottom of the image. The start of four of the banks of secondary detectors, with one BGO detector in each, have been mounted around the BGO collimators. Four of the assemblies of the BGO banks are shown in Figure 4.8. A schematic of the experimental set-up is shown in figure 4.9 but with only 4 of the BGO detectors installed to show the z positions. In this figure, the events selected are from 662 keV γ-rays from the collimated ^{137}Cs source entering the detector and undergoing Compton scattering at 90° from their original path if they have sufficient energy and do not undergo further scattering. They can then pass through one of the lead collimators and be detected in one of the BGO's. However, it is also possible for γ-rays to scatter through any direction, not just at 90° but due to the limitations of this system, only the γ-rays that scatter through 90° and pass through the collimators are identifiable. From the Compton scattering equation (for these ideal events), the inbound 662 keV γ-rays will deposit 374 keV in the BE6503 with the remaining 288 keV of its energy deposited in the BGO. Following such an event, the (x, y) coordinates can be determined by the position of the scanning table, whilst the z coordinate is established by the BGO that has been triggered.

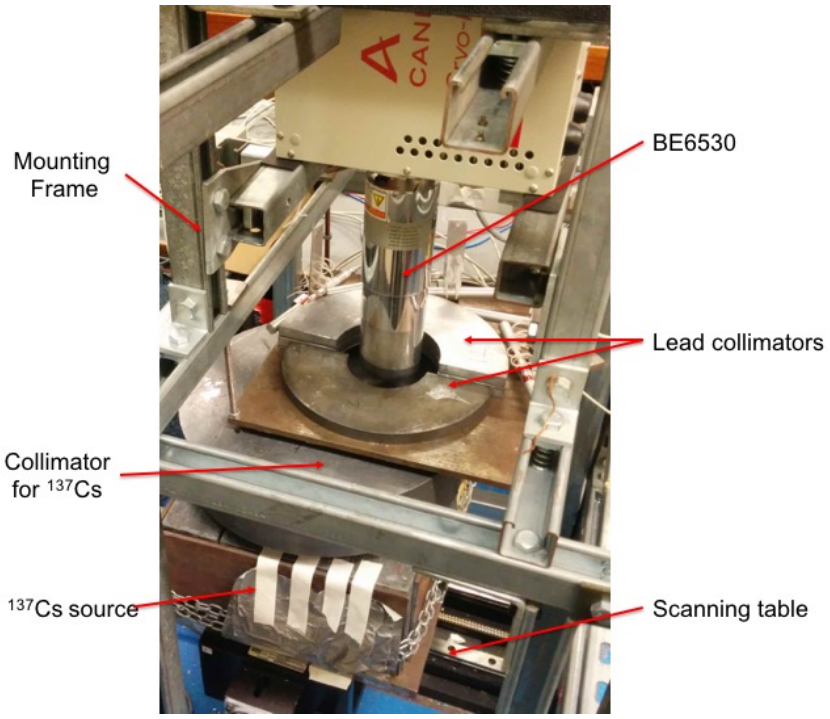

Figure 4.7: Image of experimental set-up used for coincidence scan of BE6530 detector. Four of the BGO detectors are visible together with some of the lead sheets that are used as collimators, the 1 mm perspex sheets are not quite visible.

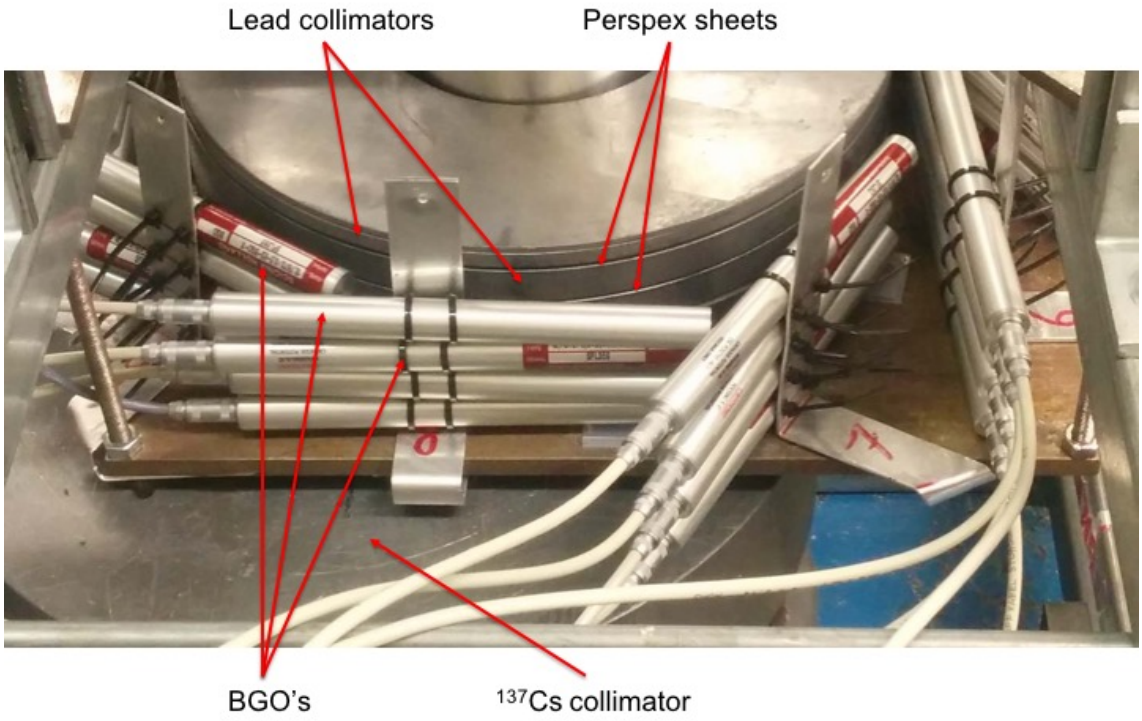

Figure 4.8: Image of four of the nine banks of BGO's assembled around the BE6530.

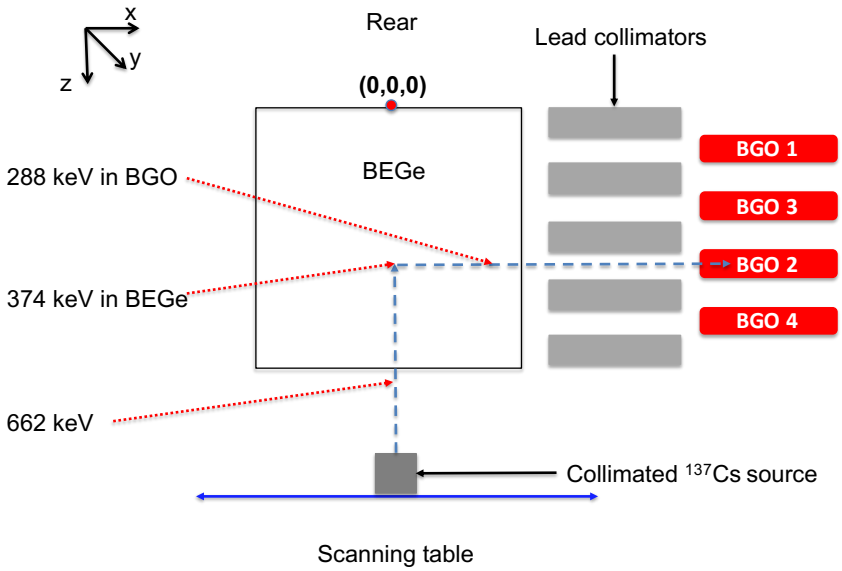

Figure 4.9: Schematic of experimental set-up used for coincidence scan of BE6530 detector. Four BGO detectors are collimated using lead blocks which in turn are separated by 1mm perspex sheets. The combination of the scanning table and BGO's enables an xyz coordinate system to be created for the detector.

Run	Date	Description
BE6530_A_12_*	7 Apr 2015	First singles front scan ^{137}Cs, 1 mm step, 2 s/position
BE6530_A_13_*	8 Apr 2015	Second singles front scan ^{137}Cs, 1 mm step, 2 s/position

Table 4.5: Singles scans run details using ^{137}Cs

Several scans were implemented in the laboratory at the University of Liverpool by Dr Carl Unsworth prior to this work. The scans used the apparatus detailed above and took place over a period of 2 months to produce a database of experimental signals at sparse positions throughout the detector volume. A mean signal was produced from the data at each of the scanning positions and these were used in the analysis carried out in this thesis work. The singles scans, which are detailed in Table 4.5, were used to establish the correct orientation of the detector relative to the scanning table and do not use a coincidence window. Two calibration runs using ^{137}Cs and ^{152}Eu were executed to enable the full calibration of the detectors. A spectrum was produced using the *Baseline Difference* energy, which is calculated from the difference in the maximum digitised trace and the baseline value (3 meV). From this, a calibration can be made using MIDAS, this was also repeated for the *Moving Window Deconvolution* spectrum. This energy is calculated by a moving window deconvolution algorithm [52]. The calibration runs were followed by a number of coincidence scans shown in Table 4.6. The runs shown in this table can be combined to give full coverage of the detector within the time constraints of the experiment.

Run	Date	Description
BE6530_A_14_*	9 Apr 2015	^{137}Cs BGO calibration
BE6530_A_15_*	16 Apr 2015	^{152}Eu Ge calibration
BE6530_13Apr15_*	13 Apr 2015	Initial test ^{137}Cs
BE6530_16Apr15B_*	16 Apr 2015	20 positions at R = 42 mm
BE6530_20Apr2015_*	20 Apr 2015	Previous run from 8/20
BE6530_22Apr2015_*	22 Apr 2015	Previous run from 11/20
BE6530_23Apr2015_*	23 Apr 2015	81 point radial scan at θ = 0,45,22.5,11.25,90
BE6530_24Apr2015_*	24 Apr 2015	Previous run continued from 5/81
BE6530_6May2015	6 May 2015	Previous run from 20/81
BE6530_11May2015	11 May 2015	30 point azimuthal 15 mm (10 points) azimuthal 44 mm (0-180 degrees)

Table 4.6: Coincidence scan run details

In order that the (x,y) coordinates can be identified, a collimated source is used with its position relative to the primary ascertained by mounting on a computer controlled scanning table. The secondary detectors are mounted at various heights about the primary detector and collimated using lead and used to determine the z-coordinate of signals that originate in the primary and have undergone Compton scattering. Any events that are identified to have occurred in coincidence in the two systems can be attributed to one event.

Data was provided for the scanning positions in Figure 4.10 giving the the (x, y) positions at z = 5.5, 13.5, 20.5 and 29.5 mm, these depths were arbitrary and purely as a consequence of the physical dimension of the equipment used. Note that, as mentioned in the previous chapter, the number of positions used to generate signals in an experimental scan is several orders of magnitude lower than that produced using ADL and is illustrated by Figure 4.10.

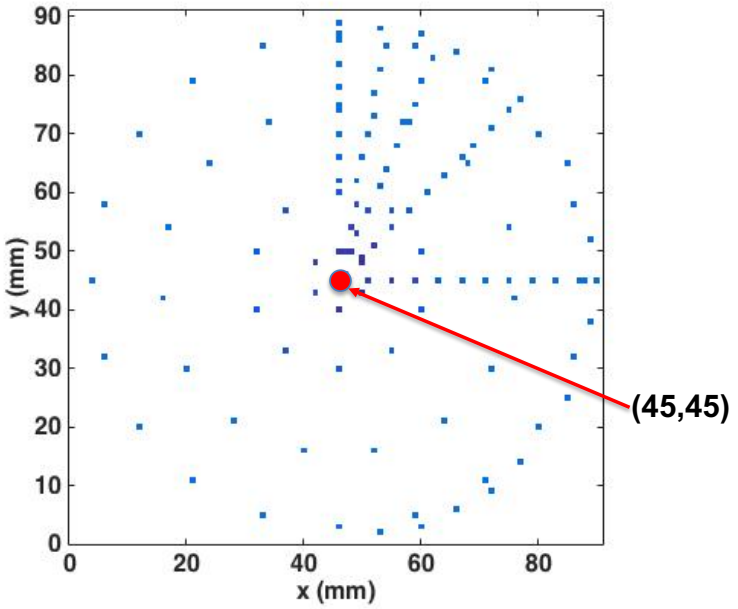

Figure 4.10: Scanning positions used in all coincidence scan runs used in Table 4.6. The centre of the plane is indicated at (45,45).

Depth #	Depth from rear of detector (mm)	Correction (mm)
1	29.5	0.003
2	13.5	0.003
3	20.5	0
4	5.5	0.005

Table 4.7: Depth correction factors for each of the four experimental depths.

To begin with, the accuracy of the measured locations of the secondary detectors used in the coincidence scan was determined. To do this, the average risetimes for T10, T30 and T90 for signals in a number of different planes for both the experimental coincidence scan and ADL data were calculated. The planes that were used were in a range of z coordinate values in and around the four depths corresponding to those used in the coincidence scan and given in Table 4.4. The absolute time difference between the combined average risetimes in each experimental plane and its corresponding counterpart in ADL were calculated. The minima found in the plots for each of the results of these calculations (Figure 4.11 and Figure 4.12) represents the most accurate value for the z

coordinate of each plane with the correction values shown in Table 4.7. However, since the collimators for the secondary detectors are 1 mm wide, these correction values are within the error on the measured z-coordinate of the secondary detectors in the coincidence scan experiment (± 1.0 mm). The depths listed in Table 4.4 were confirmed and used in in all further measurements.

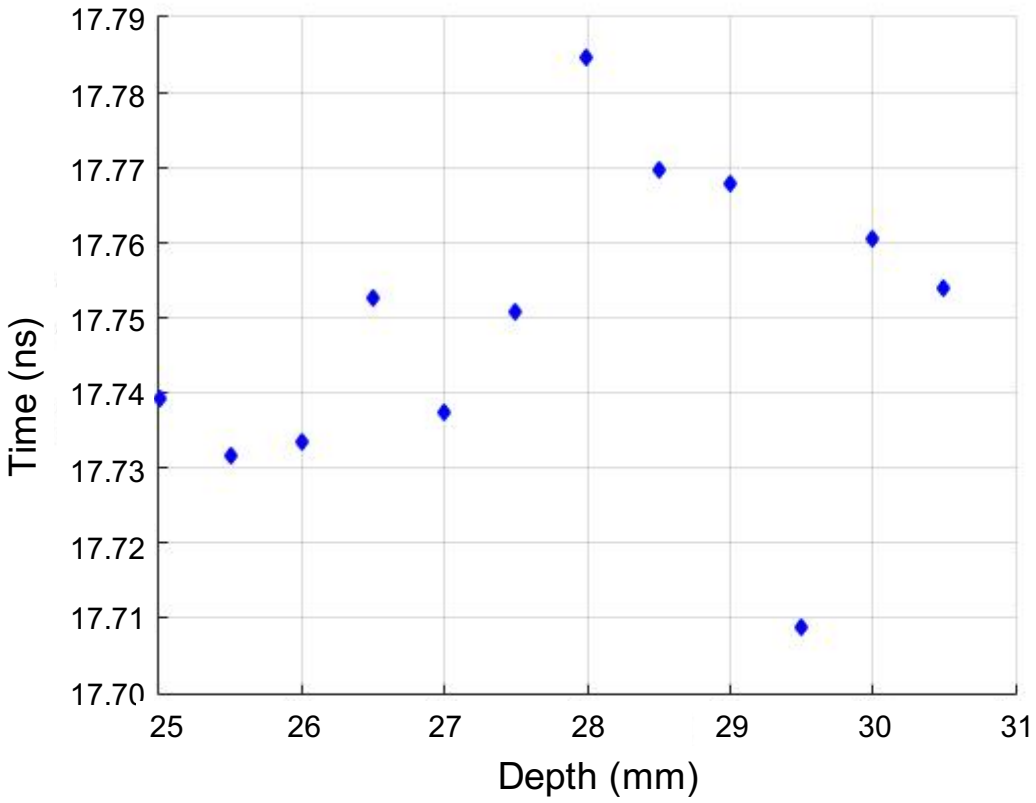

(a)

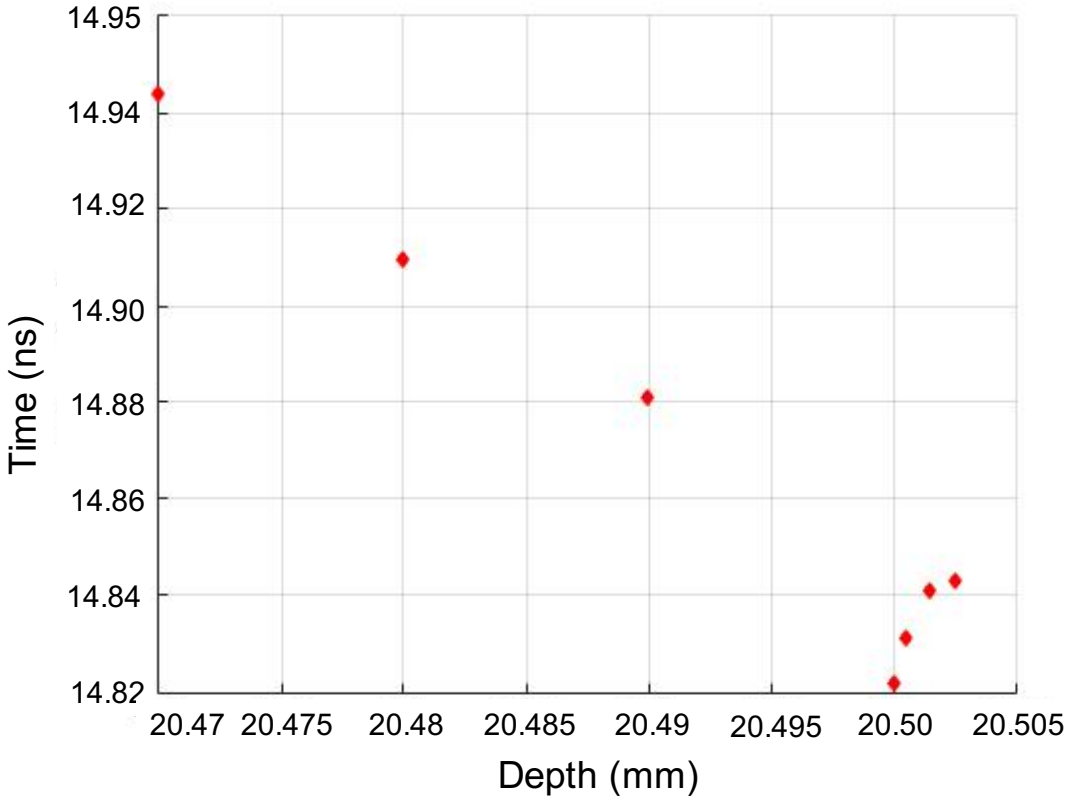

(b)

Figure 4.11: Absolute difference in risetime as a function of depth for (a) 29.5 mm and (b) 20.5 mm relative to the rear of the detector.

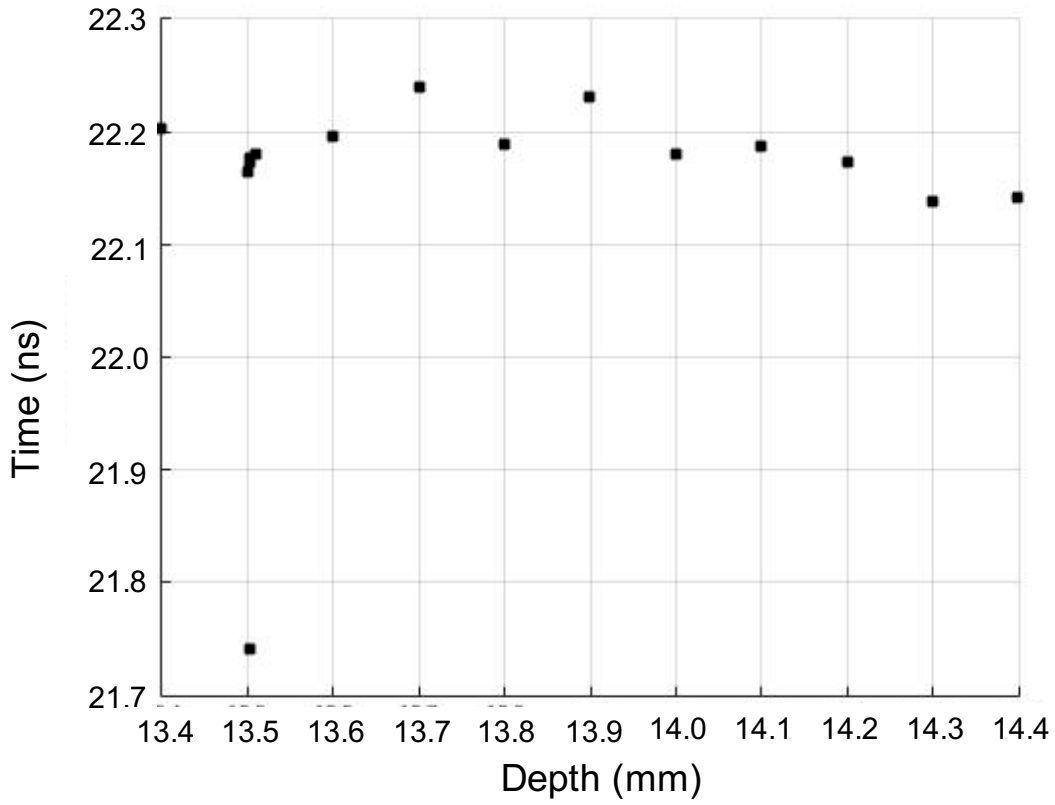

(a)

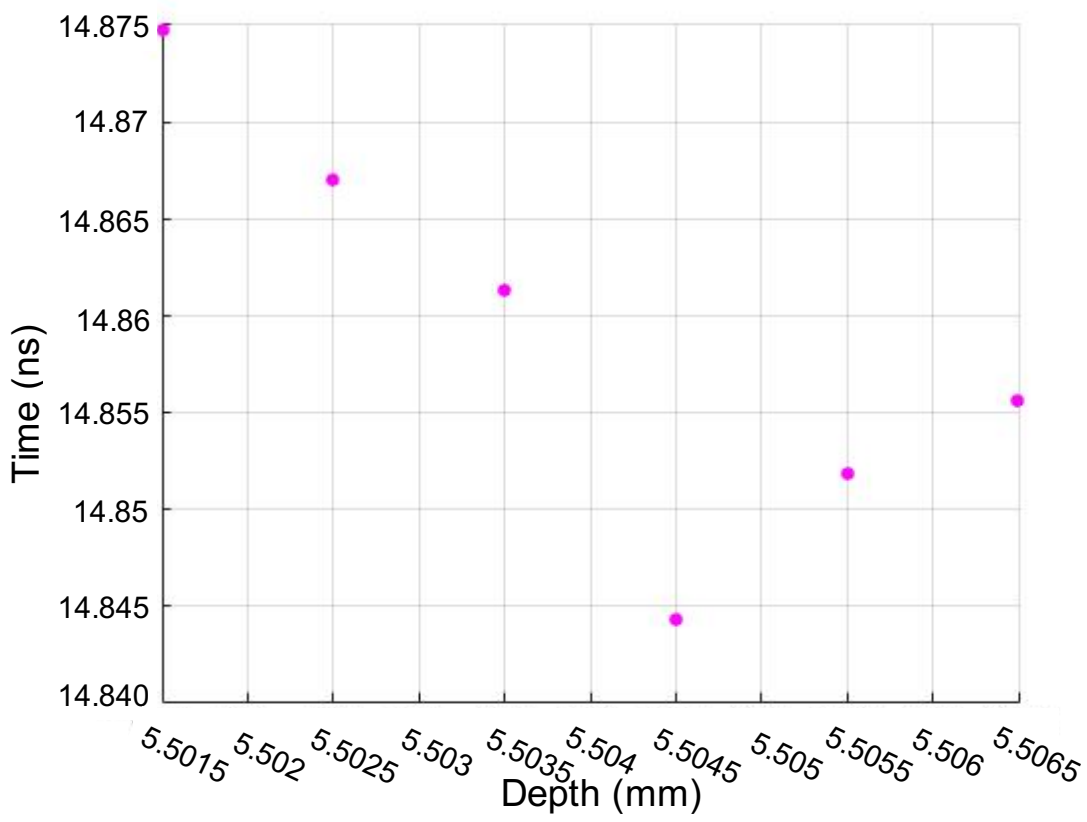

(b)

Figure 4.12: Absolute difference in risetime as a function of depth for (a) 13.5 mm and (b) 5.5 mm relative to the rear of the detector.

4.4.2 Impurity doping concentration

Impurity doping concentration was first discussed in Section 3.2.2, with Mirion Technologies Inc. supplying the values for theoretical ADL models of the BE6530 detector, as shown in Table 4.2. However, these were provided on the proviso that they are an "estimate" of the true values. As part of the validation process, the impurity doping concentration was explored using data from both ADL and the coincidence scan. The first stage of this validation process was to use the experimental and ADL data sets to investigate if it was possible to establish a more accurate value for the impurity doping concentration. To do this, the average T10, T30 and T90 risetimes were calculated using the experimental and ADL data for (x, y) planes at z = 29.5 and 5.5 mm, representing the planes at the top and bottom of the detector. The absolute difference between the average risetime for the experimental and ADL data sets was then calculated. The optimum impurity doping concentration can be established by varying its value and repeating these calculations. By plotting the combined absolute difference for all 3 risetimes for the plane being examined as a function of the impurity doping concentration, the minima found in the resultant plot equates to the optimum value for the impurity doping concentration. This is the minimum difference between the physical value in the crystal and the simulated value defined in ADL. In Figure 4.13 the results for the calculations made at depths of z = 29.5 and 5.5 mm are shown. In Figure 4.13a, the minima, at -1.4665 x 10^{10} cm^{-3}, serves as the most accurate value for the impurity doping concentration at the top of the crystal and compares well to the manufacturers figure of -1.4 x 10^{10} cm^{-3}. It is noted that in Figure 4.5a the electric potential between z = 0 to 5.5 mm and z = 29.5 to 31 mm has little variation. As already discussed, since electric potential is the gradient of the electric field which is calculated using the impurity doping concentration, an assumption is made that the impurity doping concentration is uniform in the regions between z = 0 to 5.5 mm and z = 29.5 to 31 mm.

In Figure 4.13a the value for the impurity doping concentration at the minima corresponds to the value of -1.7x 10^{10} cm^{-3} supplied by the manufacturer for the bottom of the detector. These values were used in all future calculations.

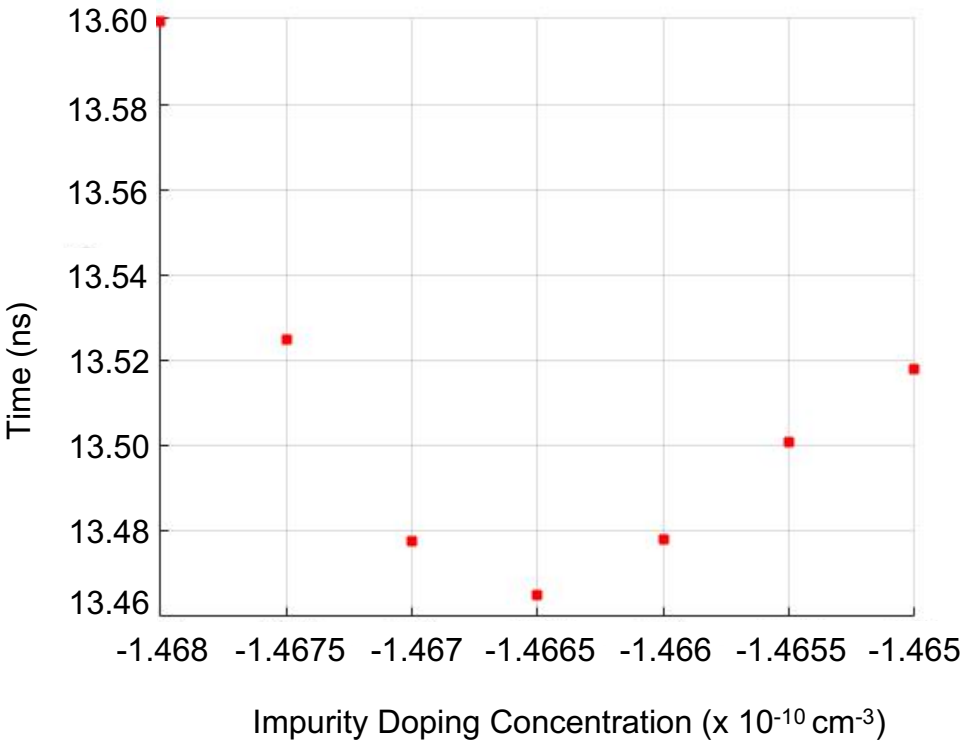

(a)

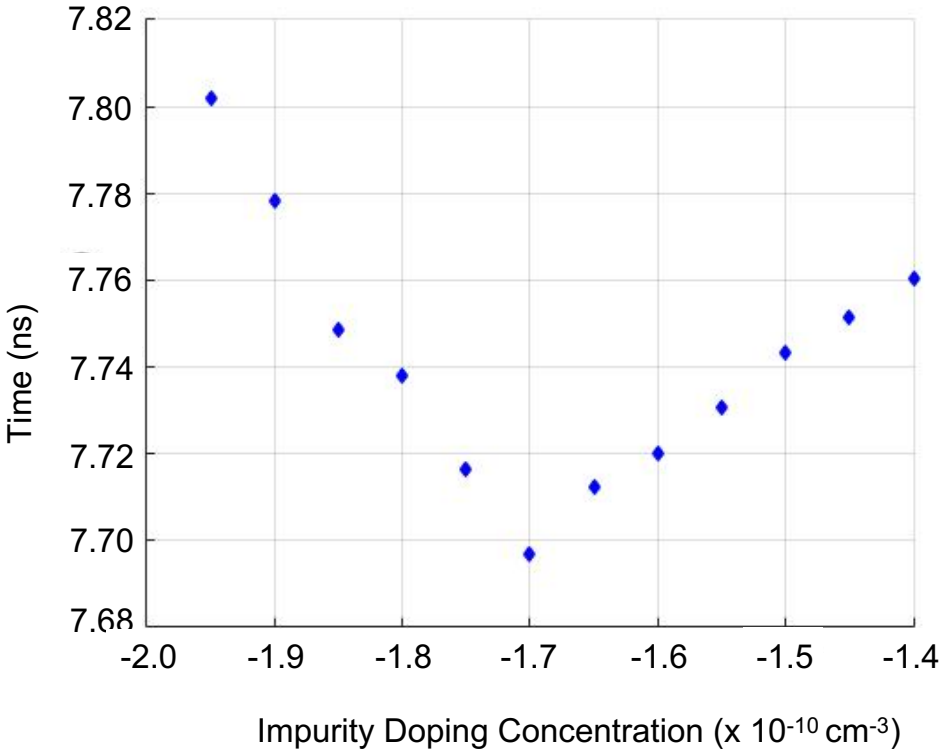

(b)

Figure 4.13: Absolute difference in risetime as a function of impurity doping concentration for (a) $z = 29.5$ mm and (b) $z = 5.5$ mm.

4.5 Risetime Comparison between ADL and Coincidence scans

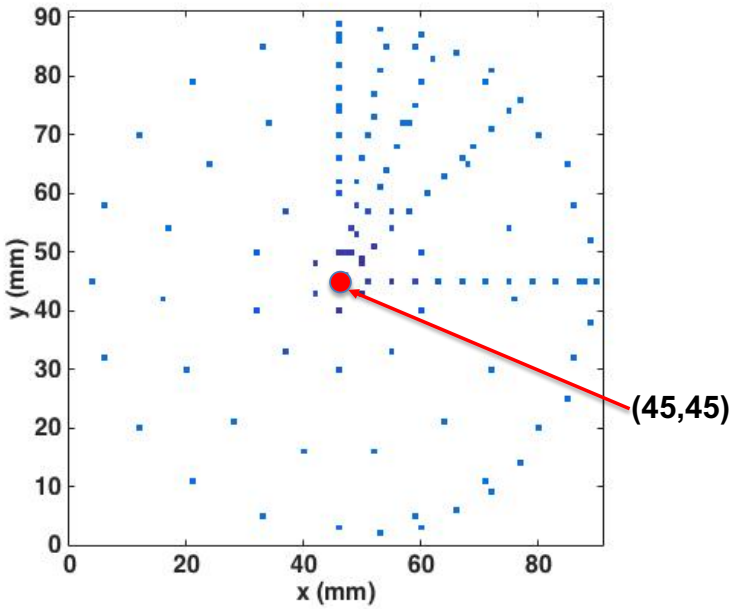

Figure 4.14: Scanning positions used in all of the experimental coincidence scan runs. The centre of the detector crystal is indicated at (45,45).

The average risetimes for each plane at the four experimental depths were calculated for the experimental and ADL data. The results, given in Table 4.8, show a faster risetime for signals that originate closer to the point contact which is due to the shorter path length of the charge carriers. Recalling that there are a relatively small number of scanning positions (shown again in Figure 4.14) for the experimental data set, we can observe that the uncertainty for each annulus will be high when compared with the ADL data as there are lower statistics in each annulus. It will be the case that some annuli will have fewer data points than others due to the scanning positions chosen. Additionally, since the assumption that the crystal is symmetrical, a full experimental data set for all quadrants was not obtained and this also lowers the statistics from the experimental data. The

standard error of the mean ($\sigma_{\bar{x}}$) has been calculated using the estimate equation:

$$\sigma_{\bar{x}} = \sigma/\sqrt{n}$$

where σ is the sample standard deviation and n is the number of observations in the sample. $\sigma_{\bar{x}}$ has been calculated for each of the average risetimes shown in Table 4.8 in each plane. In calculating $\sigma_{\bar{x}}$, it has not been possible to ascertain the uncertainty on each data point. There are some notable exceptions to this general pattern, the values for the experimental data at 20.5 mm are higher for T30 and T90 than those at 29.5 but this is more than likely an error due to the small number of scanning positions used in the experimental data (116), therefore lower statistics.

BGO Rows	Depth (mm)	Experimental Risetime (ns)						ADL Risetime (ns)		
		T10	$\sigma_{\bar{x}}$	T30	$\sigma_{\bar{x}}$	T90	$\sigma_{\bar{x}}$	T10	T30	T90
1	29.5	90	0.6	224	1.3	366	1.3	92	242	369
3	20.5	90	0.7	227	0.9	369	0.8	84	232	359
2	13.5	85	0.6	221	0.9	362	0.7	79	219	345
4	5.5	79	0.8	206	1.4	344	1.3	78	218	342

Table 4.8: Average risetimes for the experimental and ADL data sets calculated for each of the four experimental depths relative to the distance from the rear of the detector.

The results for the calculations of the average risetimes for the experimental and ADL data were all found to be consistent using the standard consistency check formula:

$$|x_1 - x_2| < \ 3\sqrt{\Delta x_1^2 + \Delta x_1^2}.$$

The experimental coincidence data was used to calculate the average risetime for 2mm annuli corresponding to the four depths in the experimental coincidence scan. The results are shown in Figures 4.16 to 4.19. It can be seen that at lower radii, the results show a fluctuation. This is due to the limited number of data acquisition positions used in this region, Figure 4.15 indicates that there are in fact only 15 data acquisition points used in this region. This is because in the coincidence scan, scanning positions were only used in

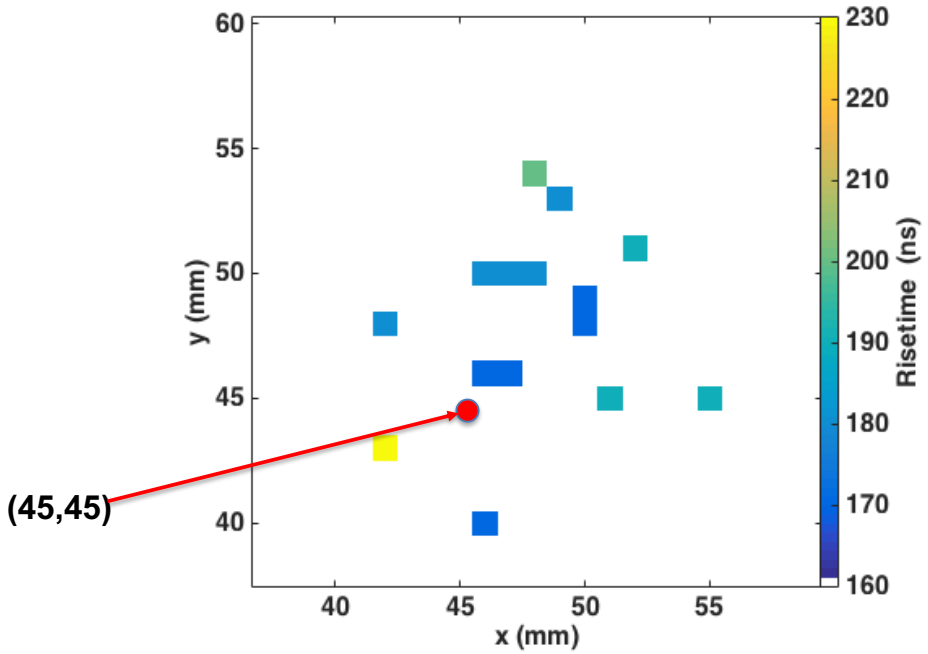

Figure 4.15: T90 calculated for all four experimental depths using a 10 mm annulus in the central region of the detector. The (0,0) coordinate is indicated.

one quadrant of the *(x,y)* plane. To compensate for these limited statistics, 4 mm annuli were used to calculate the average risetime as a function of radius for the experimental data. Using 4 mm annuli increases the statistics for each data point in this plot. The results are shown in Figure 4.20 with, as a comparison, the results for the ADL data at these depths.

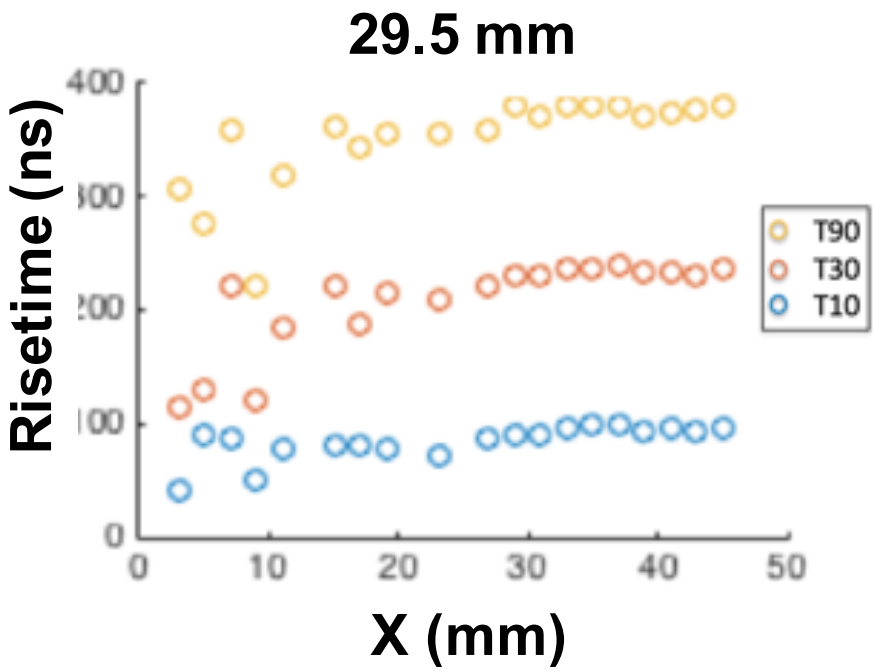

Figure 4.16: Average risetime for 2 mm annuli at z = 29.5 mm relative to rear of detector using the ADL data.

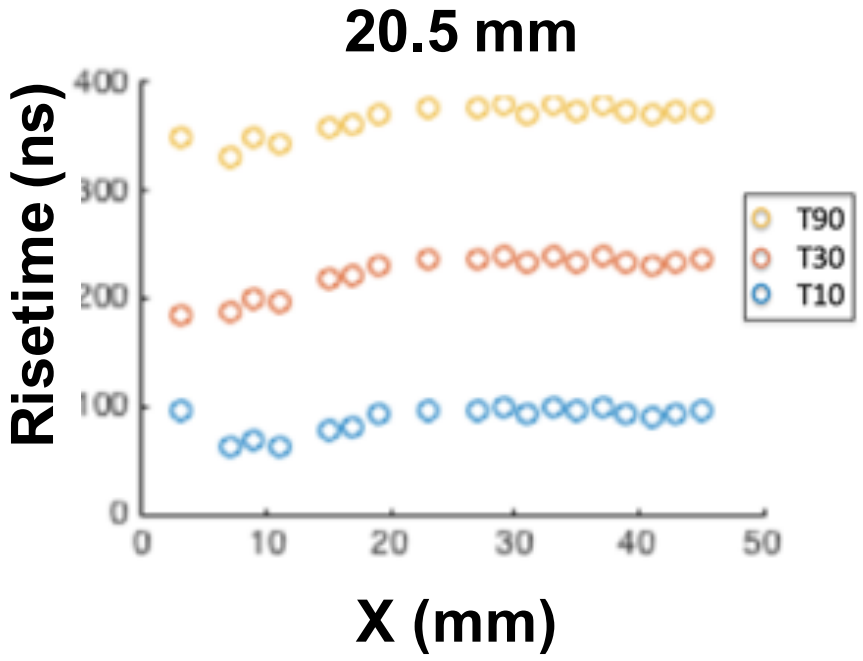

Figure 4.17: Average risetime for 2 mm annuli at z = 20.5 mm relative to rear of detector using the ADL data.

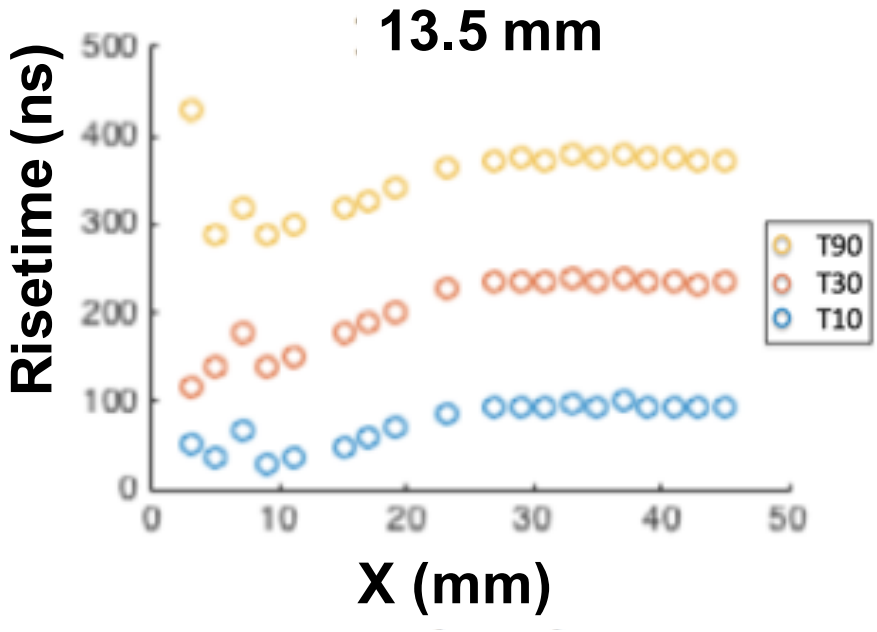

Figure 4.18: Average risetime for 2 mm annuli at z = 13.5 mm relative to rear of detector using the ADL data.

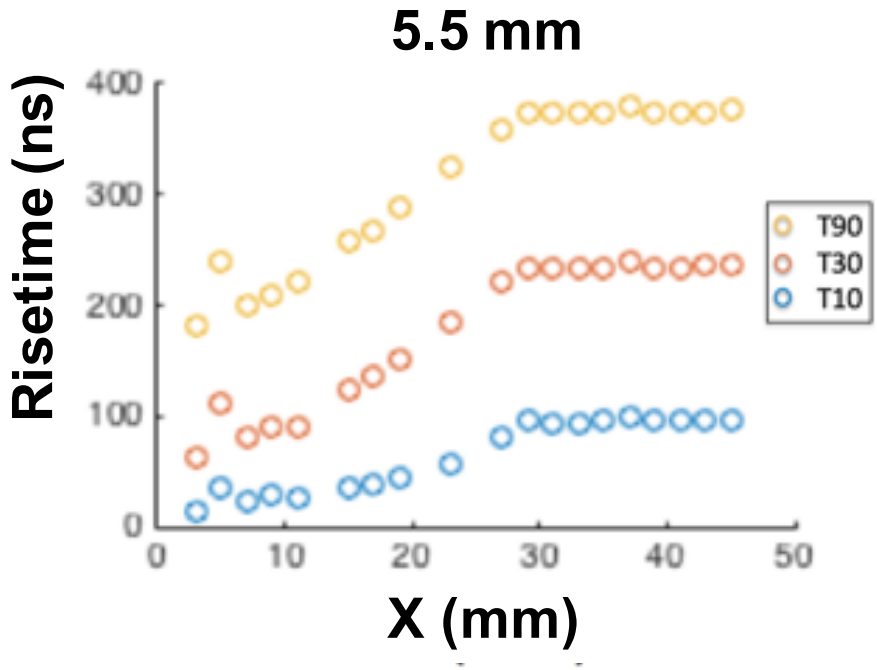

Figure 4.19: Average risetime for 2 mm annuli at z = 5.5 mm relative to rear of detector using the ADL data.

We can see that Figure 4.20 demonstrates that the results for the coincidence scan are now generally in agreement and within the errors from Table 4.8 with those from ADL in the region greater than 25 mm corresponding to the change in weighting potential

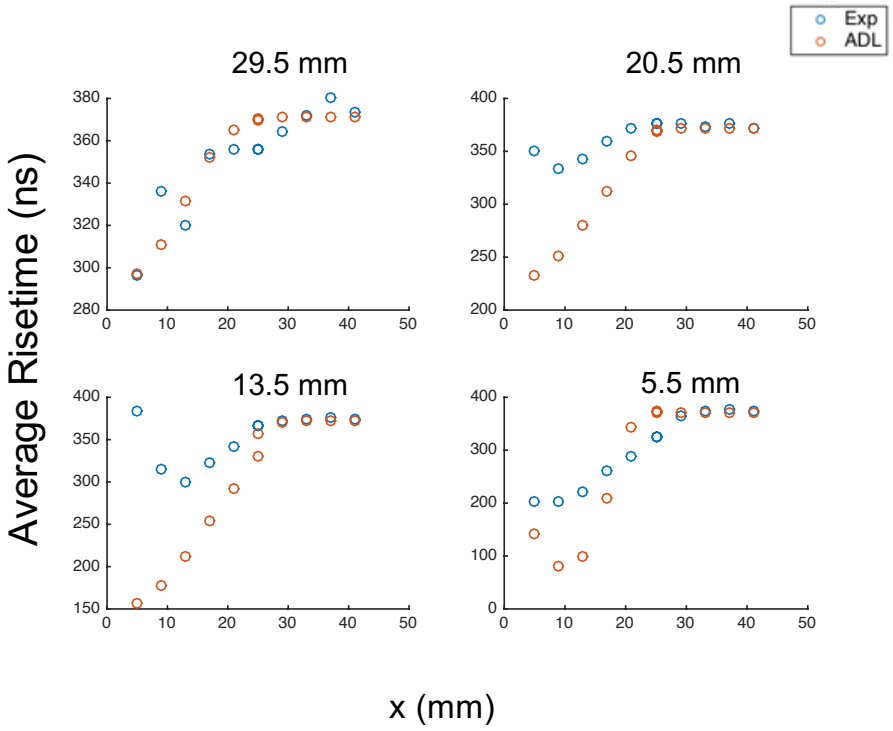

Figure 4.20: Comparison between Experimental and ADL average risetimes for T90 at 4 depths using 4mm annuli. For the experimental data, the standard error of the mean are 1.3 (ns), 0.8 (ns), 0.7 (ns) and 1.3 (ns) respectively.

discussed in Section 4.3. However, at radii less than 25 mm, there is a discrepancy between the results for these two data sets at depths 2,3 and 4. It is hypothesised that this is due to the higher number of data points that are obtained with ADL when compared to the experimental data. This could be improved by obtaining more data for this region by using more scanning positions within this region.

From Figure 4.20 it can be deduced that the charge collection times from the surface region (the region in which 90% of gamma rays from ^{241}Am interact) are approximately 11% - 15% longer than for those from the bulk region (the remainder of the detector crystal). This is fundamentally as a result of the greater distance that the charge carriers from surface interactions have to travel when compared to those from the bulk. The slow initial component of each pulse is attributable to the slow initial collection times mentioned in Section 4.3, as the charge carriers approach the area around the anode a gradual increase in the gradient of the pulses occurs. As the charge carriers move into the higher weighting field immediately surrounding the anode, the gradient of the pulse

rises rapidly before reaching a plateau at the point when the majority of charge carriers have been collected. The rate of collection then diminishes and the pulse will gradually degrade back to zero. The distribution of risetimes as a function of (x, y, z) for the four experimental depths have been calculated using the data from the coincidence scan. As an example, the results for T90 are presented in Figure 4.21. By examining this plot, we would expect that the risetime values to be highest at the edges of the four planes due to the longer path length of the charge carriers moving towards the point contact and this is indeed the case shown in this figure. Additionally, we find shorter risetimes to be found in the planes closer to the contact (depths 2 and 4) when compared to the planes towards the top of the detector (1 and 3) which is again due to the path length of the charge carriers. However, the difference between risetimes is most noticeable in the two regions discussed in Section 4.3. That is, in all four plots the risetime in the region at radii greater than 20 mm are markedly different to the risetime at radii less than 20 mm with values greater than 280 ns and less than 240 ns respectively. This is due to the gradients of the weighting potential found in these regions. These values will be used in the next chapter as the basis for developing the DCS. These results go to further show the difficulties faced when using the BE6530 detector which were first expressed in Section 4.3. That is, because the BE6530 detector has a relatively large region where the weighting and electric potentials have a small rate of change, difficulty in distinguishing signals by their shape at radii greater than 20 mm is observed.

It should be noted that ADL does not give any treatment to the preamplifier response of the detector, in an experimental signal the potential value of the pulse will decay from the maximum amplitude due to the capacitance of the preamplifier. In ADL, no decay is introduced, rather, the signal length is defined in the .txt files according to the parameter values shown in Table 4.2, this leads to the offset that has been noted. ADL also assumes that all events are single interactions and that no multiple interactions, such as those from Compton scattering events, occur.

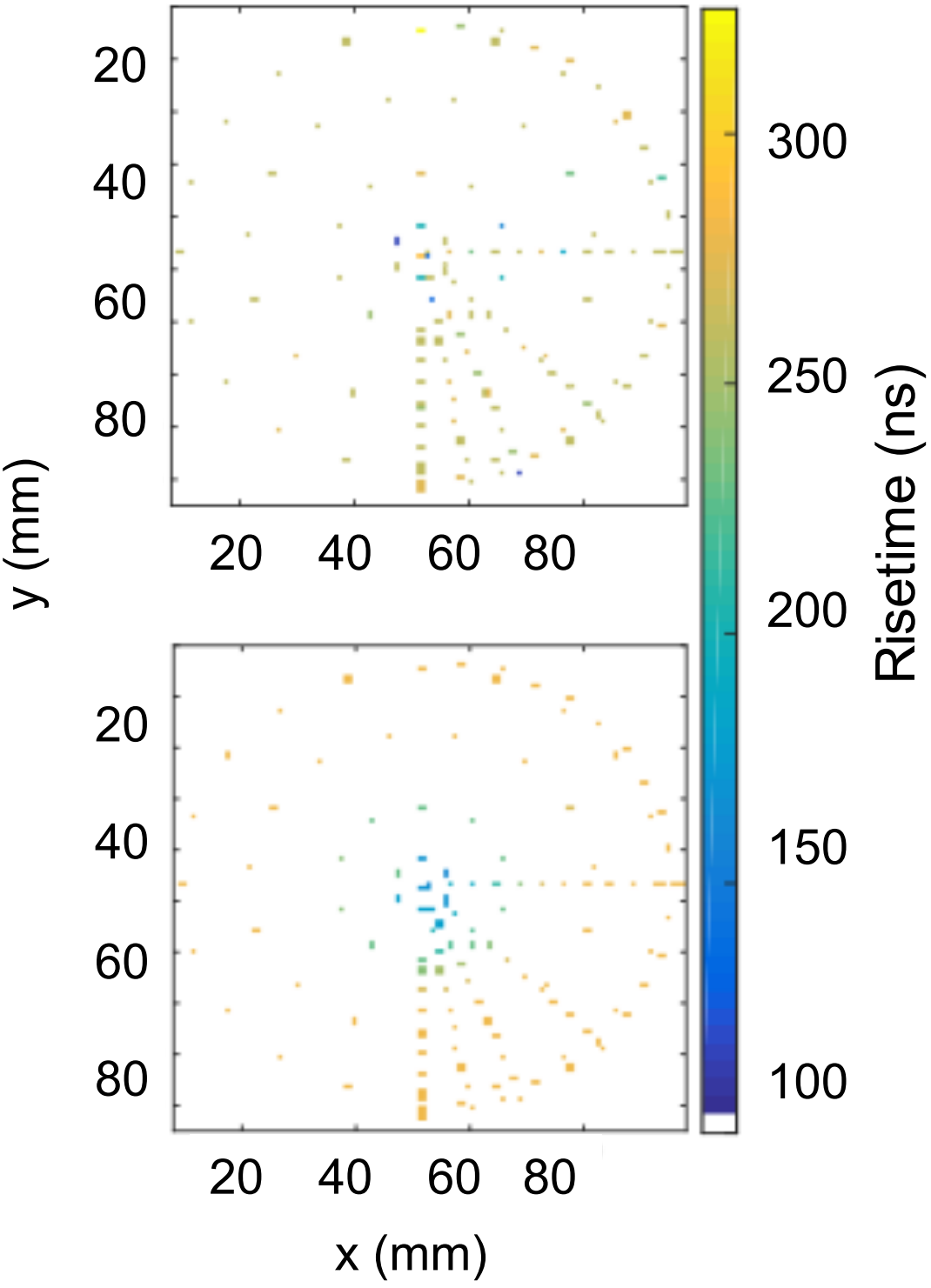

Figure 4.21: T90 Risetime map at $z = 29.5$ mm (top) and $z = 5.5$ mm (bottom) generated from experimental data. The centre of the plane is at (45,45).

4.6 The Position Dependency of Risetime

To determine the most appropriate method of discriminating between signals that originate from the surface and bulk regions, work began by exploring the use of risetime as a function of position in terms of (r, z). Figure 4.22 shows risetime calculated for signals at example (x, y, z) positions using the ADL database. Such plots will be referred to as *risetime maps* (RM) with each pixel representing the (x, y) position at which a signal within the detector plane has been produced using the 0.5 mm grid size. The plots show the calculated $T(RT)$ for signals produced at (x,y) positions throughout a z plane with lower times (in ns) coloured at the blue end of the colour range and higher times at the yellow end. These plots can be used to illustrate the effect on risetime of using different $T(RT)$ which is achieved by changing t_{max} in:

$$T(RT) = t_{min} \rightarrow t_{max} \tag{4.7}$$

and with $t_{min} = 5\%$. Although signals generated in ADL do not have any noise element, $t_{min} = 5\%$ is used because it ensures that the initial start point of the calculation is on a part of the signal that is above the noise element that would be expected in an experimental signal obtained using the BE6530 detector. In the example, a RM has been produced for $T(RT) = 90\%$, being a typical value used as it gives broad coverage of the signal. We see that the maximum risetime is 385 ns and occurs for signals at $r \gtrsim 25$ mm, at radii less than ~ 25 mm, the risetimes are shown to increase as a function of radius. The effects of the anisotropic drift velocities of charge carriers moving through the crystal as a result of the crystallographic axes of the FCC crystal [53] are evident in the region of radii $\gtrsim 25$ mm. This is highlighted by the variation in risetimes as a function of θ of the signal, with longer risetimes along the $\langle 110 \rangle$ axis and shorter risetimes along the $\langle 100 \rangle$ axis apparent. The maximum risetimes for T90 are approximately 18% higher along the $\langle 110 \rangle$ than along the $\langle 100 \rangle$ axis and with a difference of 30 ns between them.

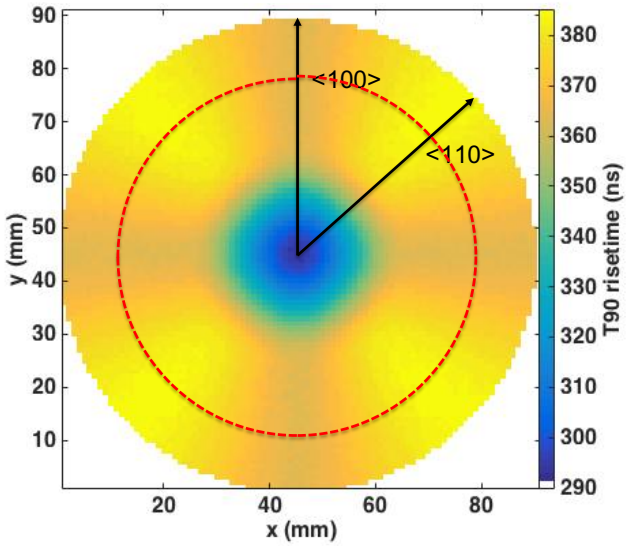

Figure 4.22: Risetime map for T90 at $z = 29.5$ mm above the base of the detector, the $\langle 100 \rangle$ and $\langle 110 \rangle$ crystallographic axes are indicated together with $r = 25$ mm. The centre of the plane is at (45,45) whilst the axes limits represent the diameter of the crystal.

To further investigate the angular dependence of risetime as a function of θ, the average risetime of all signals along a radial line from $0 \rightarrow r_{max}$ are calculated, this is repeated for all radii, the formulation is illustrated in Figure 4.23. In these calculations, An example of the results of these calculations for a plane at $z = 20.5$ mm are shown in Figure 4.24 where increments of $\theta_{step} = 1.8°$ have been used. The distribution in this plot reveals local maxima and minima corresponding to the $\langle 110 \rangle$ and $\langle 100 \rangle$ axes respectively. We can also note that, as a consequence of the pixellation that occurs in the ADL data, rather than a smooth curve between maxima and minima, there is a stepped curve. The maximum risetimes of ∼90, 235 and 360 ns for T10, T30 and T90 respectively are calculated and corresponds to the signals along the $\langle 110 \rangle$ axis. The corresponding minima are for signals along the $\langle 100 \rangle$ axis and are ∼40, 95 and 145 ns respectively.

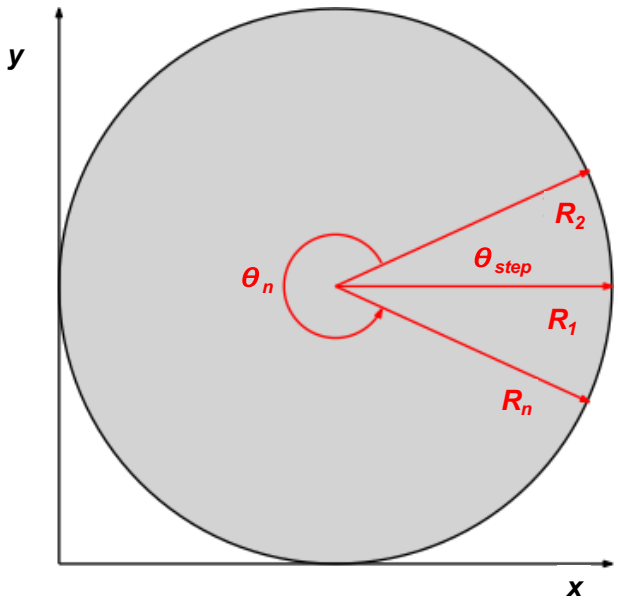

Figure 4.23: Illustration of the method used for the calculation of average risetime along each radial position (r) using a step size θ.

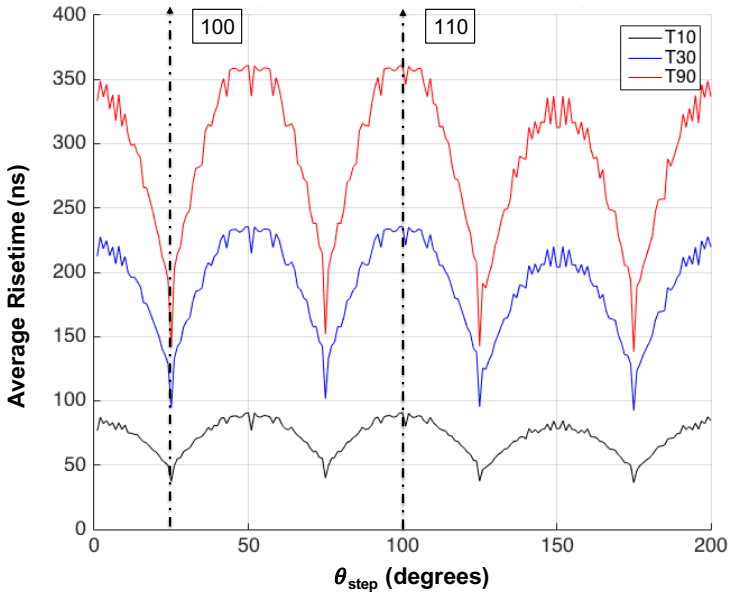

Figure 4.24: Average risetime calculated for T10, T30 and T90 as a function of θ_{step} at $z = 29.5$ mm above the base of the detector. The crystallographic axes are overlaid and correspond to the maxima and minima.

Figure 4.25 shows the RM for T30 and T90 produced for an (x, z) plane through y = 45 mm and using $t_{min} = 5\%$. In Figures 4.22 and 4.25 it is apparent that the risetime is dependent on the distance of the origin of the signal from the point contact at the base of the detector. In Figure 4.25a risetimes up to $\sim$ 75 ns (T30) are distributed in areas that resemble an arrowhead shape above the point contact for $35 < x < 55$ mm. Longer

risetimes of 55 to 260 ns are observed in the outer region at $x <$ 35 mm and $>$ 55 mm. This distribution is explained by the changes in the gradient of the weighting potential that we examined previously and shown in Figure 4.4a. In Figure 4.25b, the same pattern is observed below $z = 25$ mm and a risetime above 125 ns, with the exception of an area of 5 mm^2 located above the point contact which is again attributable to the gradient of the weighting field in this region. The white pixels along the bottom of the images are non active regions corresponding to the positions of the passivated layer about the point contact region discussed in Section 4.2.

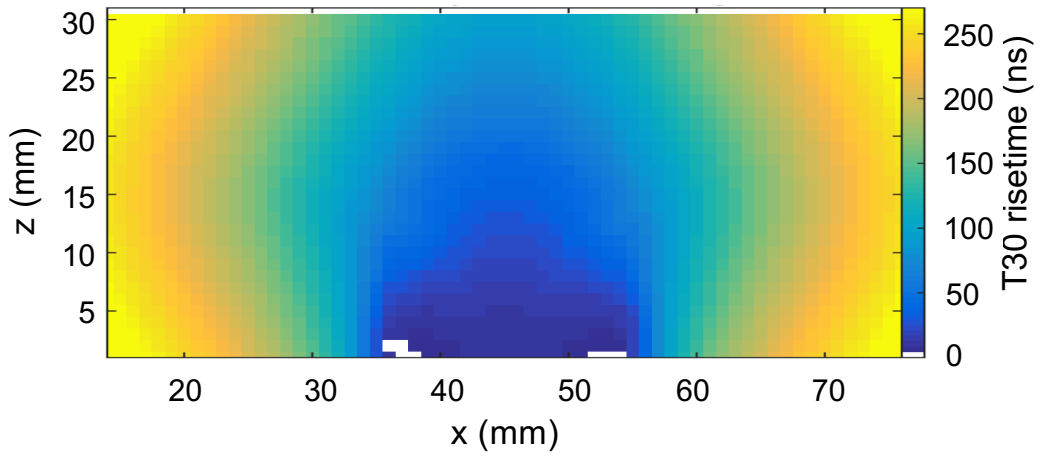

(a)

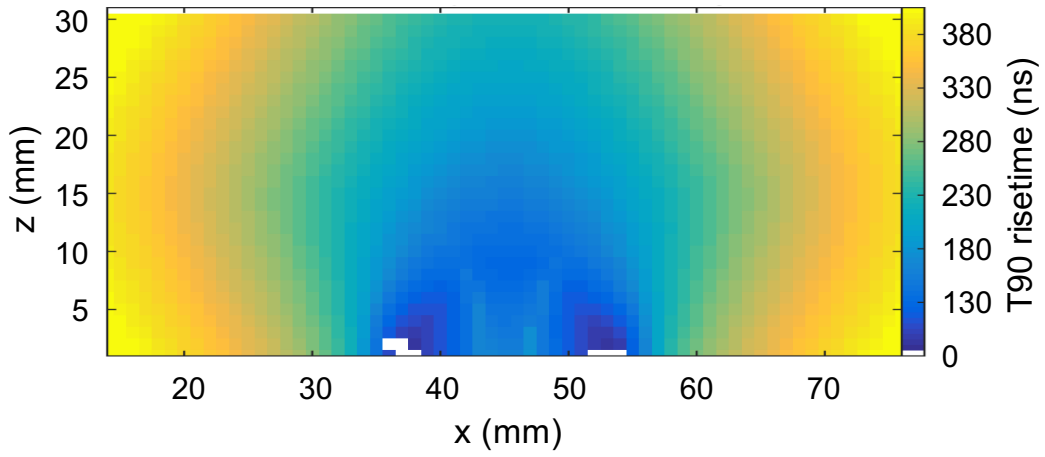

(b)

Figure 4.25: Risetime maps for (x, z) planes through the centre of the detector at y = 45 mm for (a) T30, and (b) T90.

4.7 Summary

ADL has been used to generate a database of signals. A subset of these signals, corresponding to four depths used in an experimental coincidence scan, have been chosen for validation. The ADL data has been obtained using a 0.5 mm grid for the (x,y) planes corresponding to the four experimental depths whereas the experimental data has been obtained at selected positions. Despite the discrepancy in the amount of data used in both scenarios, ADL has been shown to be in good agreement with the experimental data and is a valid tool to use for the development of the DCS. The position dependency of risetime has been shown and this will be used in developing the DCSA with the aid of ADL and will be discussed in the next chapter.

Chapter 5

Digital Compton Suppression Algorithm Development

The DCSA has been developed with the aim of achieving Compton suppression in the BEGe detector without operating it in coincidence with auxiliary detectors. The DCSA will be used to identify if a gamma ray interacts in the bulk or surface of the crystal. It is based on the knowledge that low energy gamma-rays, such as the 60 keV gamma rays from ^{241}Am, will only interact in the surface of the detector, whilst higher energy gamma rays from the background and sources in the waste stream (i.e. ^{60}Co and ^{137}Cs) will interact throughout the detector. The goal is to achieve the best Minimum Detectable Activity (MDA) for the BE6530 detector. To accomplish this, the DCSA has been tested using the ADL signals database presented in Chapter 4. This chapter will outline the optimisation method and results.

5.1 Average Risetime

Although a complete database of signals has been produced using ADL, it is not computationally efficient to search through the entire database to determine gamma ray

interaction positions. It can be seen in Figures 4.22 and 4.25 that the risetime varies as a function of position across (x,y) and that the BE6530 detector has (x, y) symmetry, because of this the "average " behaviour can be investigated. Whilst this method has larger uncertainties, it is computationally more efficient, which is important for in-situ counting measurements. The risetime, $T(RT)$, of each signal is calculated and represents the time taken for the signal to rise from 5% to a percentage of its maximum height along the leading edge. Since surface signals correspond to large radii and bulk to lower radii, the risetime as a function of (r, z) has been investigated. The average risetime for all signals at (x, y) positions within numerous defined annuli at specific z planes has been calculated. The effects on average risetime due to the crystallographic axes will be discussed later in this section. A schematic illustration of 10 of these annuli are shown in Figure 5.1. By calculating risetime as a function of (r, z) throughout the detector, it is possible to develop an algorithm to discriminate between surface and bulk signals that is based on the risetime of signals.

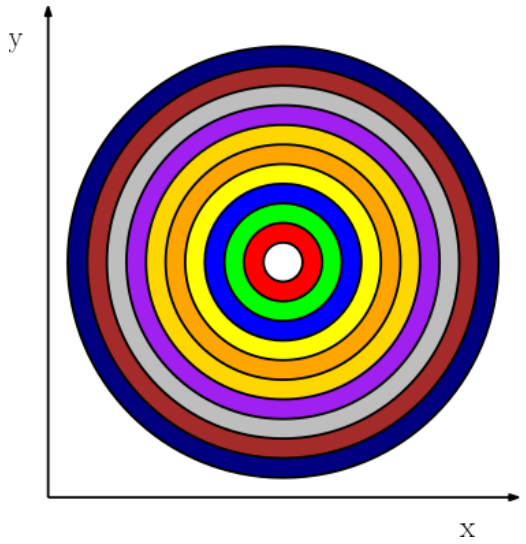

Figure 5.1: Illustration of example radial annuli in an (x, y) plane used in the average risetime calculations. The figure is indicative only and not to scale.

The average risetimes for $T(RT)$ = T10, T30 and T90 have been calculated for 4 mm wide annuli for (x, y) planes at z = 5.5, 15, 20.5 and 29.5 mm above the contact. We would expect the average risetime at low radii to be faster than large radial positions because the drift path length for charge carriers will be shorter in the central region than

those at the edge coupled with higher drift velocities. This can be seen in Figure 5.2 and Section 5.1. We can note that the results shown for T10, T30 and T90 follow similar trends at all depths. These results indicate lower risetimes at the centre of the plane, increasing with greater radial position. Whilst these results have been produced using increments of $z \simeq$ 5 - 10 mm, there isn't any significant change other than a shifting of the peak/plateau region towards larger radii. The position dependence of risetime can be established throughout the volume of the detector by repeating this method and using smaller increments in the value of z.

It is noted that there is an apparently anomalous region in which the average T90 is higher at $r = 5$ mm, highlighted in red in Figure 5.3. In previous work by a collaborator [54], this region was examined using weighting field models for the detector which revealed a significantly longer path length for the electrons in comparison to the path length for the holes in the area of the point contact between $x = 0$ and 10 mm (Figure 5.4). It was concluded that the increase in risetimes in this region could be attributed to the tendency of the charge carriers to drift towards the front face of the crystal rather than towards the outer area around the passivated layer Figure 5.4. For the electrons created as a result of signals in areas that are further away from the centre, their drift paths tend to be towards the bottom of the crystal at $z = 0$. In the ADL model for the BE6530, this central region extends to a radius of 12mm. The longer path length for electrons created as a result of gamma ray interactions in the central region results in higher risetimes for these signals, in particular for T90. This is less evident in the models for T10 and T30 and is indicative that the initial part of the charge collection process in the central region above the contact is more consistent across the early part of the signal than in the latter stages. The same effect is not noticed for planes that are further from the contact and this is attributable to the greater uniformity in the weighting field at higher z.

Figure 5.5 shows the average risetime calculated for T10, T30 and T90 using 4 mm

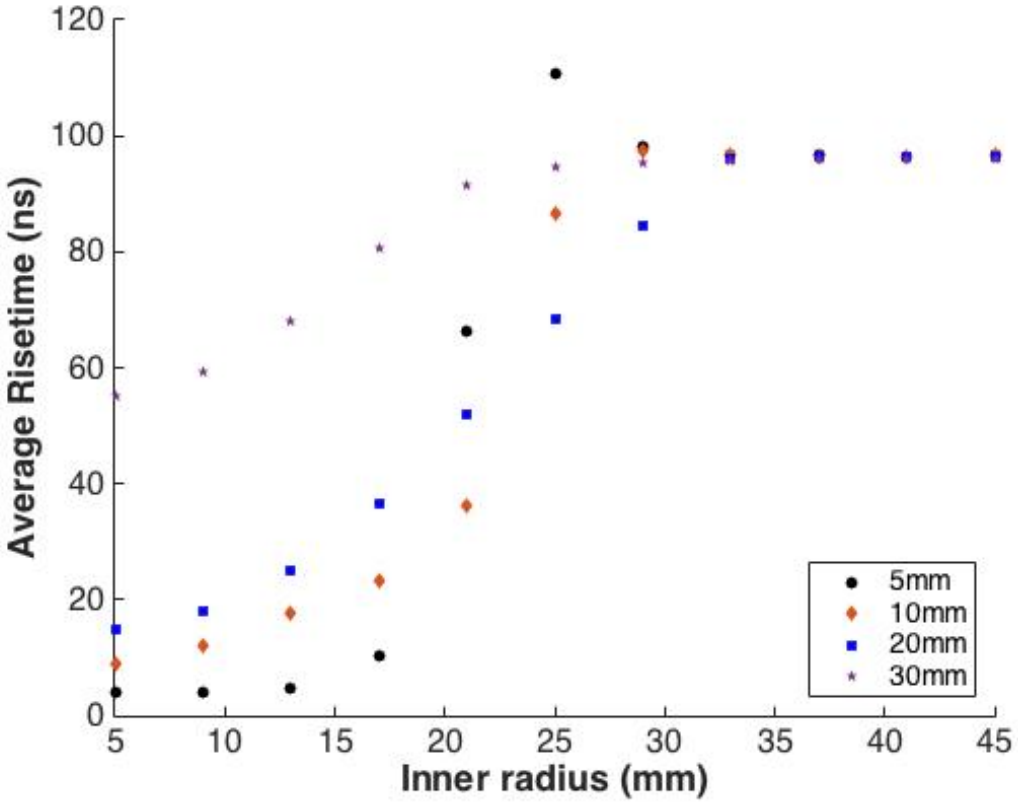

(a)

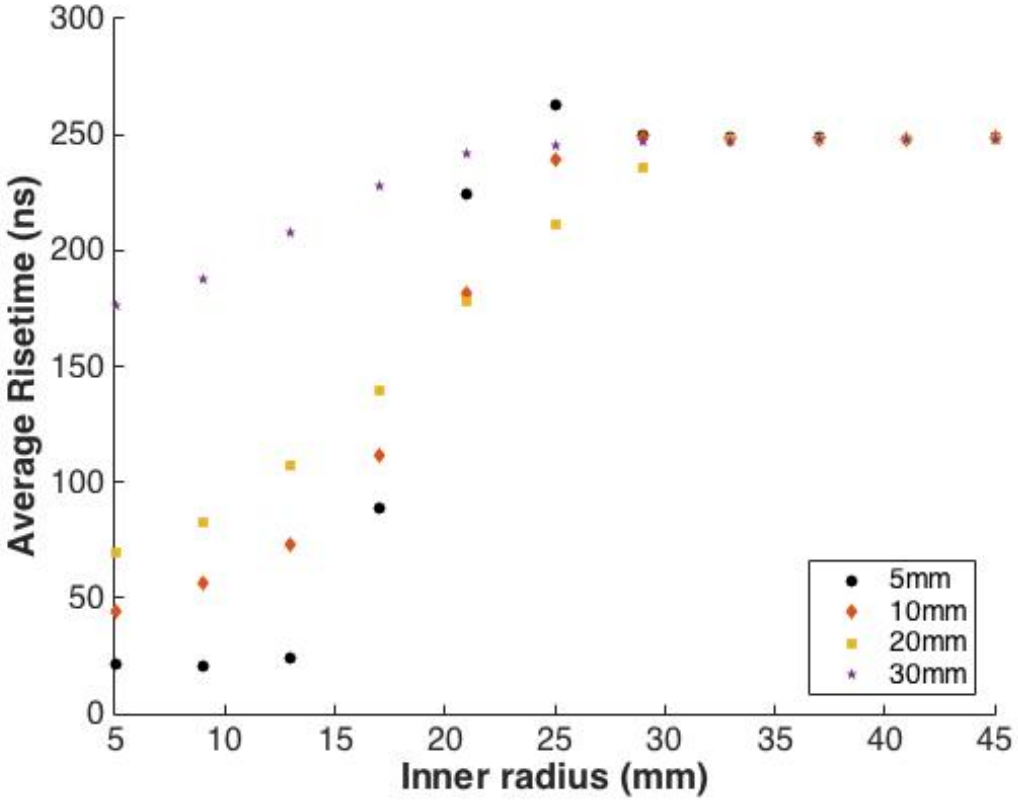

(b)

Figure 5.2: Calculations of average risetime to show the dependence on the (r,z) position of the interaction where the risetimes used are (a) T10 and (b) T30.

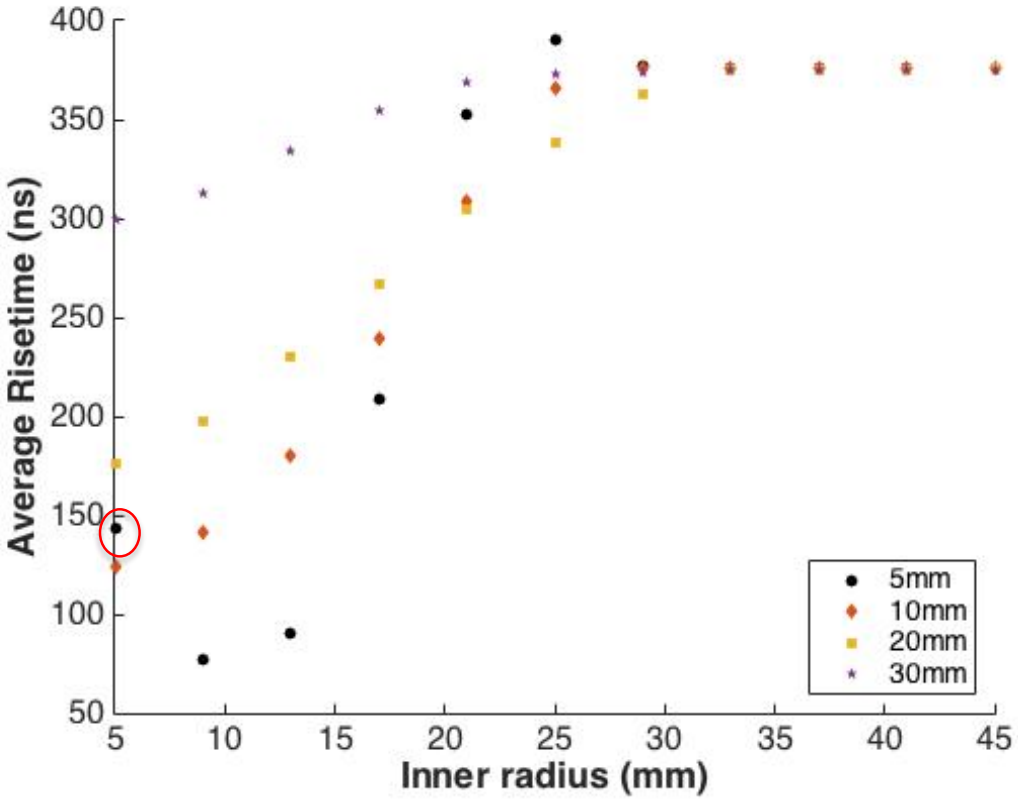

Figure 5.3: Calculations of average risetime to show the dependence on the (r,z) position of the interaction where the risetimes used is T90, the anomalous point circled in red is due to the different path lengths for electrons in comparison to holes in this region.

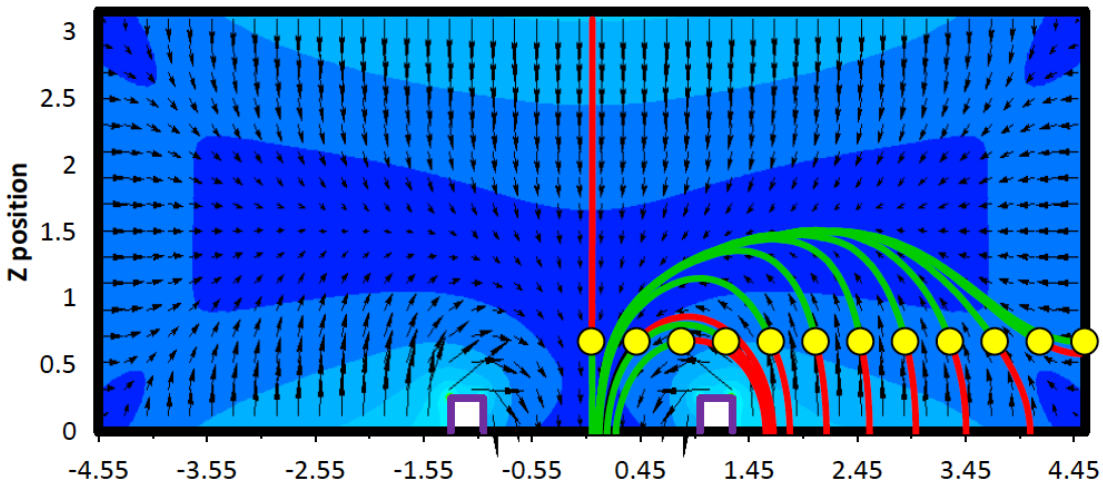

Figure 5.4: Simulated trajectories of holes and electrons for γ -ray signals showing longer path lengths for electrons about the centre of the crystal. Figure used with permission from [54].

wide annuli in a plane at 20.5 mm above the point contact, this plane is chosen because it represents a slice through the crystal encompassing both the surface and bulk regions of the detector. In the 3 plots in Figure 5.5, the average risetime increases as a function of radius until a maximum is reached at $r \simeq 25$ mm, after which it plateaus. The shape of the plot can therefore be divided into two zones, zone 1 is 0 <r <25 mm and zone 2 is r > 25 mm. From our previous discussions in Section 3.1.1, we know that for 60 keV gamma rays from ^{241}Am, the surface region should extend to a depth of ∼2.1 mm from the outer electrode, and we also denoted the remainder of the crystal as the bulk region. The boundary between zone 1 and zone 2 can be set at 25 mm, the radius at which the gradient of the weighting potential plateaus. However, in this figure it can be seen that risetimes do not change between 25 mm and the edge of the crystal, therefore there isn't a unique risetime for the surface zone ($r >$ 43 mm). This can be attributed to the shallow gradient of the weighting potential that exists in zone 2. Within zone 1, the gradient of the weighting potential is steeper, this has the impact of increasing the acceleration of the charge carriers from their point of origin to the collecting electrode. The DCSA algorithm works by operating a threshold on the risetime at the boundary of zones 1 and 2. For this reason, we make the following assumptions:

- The signals produced in the region marked as zone 1 and shaded green are correctly identified as bulk signals.
- For zone 2, the signals *may* be incorrectly interpreted as surface rather than bulk signals (red).
- For radii greater than (43 $\pm$1) mm the surface signals are correctly identified (green).

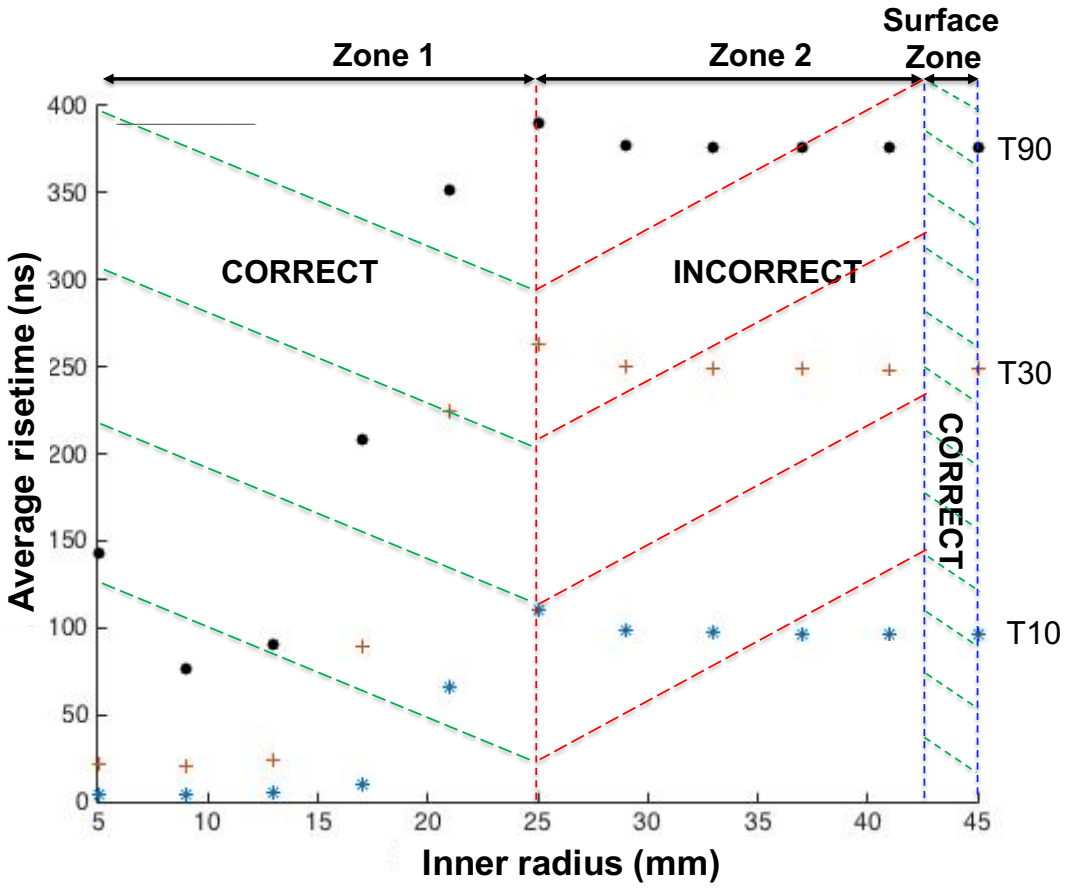

Figure 5.5: Average simulated risetime calculated for the same plane used in Figure 5.6. The extent of the surface region together with zones 1 and 2 are indicated.

Whilst efficient, using an average risetime has some limitations. The crystallographic axes of germanium have a bearing on the risetimes throughout the crystal as there are lower values along the $\langle 100 \rangle$ axis, as shown in the RM. This leads to the incorrect identification of some of the signals as surface signals in zone 2. In addition to the effects of the crystallographic axes, the discrepancy in the correct and incorrect identification of signals is also as a result of the shallow gradient found in the weighting field that has been discussed

earlier Figure 4.4. Indeed, if one examines the gradient of the weighting potential shown in this figure, it is apparent that it has a region from the centre to a radius of ∼25 mm in which the gradient decreases significantly, for radii greater than ∼25 mm, the gradient undergoes little change. As such, the drift velocities of the charge carriers and, thus the risetimes for signals originating in this outer region will change little. This is reflected in the plateau section of the plots in the surface region to the right of the red dashed line in Figure 5.5. The results shown this figure indicate that the thresholds to be used with $T(RT)$ = 10, 30 and 90 correspond to 95, 245 and 365 ns, respectively, and are listed in Table 5.1. When the DCSA algorithm is applied, all signals with a risetime less than the threshold will be removed from the energy spectrum. This acts to remove bulk interaction events at low radii. One of the goals of optimising the DCSA will be to minimise the width of the incorrect region as much as possible.

Risetime	Threshold (ns)
T10	95
T30	245
T90	365

Table 5.1: Risetime thresholds used when applying the DCSA for T10, T30 and T90 in the 20 mm plane

To further illustrate the dependence of risetime on (r, z), RM have been calculated for z = 20.5 and 29.5 mm, these represent the bulk (at smaller radii) and surface regions respectively. The RM for these calculations are shown in Appendix B. In these examples, the risetime calculations have been generated for $T(RT)$ = 10, 30 and 90. These calculations reveal that, as in previous results, the risetimes calculated for T10, T30 and T90 in the centre of each detector plane are lower than in the outer regions of the plane. They also replicate the previous results indicating a region with radii $<$ 25 mm in which there is a sharp change in risetime surrounded by an outer region at radii $>$ 25 mm in which there is little change, other than the differences found in the crystallographic axes. In the surface region, at z = 29.5 mm, the range for T10 is between 80 ns in the centre

to 105 ns at the edge of the plane, for T30 the corresponding range is between 170 and 260 ns and for T90 between 290 and 385 ns. In the bulk region, at $z = 20.5$ mm, the range for T10 is between 50 ns at the centre, rising to 90 ns in a ring about the central region before rising further to 100 ns at the edge. For T30, the corresponding risetimes are 100 ns in the centre rising to 240 ns in a ring around the central region and rising further to 260 ns at the edge. For T90 the range is from 220 ns in the centre, rising to 360 ns in a ring around the central region then rising to a maximum of 380 ns at the edge. This variation is to be expected as the distance to the electrode, and hence the path length of the charge carriers increases with both radius and distance above the point contact. It can also be observed that angular variations in risetime as a result of the effects of the crystallographic axes are again evident with longer risetimes along the $\langle 110 \rangle$ axis and shorter risetimes along the $\langle 100 \rangle$ axis. These variations range from 10 ns for T10 and 20 ns for T30 and T90. Whilst these results show that risetime is a function of (r, θ), they do not necessarily help in establishing the optimum $T(RT)$ to use with the DCSA, this will now be investigated.

5.2 DCSA Algorithm Methodology

In order to develop the DCSA algorithm, the knowledge of position dependence and the threshold values from Figure 5.5 have been used as its foundation using t10, t30 and t90. This section will now outline the methodology in developing the DCSA to establish the optimum $t(RT)$ and threshold to be used.

5.2.1 DCSA Event Selection

It has been shown that signals within the detector have position sensitivity and that discriminating between surface and bulk signals based on their risetime is to some degree possible. The DCSA has been developed using the previous thresholds for risetime

calculations. We shall now consider the results using a range of $T(RT)$ in these planes to establish the optimum to be used in the implementation of the DCSA for the subsequent analysis of experimental data.

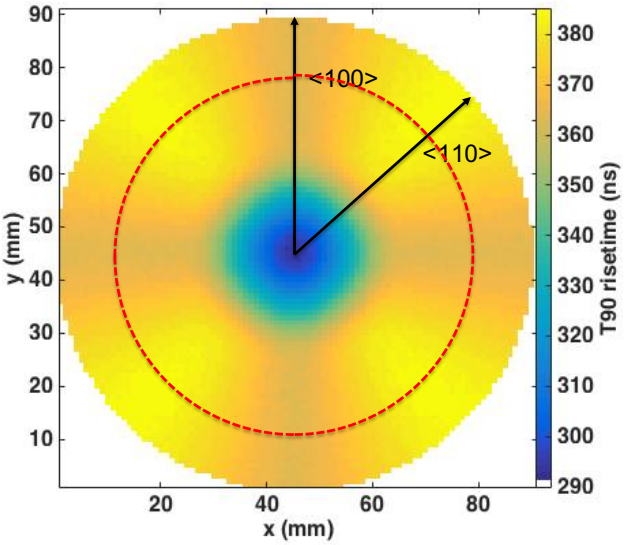

Figure 5.6: Risetime map for T90 at $z = 29.5$ mm above the base of the detector, the $\langle 100 \rangle$ and $\langle 110 \rangle$ crystallographic axes are indicated together with $r = 25$ mm. The centre of the plane is at (45,45) whilst the axes limits represent the diameter of the crystal.

Figure 5.6 shows the RM for T90 at a height of 20.5 mm above the base of the detector corresponding to the surface region. The risetime is a minimum at the centre of the image, corresponding to signals generated directly above the point contact. At larger radii, the charge generated from these positions takes longer to drift towards the point contact, resulting in a larger T90. Since we are interested in achieving suppression of Compton scattering events in the bulk, we will examine the plane at $z = 20.5$ mm above the point contact. To demonstrate that suppression has taken place, the DCSA has been applied to the ADL data at $z = 20.5$ mm using a 365 ns T90 threshold to the risetime map that was shown in Figure 5.6. The result is presented in Figure 5.7. The white regions in the risetime map represent sites where suppression of the signals has taken place. The coloured areas in the outer 2 mm of the map represent signals that have been correctly

retained in the surface zone (Figure 5.5). It can be seen that a small number of events have been incorrectly suppressed in this zone. The signals that have been incorrectly suppressed in the extended surface region correlate to the ⟨100⟩ crystallographic axis, an area in which we would expect shorter risetimes than in the ⟨110⟩ axis. By examining this figure we can see that the general distribution of risetimes follows the same trends as before, with longer risetimes along the ⟨110⟩ axis than the ⟨100⟩ axis. For completeness, the effects of altering the thresholds for T10, T30 and T90 risetimes used in the DCSA were investigated, these results are given in Appendix B.

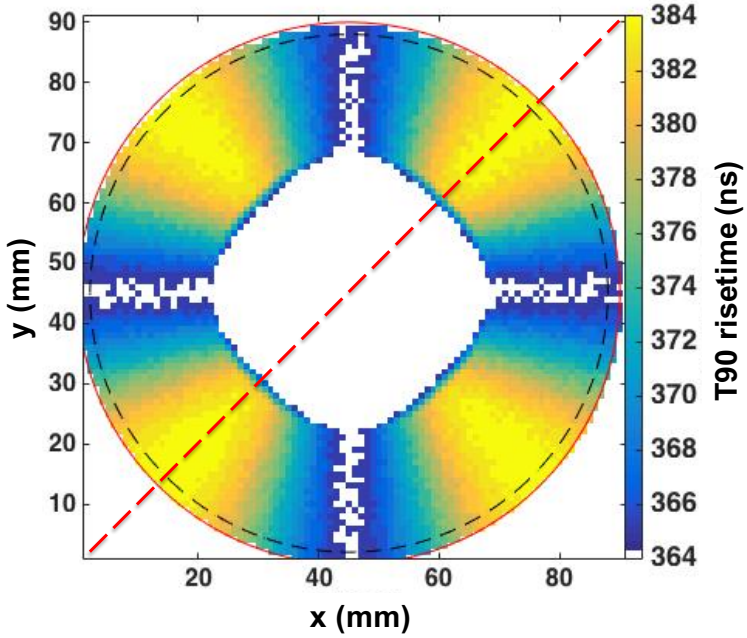

(a)

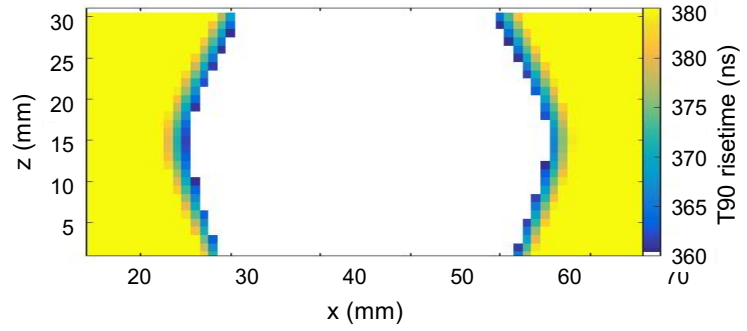

(b)

Figure 5.7: Simulated risetime map for $T(RT)$ = T90 in (a) an (x, y) plane at $z = 20.5$ mm above the contact and (b) an (x, z) plane along the red dashed line in (a), both plots are with the DCSA applied and using a threshold of 365 ns. The extent of the surface zone is shown by the black dotted line in (a). The centre of the plane is at (45,45).

So far we have looked at results that consider the (x, y) plane at various distances above the contact. However, this does not provide a complete treatment for the entire detector volume. To complement these results we will now consider an (x, z) plane through the centre of the detector crystal along the red dashed line in Figure 5.7a. Figure 5.7b is a RM for such a plane and is along a $\langle 110 \rangle$ axis at $x = y$, in this figure the DCSA has been applied using T90 and a thresholds 365 ns. As before, the white area in this figure

represents the "suppressed" region in the plane. The suppressed area is not uniform in width, it extends to a width of ∼50 mm at $z = 15$ mm, narrowing to 30 mm at both the base and top of the crystal. This variation is as a consequence of the weighting fields, as shown in the ADL model which models the surface region into a elliptical shape, following the pattern of the weighting fields shown in Figure 4.4a. A similar pattern is observed along the ⟨100⟩ axis but a lower threshold is used due to the shorter risetimes along this axis.

5.2.2 Experimental Optimisation of DCSA

Since the aim of this work is to develop a DCSA for use with a single BEGe detector, such as those outlined in Section 2.1, an experiment was carried out using the BEGe6530. The experiment was conducted at the University of Liverpool and used the BEGe6530 with a combination of unshielded and uncollimated point sources. The sources, which were chosen to simulate the requirements outlined in Chapter 2, were ^{241}Am and ^{137}Cs point sources. The experimental data was acquired using the BE6530 BEGe detector, the preamplifier signals were digitised by a Caen V1724 with a 100 MHz sample rate, the radiation point sources, NPRL466 ^{241}Am with an activity of 0.179MBq and NPRL192 ^{137}Cs with an activity of 0.171 MBq, were placed centrally in front the BE6530 detector. A diagram of the equipment used is shown in Figure 5.8. This shows the BEGe placed on the workbench with a scissor stand located in front of and in line with then centre of the crystal. The source was placed on the edge of the stand at a distance of 25 cm from the front detector face. Data sets with a counting time of 10 minutes were obtained using the two sources both individually and in combination with each other. The acquisition was controlled using MIDAS [51].

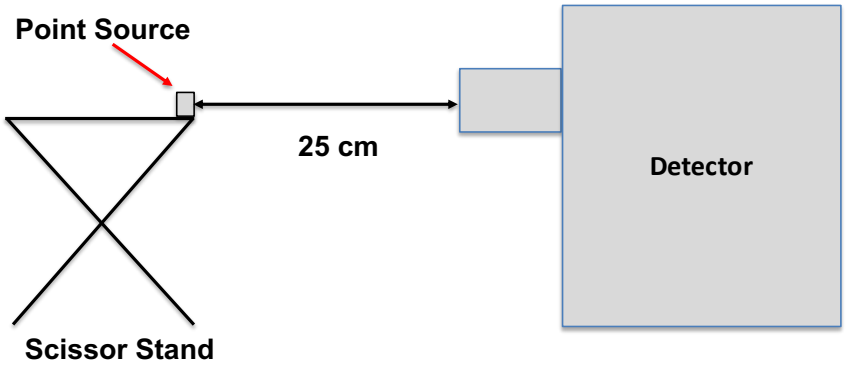

Figure 5.8: Schematic of experimental set-up used to obtain data from a point source. Note that no collimantion was used.

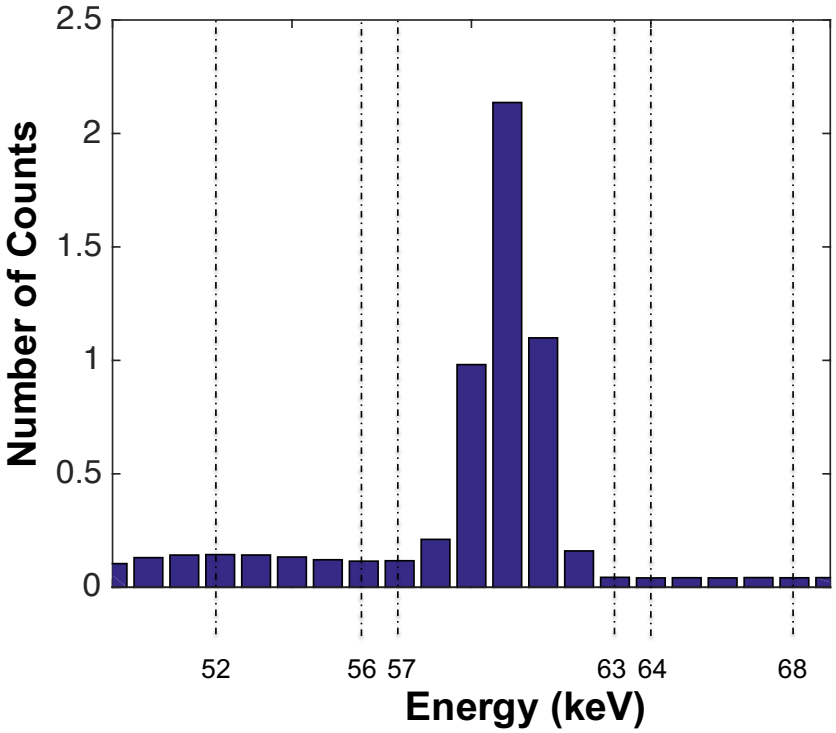

Figure 5.9: An example of energy bins used for calculating net counts and range for the ^{241}Am full energy peak.

Using this experimental data, a comparison was made between the raw spectrum and the spectrum produced with the DCSA applied with a threshold of 365 ns on the $T(RT) = 90$. As we are interested in the suppression of Compton scattering events without a reduction in the counts in the ^{241}Am full energy peak, the number of counts in two energy ranges were determined. One encompassing the ^{241}Am full energy peak and the other spanning the Compton continuum, which is a result of scattering events from the

^{137}Cs full energy peak. Figure 5.9 shows a sample spectrum from the experimental data in the region of the ^{241}Am peak after the DCSA has been applied. This figure shows the bins used to calculate the number of gross counts in the peak by using the bins for the peak together with a range of energy bins that includes the background region close to the peak, in this example the bins used have an energy range from 52 to 68 keV. The effect of altering the threshold can be observed by considering the change in these values for both spectra, the variation can be calculated as a function of the threshold used. Figure 5.10 shows the results for T30, using thresholds from 210 to 390 ns. We can see that at thresholds above 250 ns, the plots tend to converge. Below 250 ns the plots diverge to a maximum differential at 220 ns before converging again below 210 ns. The optimum threshold for T30 will be in the range of 210 $<$ threshold $<$ 250 ns and that outside of this range, the effects of the DCSA reduce. Since the purpose of the DCSA is to suppress Compton scattering events whilst retaining surface signals from ^{241}Am, the optimum threshold will be found at the point at which the maximum divergence between the ^{241} Am peak and Compton continuum range occurs, for T30 this arises at a threshold of 220 ns.

The same method was applied to a range of $T(RT)$ between T70 and T95, with the results reproduced in Table 5.2. The associated plots are shown for completeness in Appendix B. Using these calculations it was established that the $T(RT)$ that resulted in the threshold with the greatest divergence was found to be $T(RT)$ = T76, at a threshold of 300 ns, with a divergence of 11.5% and a standard deviation of 0.2% (Figure 5.11). For clarity, the difference calculated by subtracting the value in the ^{241}Am peak from the corresponding Compton continuum range value is included. This figure shows a maximum at a threshold of 300 ns. To explore this further, we can consider the number of counts retained in the ^{241}Am full energy peak compared to the number of counts suppressed in the ^{137}Cs peak which is shown for T76 in Figure 5.12. Here we see that by varying the threshold, it is possible to retain up to 98% of the ^{241}Am peak whilst suppressing 10% in the ^{137}Cs peak. With increasing threshold, these converge at a threshold of 360 ns.

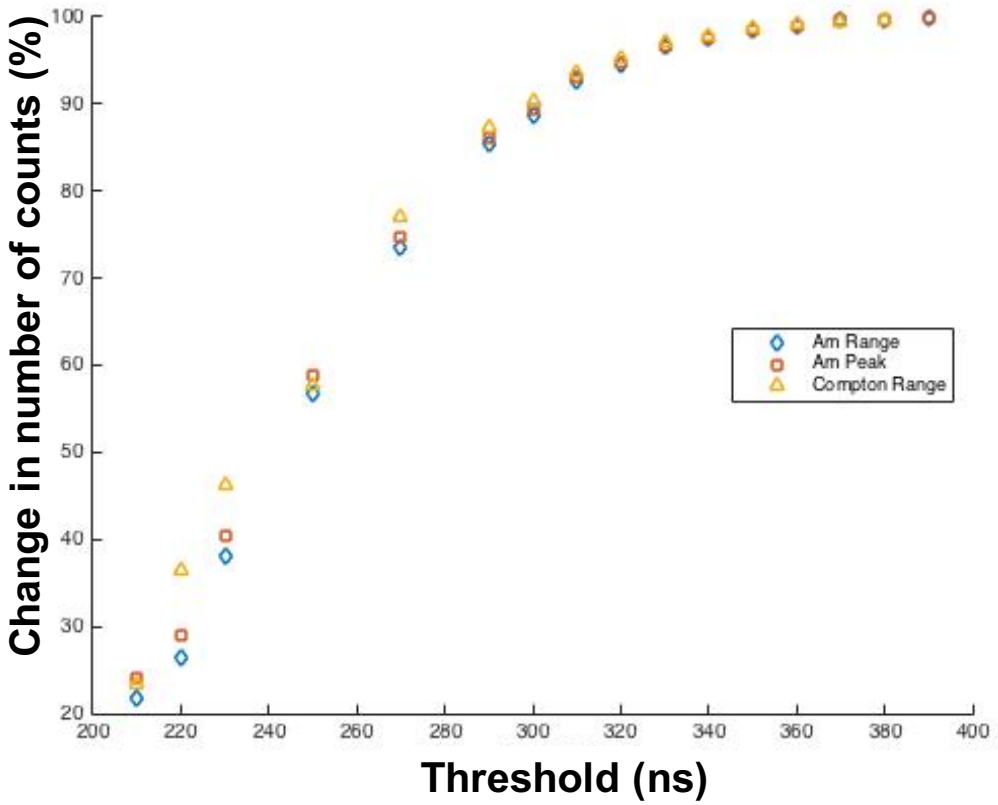

Figure 5.10: Comparison between the % change in the number of counts in (a) the energy bins surrounding the ^{241}Am peak, (b) the ^{241}Am peak and (c) the Compton continuum when the DCSA has been applied for a range of thresholds for $T(RT)$ = T30.

Henceforth a threshold of 300 ns will be used for the DCSA, at this value a retention rate of 95% with a suppression of 17% is achieved.

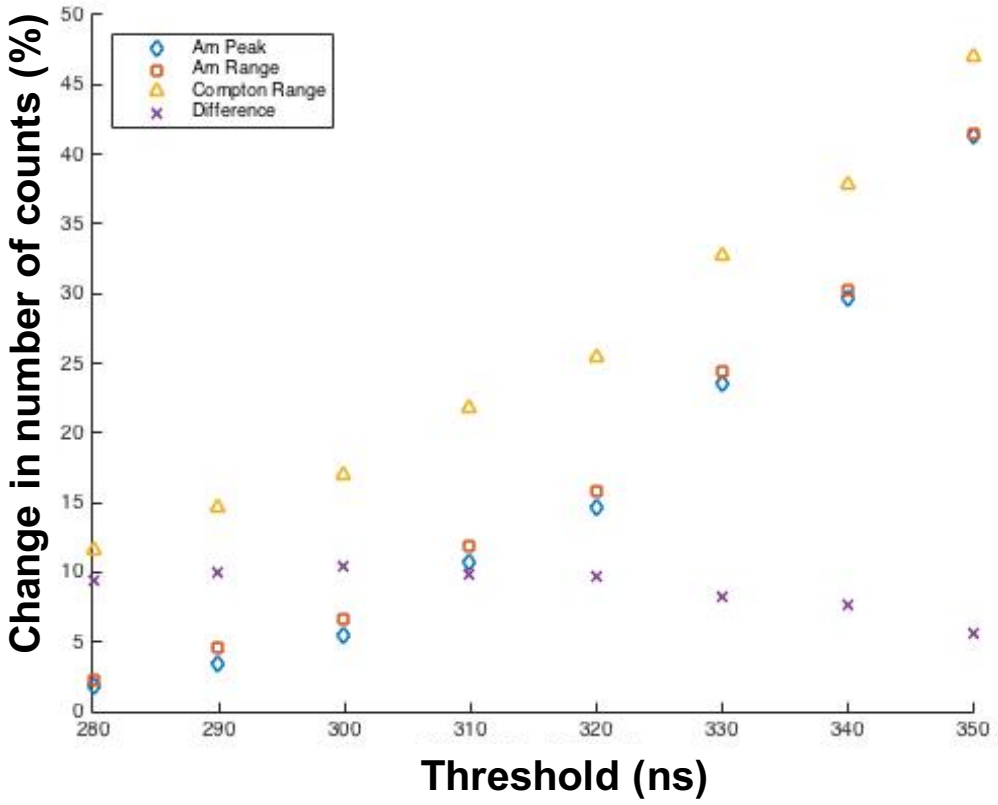

Figure 5.11: Comparison between the % change in the number of counts in (a) the energy bins surrounding the ^{241}Am peak, (b) the ^{241}Am range and (c) the Compton continuum when the DCSA has been applied for a range of thresholds for $T(RT)$ = T76.

$T(RT)$	Threshold (ns)	Difference (%)	σ (%)
T30	245	10.1	0.6
T70	297	10.5	0.4
T74	300	10.3	0.3
T75	300	10.5	0.3
T76	300	11.5	0.2
T77	300	10.3	0.3
T80	340	10.8	0.4
T85	340	10.8	0.4
T90	365	10.5	0.4
T95	365	10.0	0.3

Table 5.2: Optimum thresholds used for a range of $T(RT)$ showing the associated maximum difference in the % change of the ^{241}Am peak and the range of the Compton peak.

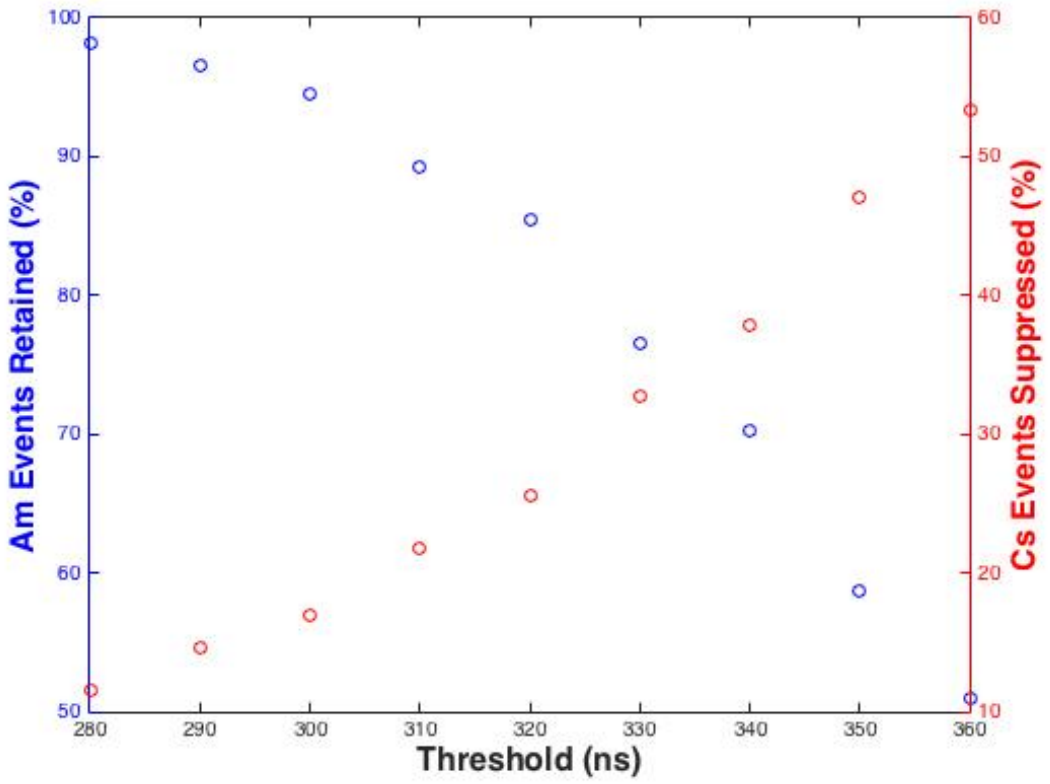

Figure 5.12: Number of counts retained and suppressed in the ^{241}Am peak and in the ^{137}Cs peak after the DCSA has been applied using $T(RT)$ = T76.

The ADL database has been used to investigate why T76 and a threshold of 300 ns is optimum. By looking at an (x, z) plane, the effects of the DCSA throughout the depth of the detector can be established. Figure 5.13 are RM in (x, z) plane along a $\langle 100 \rangle$ axis at $y = 0$ for $T(RT)$ =T76 and with the DCSA applied with a range of thresholds from 240 to 340 ns. As before, the white ares represent the suppressed regions. These plots corroborate the results from Figure 5.5, that is, at $z \lesssim 15$ mm and radii $\lesssim 25$ mm the suppression has been correctly calculated. For radii between 25 and (43 $\pm$ 1) mm there are still signals that have not been correctly suppressed. The situation at $z \gtrsim 15$ mm becomes slightly more complicated. At each increment in z, the radial range in which the signals have been correctly suppressed diminishes. If we consider the weighting field that we saw in the previous chapter, the diminishing region is in line with changes in the weighting field and its shallower gradient at $z \gtrsim 15$ mm. The radii at which the correct

results are achieved also reduces up to $z \simeq 27$ mm, above this no suppression takes place. We anticipated that the surface region, as calculated in Section 3.1.1, would extend to a depth of $(z = 29.4 \pm 1)$ mm, this indicates that there is region between $z \simeq 27$ and $z \simeq (29.4 \pm 1)$ mm where the suppression may not be correctly applied. However, we should also consider that the figure of 2.1 mm is the depth at which 90% of the intensity of the beam has been attenuated, the remaining 10% may penetrate to greater depths which may account for some of the discrepancy in the results between $z \simeq 27$ and (29.4 ± 1) mm. With thresholds higher than 300 ns the extent of the suppressed events encroaches into the true surface region, these thresholds would be unsuitable for use with the DCSA as more ^{241}Am events would be suppressed and this is not desirable. At thresholds less than 300 ns fewer events would be correctly suppressed, again, an undesirable outcome.

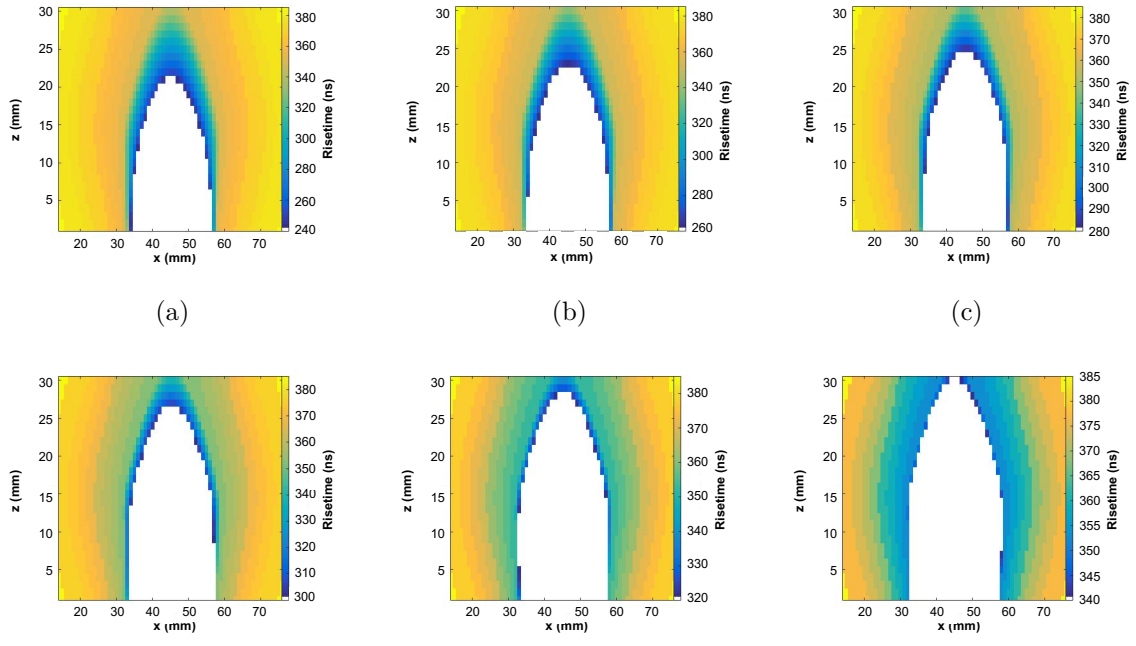

Figure 5.13: T76 RM for the (x, z) plane along the $\langle 100 \rangle$ axis with the DCSA applied and thresholds of (a) 240, (b) 260, (c) 280, (d) 300, (e) 320 ns and (f) 340 ns.

The (x, z) plane shown in Figure 5.13 illustrates that using T76 with a threshold of 300 ns in the application of the DCSA provides the largest suppression region without encroaching into the surface region at $z \gtrsim 43$ mm (Figure 5.13d).

5.3 Minimum Detectable Activity

Having established that T76 is the optimum $T(RT)$ to be used with the DCSA, calculations were made to ascertain whether an improvement in the Minimum Detectable Activity (MDA) can be achieved using the DCSA. The MDA can be calculated using the Currie formulation [55, 56]:

$$MDA = \frac{k_\alpha^2 + 2k_\alpha\sqrt{B(1+\frac{n}{2m})}}{P_\gamma \epsilon_{abs} t} Bq, \tag{5.1}$$

where

$$B = \frac{n}{2m}\left\{\sum_{i=L-m_l}^{L-1} C_i + \sum_{j=L+m_u}^{U+1} C_j\right\} counts,$$

L and U are the lower and upper limits of the peak, $m = m_l = m_u$ are the number of channels before and after the peak, n is the number of channels in the peak, k_α is the confidence level with a value of 2σ (95%), P_γ is the probability of emission [57], ϵ_{abs} is the absolute efficiency of the detector and t is the counting time [58] (in this case 10 minutes). An illustration of the channels used in the Currie formulation are shown in Figure 5.14.

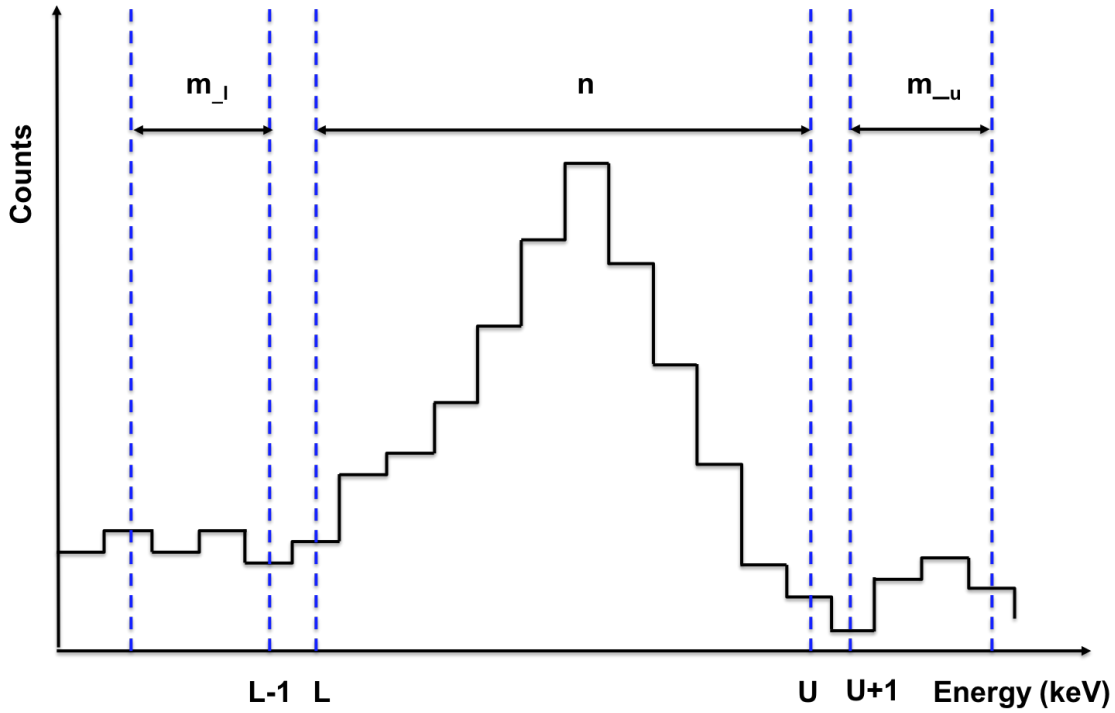

Figure 5.14: Illustration of channels used for MDA calculations

Since we are predominantly interested in the information for the energies below 100 keV in the spectrum, calculations for the MDA in the region of the ^{241}Am peak of the experimental data used in the previous section were made using the bins shown in Figure 5.9. The MDA calculated for the 60 keV full energy peak without the DCSA algorithm applied was (0.46 ± 0.02) Bq. The DCSA algorithm was then applied using various combinations of T(RT) and thresholds, the results of which are shown in Table 5.3. The greatest improvement in MDA, and therefore the optimum use of $T(RT)$, is obtained when using T76 in combination with T90 and thresholds of 300 and 365 ns respectively, this combination gives an MDA of (0.29 ± 0.02) Bq. The improvement in the MDA is calculated using:

$$Improvement = \left(\frac{A}{B} - 1\right) * 100\% \tag{5.2}$$

where A and B are the MDA values without and with the DCSA applied respectively. This gives an improvement of $(58 \pm 5)\%$ for this particular experiment

$T(RT)$	Threshold (ns)	MDA (Bq)	Error (Bq)
30	245	0.33	0.02
70	297	0.32	0.03
76	300	0.31	0.02
80	340	0.32	0.03
90	365	0.33	0.03
76/90	300/365	0.29	0.02

Table 5.3: Improvements in MDA calculated for the 60 keV full energy peak from ^{241}Am for a range of $T(RT)$ from experimental data using ^{241}Am and ^{137}Cs point sources.

Figure 5.15 shows the risetime map for the DCSA with the combined $T(RT)$ = T76 and a threshold of 300 ns. It can be seen that effects of the crystallographic axis are mitigated in zone 2 and the surface zone. It is also apparent that the DCSA has correctly suppressed signals arising from positions up to $r \simeq 25$ mm (within zone 1 and shown in white in the figure), whilst all events in the surface zone have been retained. Some events in zone 2 have not been suppressed. This is expected because there is little variation in risetimes in this region.

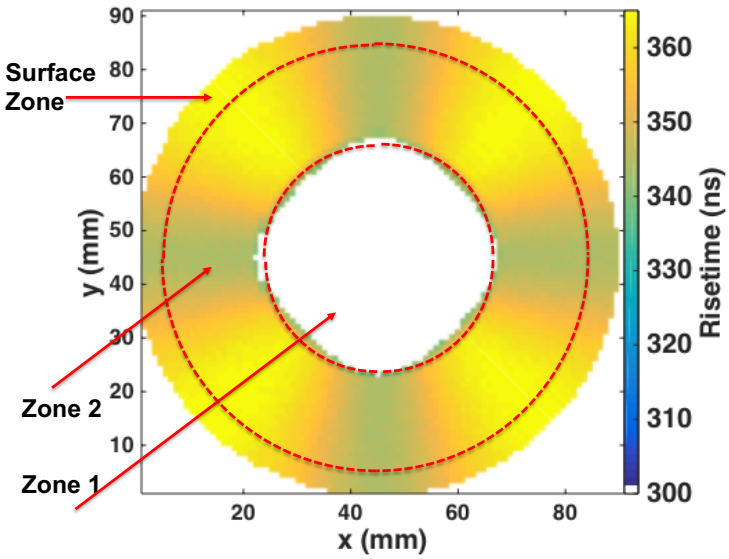

Figure 5.15: Risetime map using T76 in combination with T90 and thresholds of 300 and 365 ns respectively and calculated for theoretical (ADL) signals in a plane at 20.5 mm above the point contact with the DCSA applied. The centre of the plane is at (45,45) and the boundaries for zone 1 and zone 2 are indicated .

5.4 Summary

The DCSA has been developed with the aid of a theoretical charge signal database. It has been shown that risetime is dependent on (r, z) and this has been used as the basis for developing the DCSA that is the goal of this thesis work. By using the DCSA with a BE6530 detector, an improvement in the MDA of $(58 \pm 5)\%$ for a peak at an energy of 60 keV has been achieved. However, it has also been established that, due to the size of the BE6530, the gradient of the weighting potential in zone 2 and the surface zone is shallow, which results in little variation in risetimes at radii > 25 mm. This has led to a difficulty in discriminating between surface and bulk signals in zone 2. In the following chapter we will utilise the DCSA with these optimum values and examine data that had been obtained experimentally from the National Nuclear Laboratory for our test scenarios.

Chapter 6

Industrial Test Scenario

In the previous chapters we have discussed the use of ADL to create a database of pulse shapes and then use this database to examine the position dependency of the interaction point. From this, a DCS algorithm was developed and tested using data produced using ADL. An improvement of $(58 \pm 5)\%$ in the MDA was obtained. We shall now apply the DCS to data that has been obtained experimentally and verify whether the same improvements are observed in an industrial context using LLW.

6.1 Experimental Results

To test the algorithm in a realistic scenario, experiments were conducted at the National Nuclear Laboratory Central Laboratory, Sellafield, UK. The experimental setup comprised of a variety of sources placed in front of the BE6530 detector. In each of the experiments, the data was read out from the BE6530 using a Caen DT5780 Dual Digital Multi-channel Analyser with a trace length of 1024 samples, a 10ns sample size, a 100 MHz sample rate and a trapezium risetime of 550 ns. The sources used were chosen to simulate the requirements outlined in Chapter 2, whereby a mixed isotope waste sample comprises of low energy gamma emitters in the presence of high energy gamma emitters. Figure 6.1 is

a photograph depicting an example of the experimental setup with a source mounted on a retort stand in front of the detector with a schematic of the experiment below.

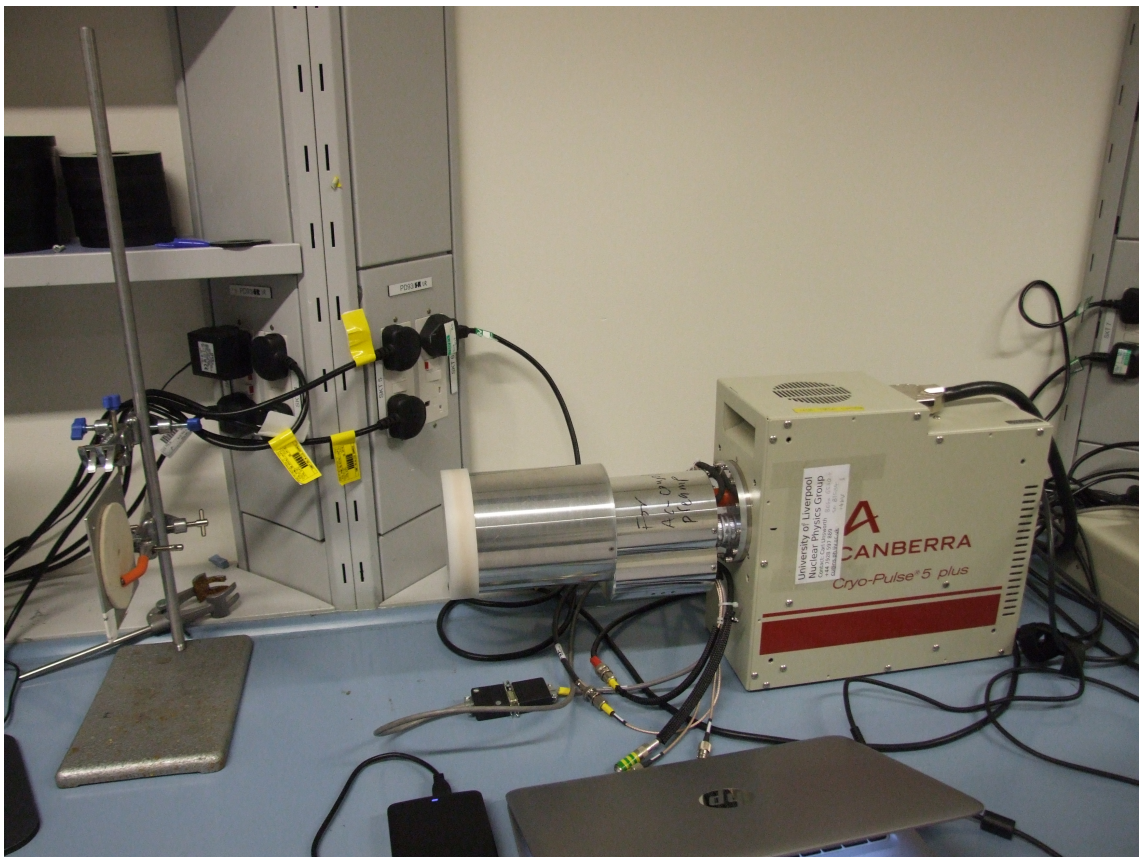

(a)

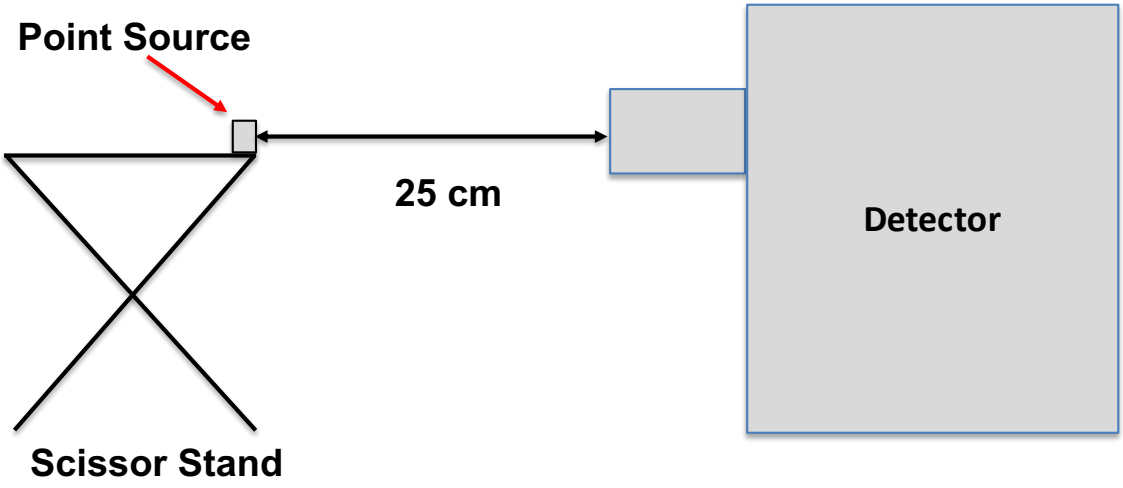

(b)

Figure 6.1: (a) Photograph of the experimental set-up used to obtain data. In this example, a point source has been mounted on a retort stand in front of the BE6530 detector, (b) A schematic of the experimental setup.

For the first experiment, a calibration spectrum was taken using a 88 kBq ^{152}Eu source in a 2% HNO_3 solution which was contained in a 16 x 50 mm vial within a 26 x 51

mm Securitainer®, the experimental setup is shown in Figure 6.3. The source was placed in a holder mounted on a retort stand which was placed in front of the BE6530 and at a distance of 29 cm, the calibration spectrum is displayed in Figure 6.2.

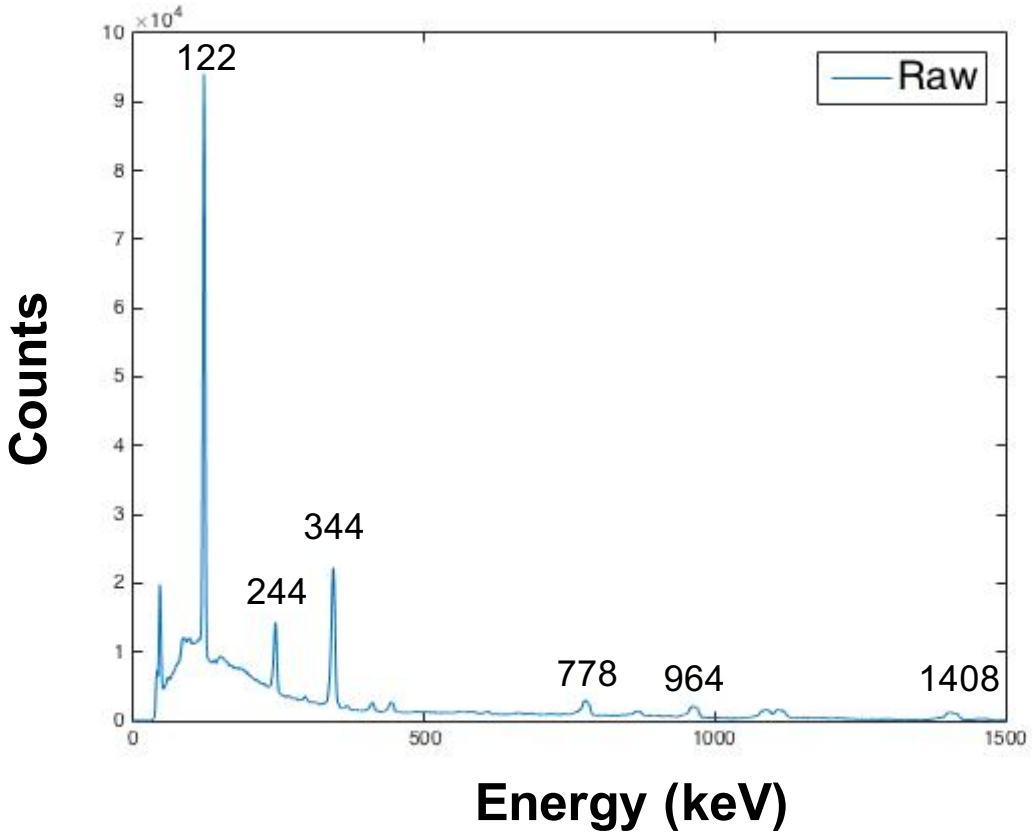

Figure 6.2: Gamma ray calibration spectrum using a ^{152}Eu sealed source. Some of the energies of the key full energy peaks used for the calibration are indicated.

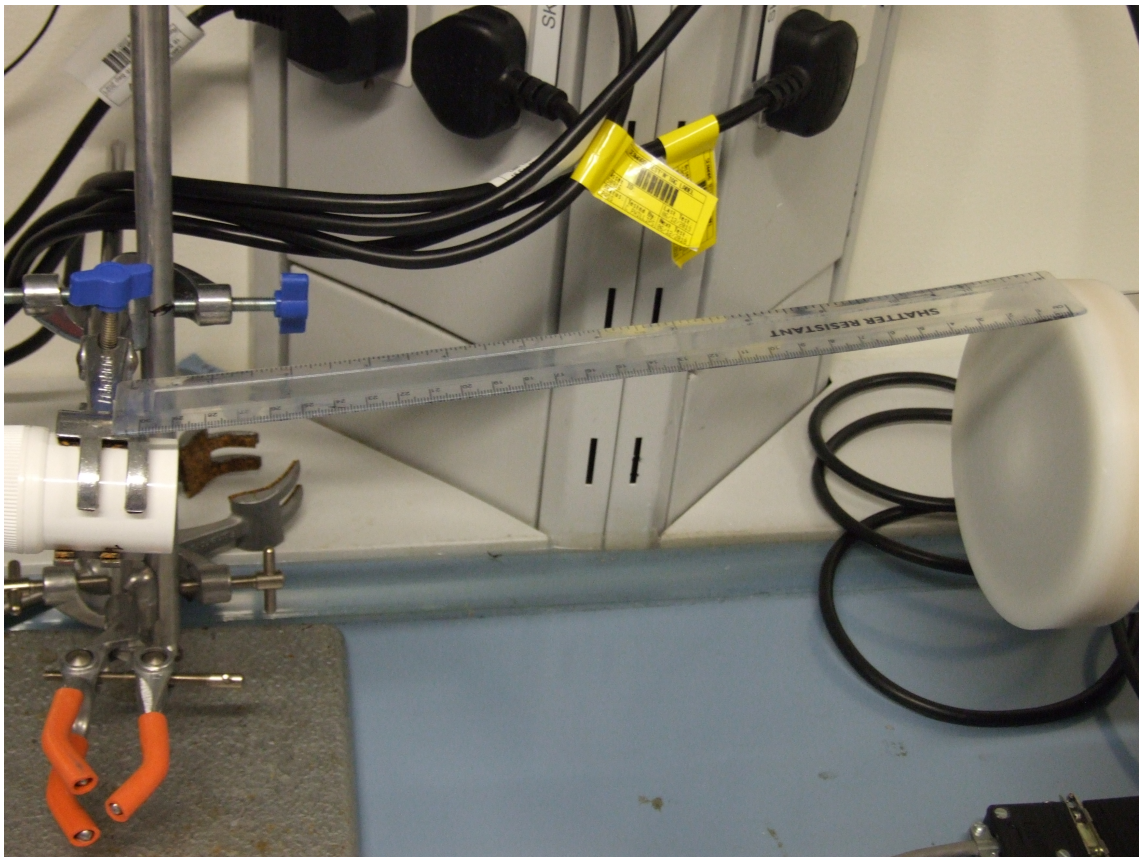

Figure 6.3: Photograph of experimental set-up showing a source contained within a Securitainer® retained on a retort stand in front of the BE6530 detector.

The second experiment was conducted using a bag of mixed waste with a variety of isotopes and a nominal activity for β/γ, recorded by the Health Physics Department at NNL, of 15 μSv/hr, the experimental setup is shown in Figure 6.4. This bag is typical of LLW bags that are sent for disposal at the LLWR by NNL and contained a variety of waste items from an NNL laboratory. To carry out the experiment, the waste bag was placed in front of the BE6530 detector with the exterior of the bag at a distance of 55 cm from the BE6530 front face. This distance was chosen due to the higher activity of the waste bag than for the sources used in previous experiments. Data was recorded for 20 minutes using the same parameters as before and the spectrum for energies between 0 and 1500 keV obtained using this setup is shown in Figure 6.5. However, to understand more fully what is taking place as a consequence of the DCSA being applied and since we are interested in the effect of the DCSA at low energies, Figure 6.6 shows the same data with

the spectrum constrained to energies below 300 keV. It can be seen that the suppression of Compton scattering events in the region of the ^{241}Am peak is evident, the number of counts in the background in this region has reduced from 3500 to 2400 with the DCSA applied. Figure 6.5 demonstrates that the waste bag that was used for this experiment contained a mixture of isotopes and that is evident that a high relative abundance of ^{137}Cs and ^{60}Co was present. The MDA for this spectrum was calculated as (0.41 ± 0.03) Bq. Again, a combination of T76 in conjunction with T90 and thresholds of 300 and 365 ns respectively have been applied. The MDA with the DCSA in operation was calculated as (0.29 ± 0.03) Bq, this gives an improvement of $(41 \pm 5)\%$ in the MDA using equation (5.2). The difference in the MDA improvements achieved for this experiment and the experiment carried out in Section 5.2.2 is attributable to the variations in the geometries of the two experiments, primarily as a result of the greater distance used for the this experiment. However, the two results are consistent with each other using the consistency check given in equation (4.5).

Figure 6.4: Photograph of the experimental set-up used to obtain data for experiment 3. In this example, a LLW waste bag from an NNL laboratory is placed 55 cm in front of the BE6530 detector.

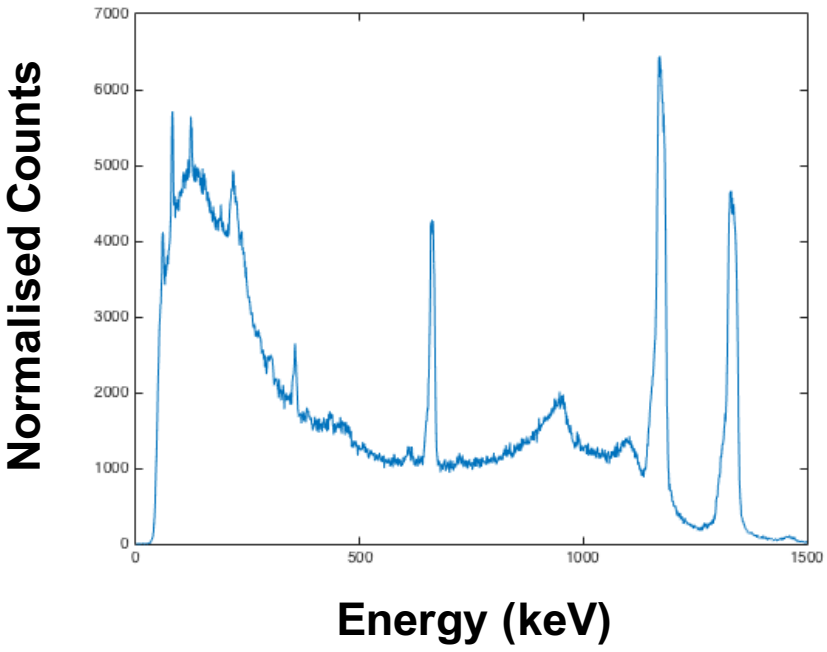

Figure 6.5: Gamma ray spectrum for the raw data of a mixed isotope NNL LLW bag.

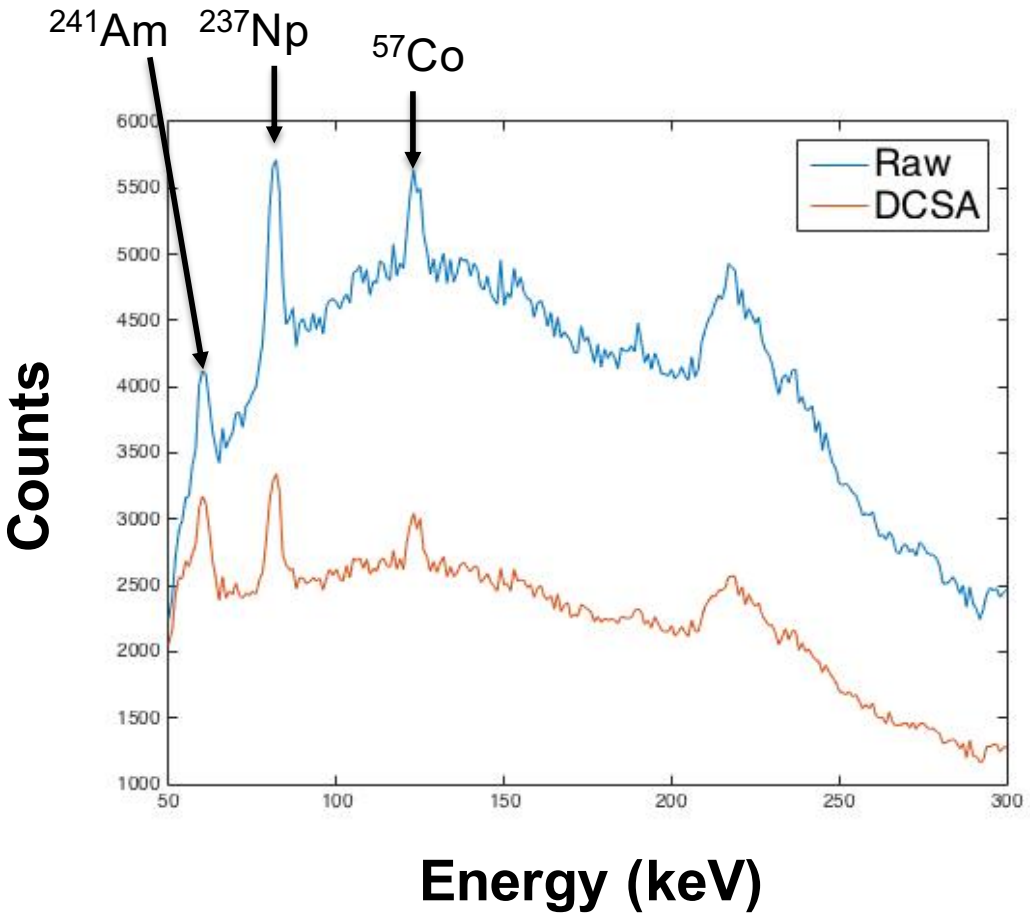

Figure 6.6: Gamma ray spectrum for both raw data and with the DCSA applied to a mixed isotope NNL LLW bag constrained to energies below 300 keV. A combination of T76 and T90 with thresholds of 300 and 365 ns have been used when applying the DCSA.

Chapter 7

Conclusion & Recommendation

The feasibility of using a Digital Compton Suppression Algorithm (DCSA) in gamma-ray spectroscopy using a single Broad Energy Germanium (BEGe) detector has been examined as an alternative to multi-detector Compton suppression systems. The DCSA algorithm relies on a knowledge of the position dependent response of the BEGe detector. This has been studied for a BEGe BE6530 detector using the ADL toolkit. Application of a veto for events that arise in the bulk of the detector will preferentially remove higher energy events that can penetrate throughout the germanium crystal.

ADL has been used to generate a theoretical database of signals for the entire detector volume. The database was used to simulate risetimes for signals and to develop a Digital Compton Suppression Algorithm. The algorithm was used to differentiate between signals originating in the bulk of the detector crystal from those originating in the surface region, both of which are shown in Figure 7.1.

The DCSA was successfully validated against an experimental data set which demonstrated that in future work, ADL could be used to simulate other detectors. It was established that due to the size of the BE6530, the gradient of the weighting potential in zone 2 is shallow and this results in little variation in risetimes at radii

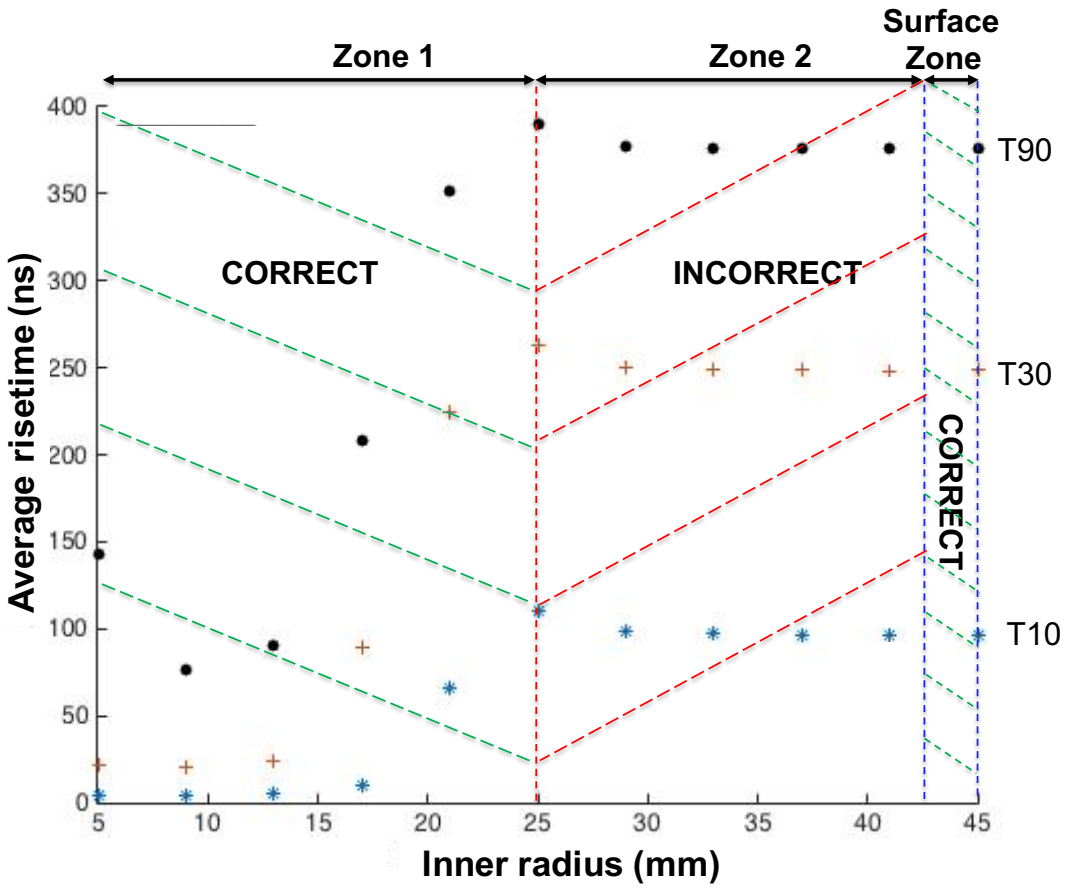

Figure 7.1: Average simulated risetime calculated for the same plane used in Figure 5.6. The extent of the surface region together with zones 1 and 2 are indicated.

greater than 25 mm. This limited the performance of the DCSA in discriminating between surface and bulk signals in zone 2, although the zone 1 events are successfully suppressed. A study was performed to ascertain the risetime thresholds to be applied in order to maximise the suppression of bulk events, whilst at the same time retaining surface events. This was primarily undertaken using the theoretical model and then validated experimentally using ^{241}Am and ^{137}Cs sources at the University of Liverpool. To gauge the performance of the DCSA, the Minimum Detectable Activity for the 60 keV peak from ^{241}Am was calculated. The greatest improvement in MDA was established by finding the optimum risetime, this was found to be T76 in combination with T90 and with thresholds of 300 and 365 ns respectively. Using this combination gave an improvement of $(58 \pm 5)\%$ in the MDA for this particular experiment.

The real world performance of the DCSA was tested by acquiring experimental data

at the National Nuclear Laboratory Central Laboratory, under the guidance of waste characterisation experts. Several experiments were conducted including one using an LLW waste bag containing a variety of waste products contaminated with isotopes such as ^{57}Co, ^{137}Cs and ^{241}Am. The results confirmed the functionality of the DCSA and that an improvement in the MDA of $(41 \pm 5)\%$ for the 60 keV peak from ^{241}Am was achieved.

For future work, further improvements in MDA may be achieved by investigating the use of smaller detector crystals. Smaller detectors will reduce the width of zone 2 as these detectors have weighting potential gradients more typical of zone 1. This will allow for a greater variation in risetime between zone 1 and the surface region with the possibility to retain a higher proportion of the events from interactions in zone 1. The ideal scenario would be to use a detector in which zone 2 is eliminated completely, thereby reducing the number of signals that may be incorrectly identified as surface signals. This will lead to greater improvements in MDA for the 60 keV peak.

This work was supported by The Engineering and Physical Sciences Research Council (EPSRC) [grant number EP/L015390], the Nuclear Decommissioning Authority and National Nuclear Laboratory.

Bibliography

[1] Her Majesty's Governement. *Radioactive Substances Act 1993*. HM Government, Oct. 1993.

[2] Her Majesty's Government. *Environmental Permitting Regulations - Amendments*. HM Government, Department of Energy & Climate Change, Oct. 2011.

[3] P.D. Wilson. *The nuclear fuel cycle from ore to wastes*. 1996.

[4] Nuclear Decommissioning Authority. *UK Radioactive Waste Inventory*. Apr. 2017.

[5] M. Grimston, W.J. Nuttall, and G. Vaughan. "The siting of UK nuclear reactors". In: *Journal of radiological protection : Official Journal of the Society for Radiological Protection* 34 (Apr. 2014), R1–R24.

[6] LLWR. "Service Pricing Schedule, WSC-SPR-LIS – Version 3.10." LLW Repository Ltd.. Apr. 2018.

[7] Ametek Inc. *trans-SPEC-DX-100T*. Ortrec. Oak Ridge, Tennessee, Apr. 2015.

[8] Department of Energy & Climate Change Her Majesty's Government. *UK Strategy for the Management of Solid Low Level Waste from the Nuclear Industry*. HM Government, Feb. 2017.

[9] C. Giel. "Overview of LLW Repository". LLW Repository Ltd. LLWR, Apr. 2015.

[10] B Bruyneel, B Birkenbach, and P Reiter. "Pulse shape analysis and position determination in segmented HPGe detectors: The AGATA detector library". In: *The European Physical Journal A* 52.3 (2016), pp. 1–11.

[11] J. Jernstrom et al. “Non-destructive characterisation of low radioactive particles from Irish Sea sediment by micro X-ray synchrotron radiation techniques: micro X-ray fluorescence (micro-XRF) and micro X-ray absorption near edge structure (micro-XANES) spectroscopy.” In: *Journal of Analytical Atomic Spectrometry.* 19 (2004), pp. 1428–1433.

[12] F Jallu, C Passard, and E Brackx. “Application of active and passive neutron non destructive assay methods to concrete radioactive waste drums”. In: *Nuclear Instruments and Methods in Physics Research Section B: Beam Interactions with Materials and Atoms* 269.18 (2011), pp. 1956–1962.

[13] S. J. Hansen. “Tomographic Gamma-ray Scanning of Uranium and Plutonium”. Los Alamos National Laboratory LA-UR-07-5150. June 2014.

[14] D. J. Mercer. “Tomographic Gamma Scanner Experience:Three Cases”. Los Alamos National Laboratory. June 2014.

[15] D Stanga, D Radu, and O Sima. “A new model calculation of the peak efficiency for HPGe detectors used in assays of radioactive waste drums”. In: *Applied Radiation and Isotopes* 68.7-8 (2010), pp. 1418–1422.

[16] G. Yang, X.G. Tuo, and Z. Cheng. “The study of tomographic gamma ray scanning for nuclear waste drums”. In: *Nuclear Electronics and Detection Technology* 35 (2015), pp. 26–35.

[17] J. Eberth and J. Simpson. “From Ge(Li) detectors to gamma-ray tracking arrays–50 years of gamma spectroscopy with germanium detectors”. In: *Progress in Particle and Nuclear Physics* 60.2 (2008), pp. 283–337.

[18] R. D. Evans. *The Atomic Nucleus.* 2nd. New York: McGraw-Hill, 1955. Chap. 4, p. 972.

[19] Martin J Berger et al. “XCOM: Photon cross section database (version 1.2)”. In: *http://physics. nist. gov/xcom* (1999).

[20] T. Rades A. Müllertz Y. Perrie. *Analytical Techniques in the Pharmaceutical Sciences*. Ed. by M.J. Rathbone. Springer Nature, 2016, p. 34. ISBN: ISBN 978-1-4939-4029-5.

[21] C. D. Wagner et al. "NIST X-Ray Photoelectron Spectroscopy Database 1, Version 2". In: *Nat'l Std. Ref. Data Series (NIST NSRDS)-* (1997).

[22] A. Einstein. "Concerning an Heuristic Point of View Toward the Emission and Transformation of Light". In: *Ann. Phys* 17 (1905), p. 132.

[23] J. Hemingway G. Gilmore. *Practical Gamma-Ray Spectrometry*. 3rd. Chichester: John Wiley and Sons Ltd., 1998. Chap. 2, p. 314. ISBN: 0471951501.

[24] A. Thompson et al. *X-Ray Data Booklet*. 3rd. Berkeley: Lawrence Berkeley National Laboratory, 2009. Chap. 1, p. 176.

[25] W.N Cottingham and D.A. Greenwood. *An introduction to nuclear physics*. Cambridge University Press, 2001.

[26] Arthur H Compton. "A quantum theory of the scattering of X-rays by light elements". In: *Physical review* 21.5 (1923), p. 483.

[27] G. F. Knoll. *Radiation Detection and Modelling*. 4th. New York: Wiley, 2010. ISBN: 978-0-470-13148-0.

[28] R. D. Evans. *The Atomic Nucleus*. 3rd. New York: McGraw-Hill Book Company, Inc., 1955. Chap. 24, p. 228.

[29] Canberra Industries. *Mirion (Canberra) BE6530 HPGe Detector*. Mirion Technologies Inc. (Canberra). 2013.

[30] P.N. Luke et al. "IEEE Transactions on Nuclear Science NS-36". In: *IEEE Transactions on Nuclear Science NS-36*. 3rd ser. 1 (1989), p. 926.

[31] K. S. Krane. *Introductory Nuclear Physics*. 3rd. New York: John Wiley and Sons Inc., 1987. Chap. 4, p. 864. ISBN: 047180553X.

[32] C. Kittel. *Introduction to Solid State Physics*. 8th. New Jersey: John Wiley and Sons Inc., 2005. Chap. 17, p. 503. ISBN: 0-471-41526-X.

[33] P. Hofmann. *Solid state physics: an introduction*. John Wiley & Sons, 2015.

[34] W. R. Leo. *Techniques for Nuclear and Particle Physics Experiments*. 2nd. New York: Springer-Verlah, 1987. Chap. 2, p. 382. ISBN: 978-03-875-7280-2.

[35] A. Patel. "An Experimental Investigation to Assess the Feasibility of Imaging Medical Radioisotopes with the ProSPECTus Compton Camera". PhD thesis. University of Liverpool, Sept. 2016.

[36] E. Aguayo et al. "Characteristics of signals originating near the lithium-diffused N^+ contact of high purity germanium p-type point contact detectors". eng. In: *Nuclear Instruments and Methods in Physics Research, A* 701 (2013), pp. 176–185.

[37] Z. He. "Review of the Shockley-Ramo theorem and its application in semiconductor gamma-ray detectors". In: *Nuclear Instruments and Methods in Physics Research A* 250 (2001), p. 267.

[38] W. Schockley. "Currents to conductors induced by a moving point charge". In: *Journal of Applied Physics* 9 (1938), p. 635.

[39] S. Ramo. "Currents induced by electron motion". In: *Proceedings of the Institute of Radio Engineers* 27 (1939), p. 27.

[40] L.J. Harkness-Brennan et al. "An experimental characterisation of a Broad Energy Germanium detector". In: *Nuclear Instruments and Methods in Physics Research Section A: Accelerators, Spectrometers, Detectors and Associated Equipment* 760 (2014), pp. 28–39.

[41] H. Boston et al. "Characterisation of the SmartPET planar Germanium detectors". In: *Nuclear Instruments & Methods in Physics Research Section A: Accelerators Spectrometers Detectors and Associated Equipment* 579 (2007), p. 104.

[42] Caen S.P.A. "Caen Electronics". Caen S.P.A. Dec. 2017.

[43] Björn Lehnert. “Background rejection of n+ surface events in GERDA Phase II”. In: *Journal of Physics: Conference Series*. Vol. 718. 6. IOP Publishing. 2016, p. 062035.

[44] M. Salathe. “Computational studies of BEGe detectors”. In: *Verhandlungen der Deutschen Physikalischen Gesellschaft* (2013).

[45] B. Bruyneel, P. Reiter, and G. Pascovici. “Characterization of large volume HPGe detectors part 1: Electron and hole mobility parameterization”. In: *Nuclear Instruments & Methods in Physics Research Section A: Accelerators, Spectrometers, Detectors and Associated Equipment* 569 (2006), pp. 764–773.

[46] L Mihailescu et al. “The influence of anisotropic electron drift velocity on the signal shapes of closed-end HPGe detectors”. In: *Nuclear Instruments and Methods in Physics Research Section A: Accelerators, Spectrometers, Detectors and Associated Equipment* 447.3 (2000), pp. 350–360.

[47] W. L. Brown. “N-type surface conductivity on p-type germanium”. In: *Physical Review* 91 (1953), p. 518.

[48] D. Palioselitis. “Experience from operating germanium detectors in GERDA”. In: *Journal of Physics: Conference Series* 606 (2015), p. 8.

[49] W.H. Press et al. “Numerical recipes in C++”. In: *The art of scientific computing* (1992).

[50] Parker Sales Company UK. Online. http://ph.parker.com/gb/en/electric-linear-positioning-stages-and-tables. 2015.

[51] J. Cresswell and J. Sampson. *MTsort manual*. Department of Physics, University of Liverpool, 2016.

[52] A. Georgiev, W. Gast, and R.M. Lieder. “An analog-to-digital conversion based on a moving window deconvolution”. In: *IEEE Transactions on Nuclear Science* 41.4 (1994), pp. 1116–1124.

[53] L.J. Harkness-Brennan et al. “An experimental characterisation of a Broad Energy Germanium detector”. In: *Nuclear Instruments & Methods in Physics Research Section A: Accelerators Spectrometers Detectors and Associated Equipment* 760 (2014), pp. 28–39.

[54] A. S. Adekola. *Position-dependent pulse shape characterization of a BE6530 germanium detector*. Private communication. Mirion Technologies Inc. (Canberra), Meridien, CT, USA. Mirion Technologies Inc. (Canberra), Meridien, CT, USA, July 2016.

[55] L. A. Currie. “Limits for qualitative detection and quantitative determination. Application to radiochemistry”. In: *Analytical Chemistry* 40.3 (1968), pp. 586–593.

[56] T. J. Sumerling and S. C. Darby. *Statistical aspects of the interpretation of counting experiments designed to detect low levels of radioactivity*. Tech. rep. National Radiological Protection Board, 1981.

[57] L.P. Ekström S.Y.F. Chu and R.B. Firestone. “The Lund/LBNL Nuclear Data Search”. Lawrence Berkeley National Laboratory. Feb. 1999. URL: `http://nucleardata.nuclear.lu.se/toi/`.

[58] K. A. Stroud and D. J. Booth. *Engineering Mathematics*. Palgrave Macmillan, 2013.

Appendices

Appendix A

The Shockley-Ramo Theorem for Induced Charge

The electric potential and field in a semi-conductor detector are described by Poisson's equation:

$$\nabla^2 \varphi = \rho/\epsilon \tag{A.1}$$

where

φ is the electric potential

ρ is the charge density

ϵ is the dielectric constant for the detector crystal

However, in semiconductor detectors, the benefit of the application of a reverse bias means that there will be an absence of any trapped charges. Thus $\rho = 0$ and equation A

will reduce to the Laplace equation:

$$\nabla^2\varphi = 0 \tag{A.2}$$

In orthogonal coordinates, the Laplace operator can be defined as:

$$\nabla^2 = \frac{\delta^2}{\delta x^2} + \frac{\delta^2}{\delta y^2} + \frac{\delta^2}{\delta z^2}$$

We can also define the electric field at any point within a detector, $\mathscr{E}$, by taking the gradient of the electric potential at that point

$$\mathscr{E} = -\nabla\varphi \tag{A.3}$$

If an assumption that there is no diffusion within the detector then any charge carriers that are generated as a result of an interaction will follow the electric field lines from that point to the electrode. If a further assumption that the drift velocity of the charge carriers has reached a saturated level as mention above, then the position of the charge as a function of time can also be established [27].

A.1 Induced Charge

The Shockley-Ramo theorem ([38], [39]) can be used to calculate the induced charge on a collecting electrode as a result of the movement of charge carriers within a detector following an interaction. This induced charge, Q, is given by [27]:

$$Q = q\Delta\varphi_0 \tag{A.4}$$

where

q is the charge of the carrier

$\Delta\varphi_0$ is the difference in weighting potential

To demonstrate the application of the Shockley-Ramo theorem, a planar semiconductor detector is used, illustrated schematically in figure A.1.

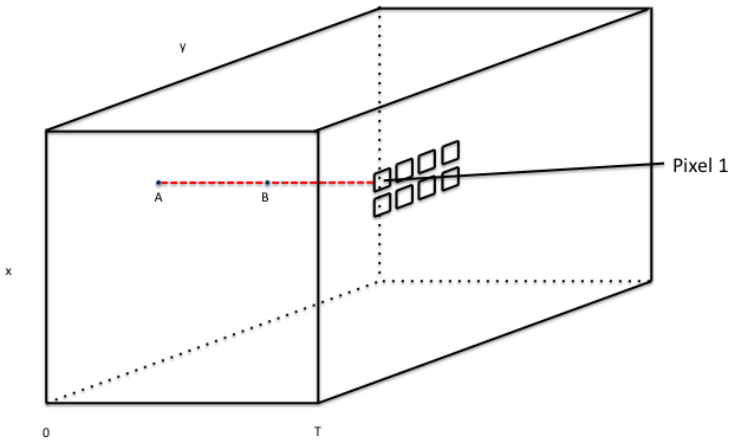

Figure A.1: Schematic of a planar semiconductor detector. The left hand x-y plane represents a continuous cathode whilst the right hand x-y plane is a pixelated anode (Only some of the pixels are shown)

An assumption is made that both holes and electrons contribute to the signal generated in the detector. For an interaction that takes place at point B, which lies on the axis of pixel 1, the weighting potential is defined as having a value of β ($0 < \beta < 1$). Since the electron in motion has a charge of

$$Q = -n_0 e \tag{A.5}$$

APPENDIX B

moving from B to the pixel we have

$$\Delta\varphi_0 = (1 - \beta) \tag{A.6}$$

and the electron contribution to the induced charge is

$$Q_e = -n_0 e(1 - \beta) \tag{A.7}$$

In contrast, the hole contribution is

$$Q_h = -n_0 e\beta \tag{A.8}$$

The total charge is achieved by combining both of these contributing elements,

$$Q_{Total} = Q_e + Q_h Q_{Total} = -n_0 e \tag{A.9}$$

From this it can be seen that the signal amplitude is independent of the location of the interaction.

APPENDIX B

Appendix B

Risetime maps used in DCSA development

The full collection of RM figures for the surface and bulk regions are given in this section.

They are included for interest and completeness.

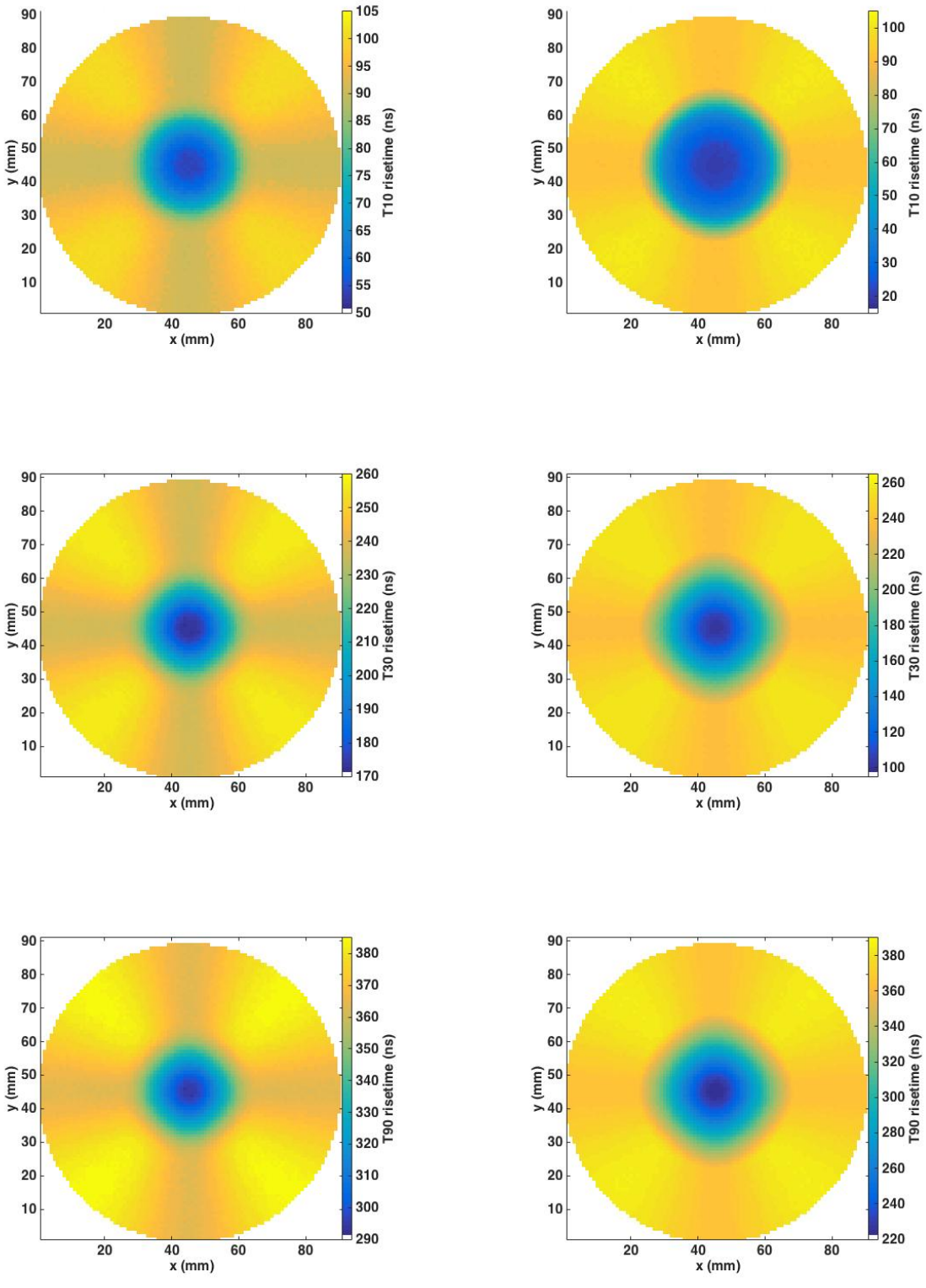

(a) (b)

Figure B.1: RM for $z =$ (a) 5.5 mm and (b) 20.5 mm relative to the point contact.

A range of threshold were used when applying the DCSA to investigate the effects of altering the threshold, the results together with the values used are shown in Figures B.2 to B.4 and Tables B.1 to B.3

Sub figure	**Threshold (ns)**
(a)	90
(b)	91
(c)	92
(d)	93
(e)	94
(f)	95
(g)	100

Table B.1: Thresholds used for T10

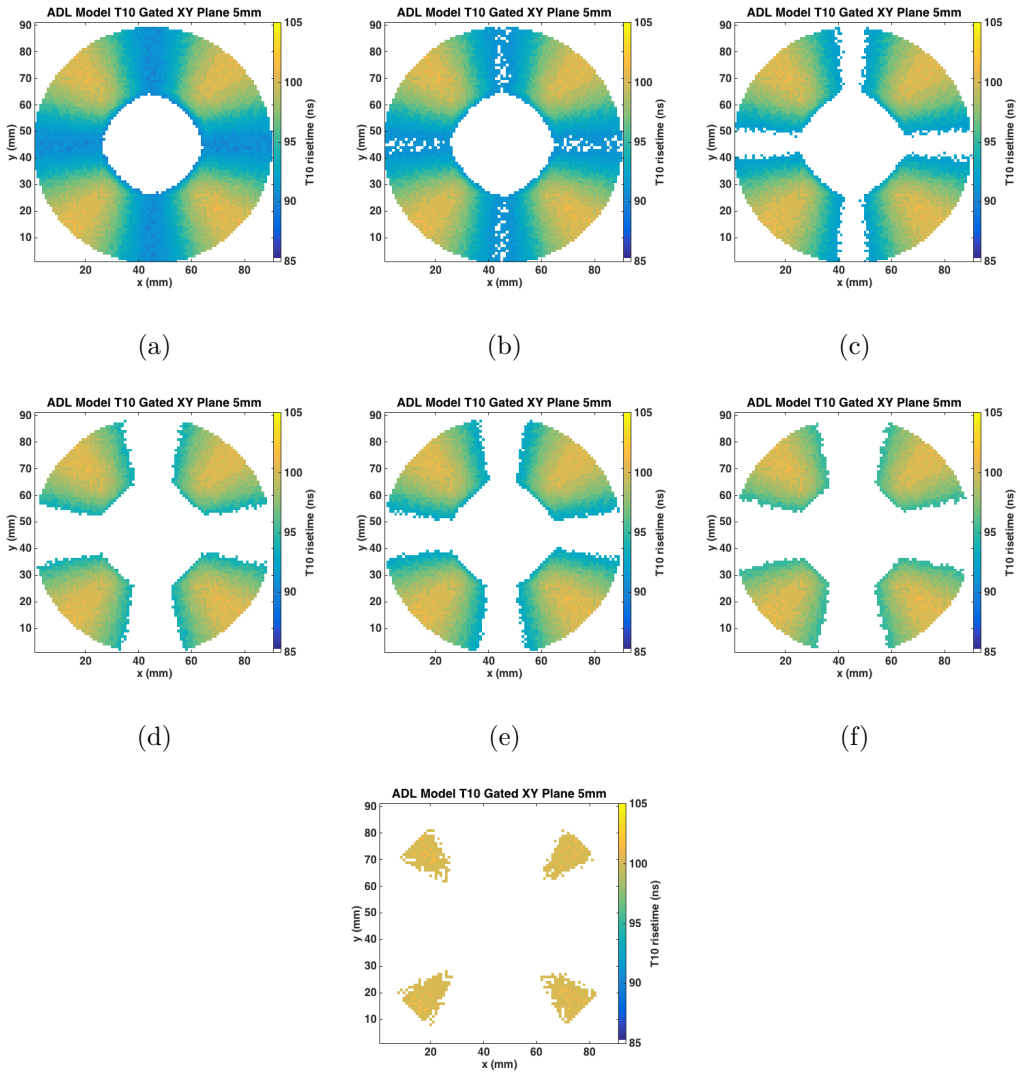

(a) (b) (c)

(d) (e) (f)

(g)

Figure B.2: RM for T10 using the DCSA with thresholds shown by run number in Table B.1.

Run Number	Threshold (ns)
1	225
2	245
3	235
4	230
5	233
6	238
7	237
8	236
9	235
10	235

Table B.2: Thresholds used for T30

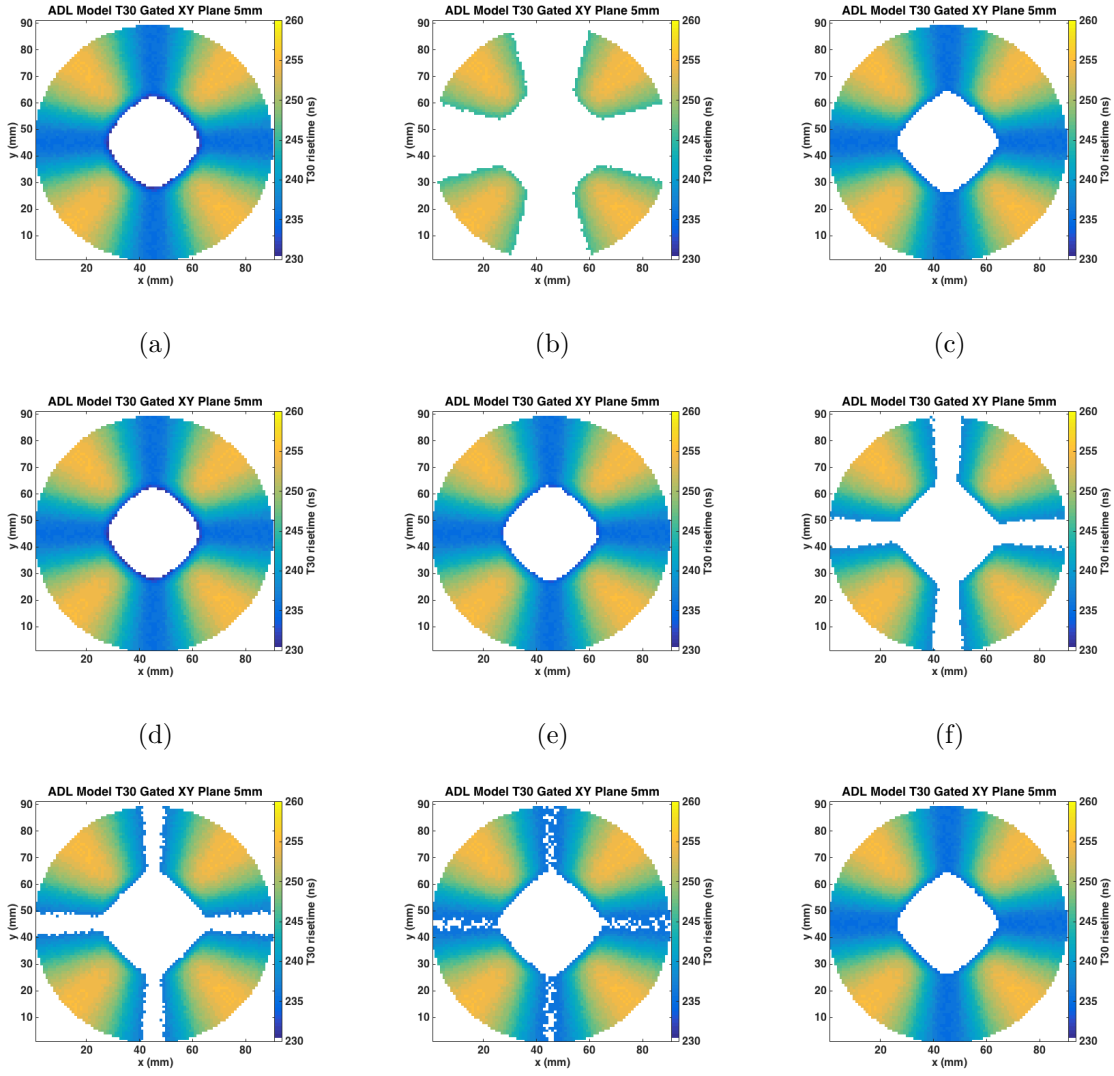

(a) (b) (c)

(d) (e) (f)

(g) (h) (i)

Figure B.3: RM for T30 using the DCSA thresholds shown by run number in Table B.2.

Run Number	Threshold (ns)
1	268
2	288
3	278
4	270
5	273
6	272
7	269
8	271
9	270.5
10	270

Table B.3: Thresholds used for T90

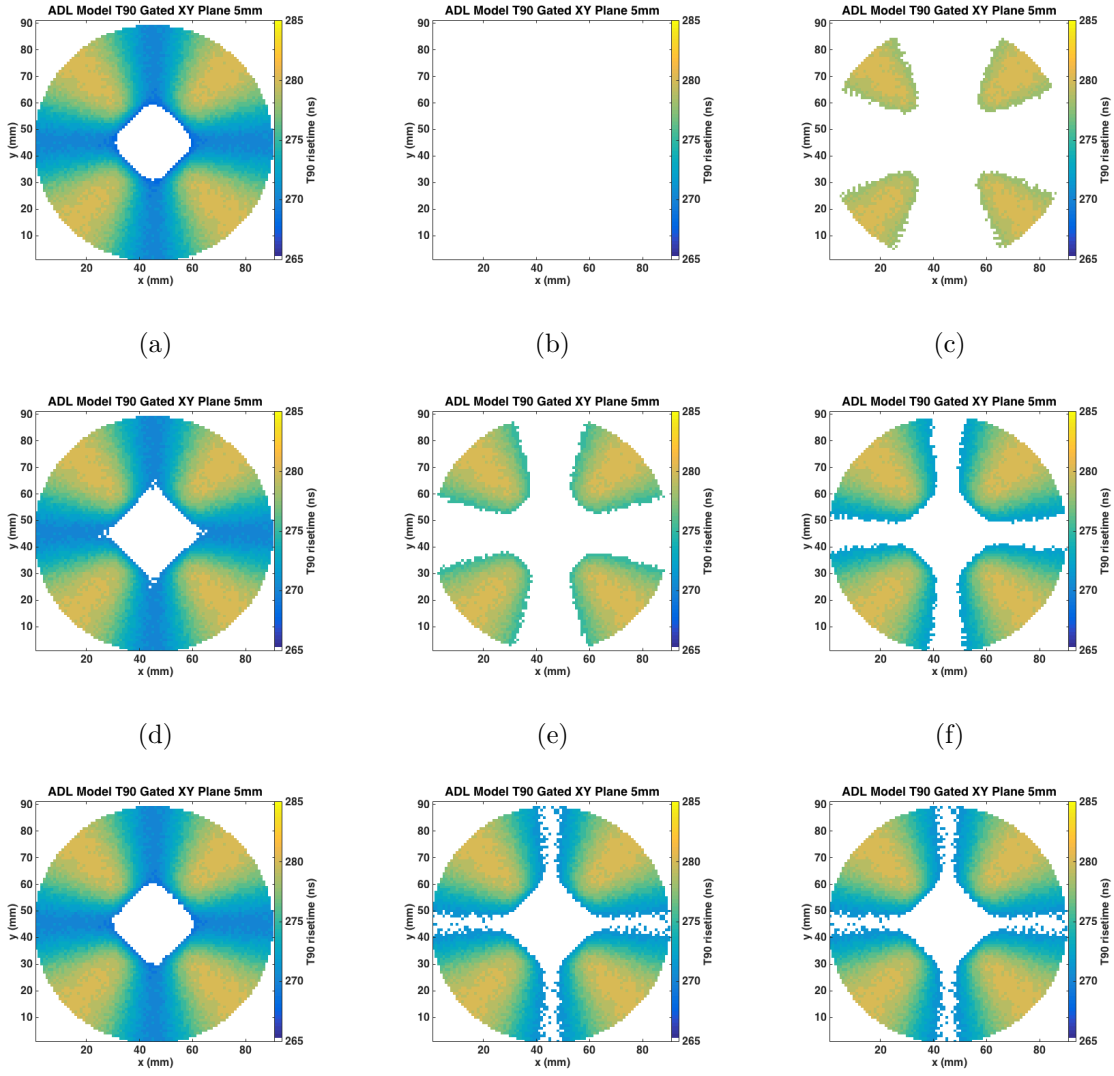

(a) (b) (c)

(d) (e) (f)

(g) (h) (i)

Figure B.4: RM for T90 using the DCSA thresholds shown by run number in Table B.3.

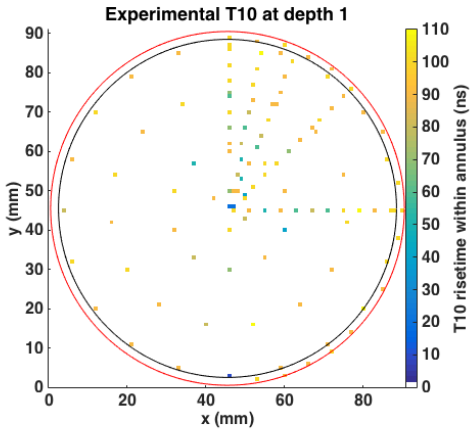

(a) Experimental T10 risetime intensity map at depth 1

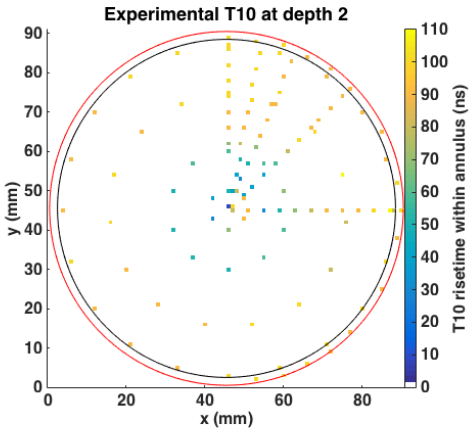

(b) Experimental T10 risetime intensity map at depth 2

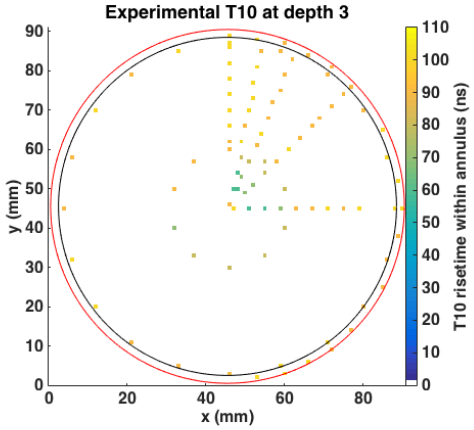

(c) Experimental T10 risetime intensity map at depth 3

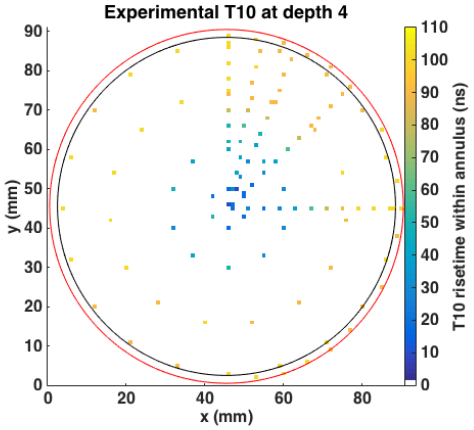

(d) Experimental T10 risetime intensity map at depth 4

Figure B.5: Experimental risetime intensity map for T10 at 4 depths relative to the contact.

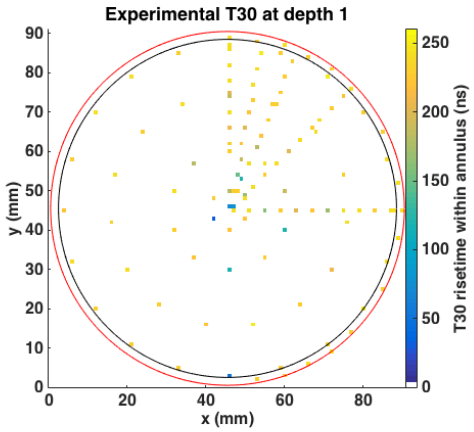

(a) Experimental T30 risetime map at depth 1

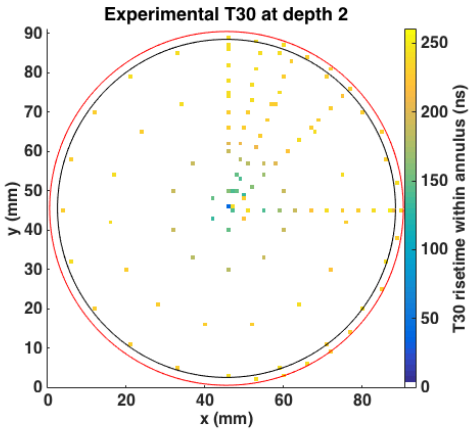

(b) Experimental T30 risetime map at depth 2

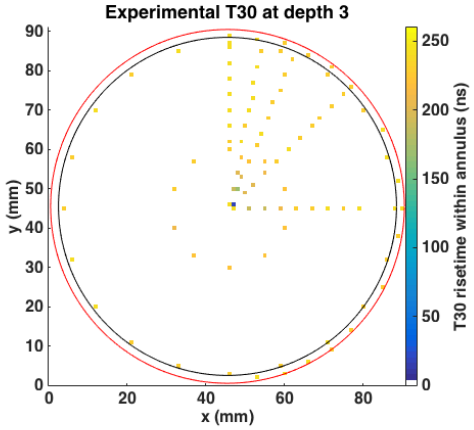

(c) Experimental T30 risetime map at depth 3

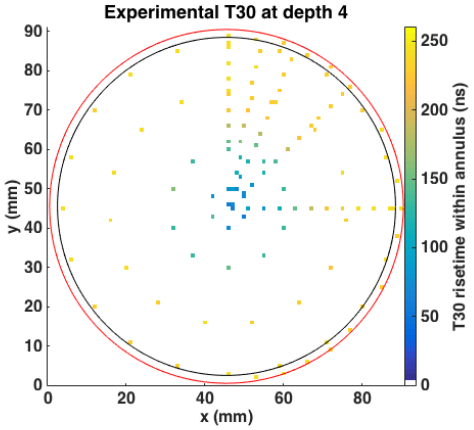

(d) Experimental T30 risetime map at depth 4

Figure B.6: Experimental Risetime map for T30 at 4 depths relative to the contact.

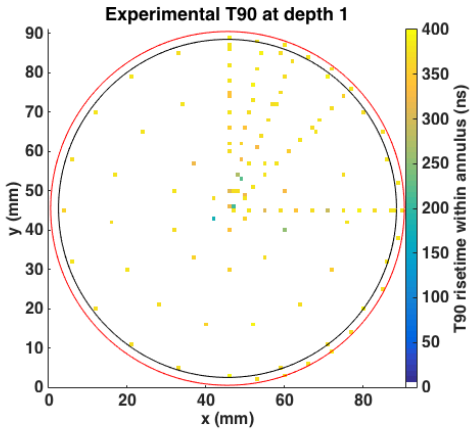

(a) Experimental T90 risetime map at depth 1

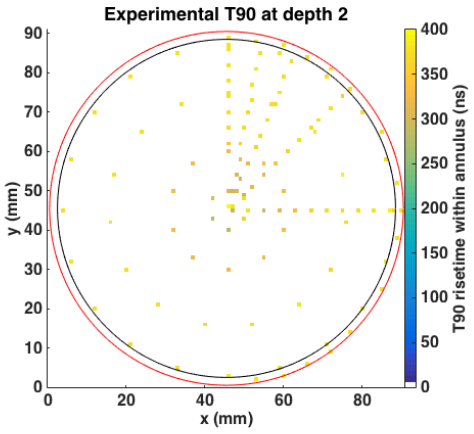

(b) Experimental T90 risetime map at depth 2

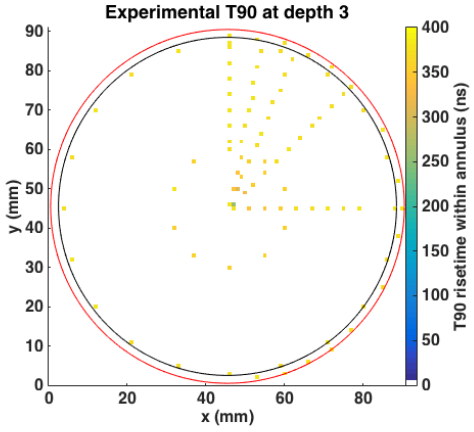

(c) Experimental T90 risetime map at depth 3

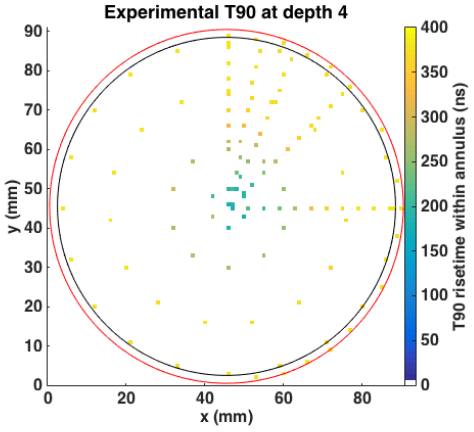

(d) Experimental T90 risetime map at depth 4

Figure B.7: Experimental risetime map for T90 at 4 depths relative to the contact.

To further explore the boundary between the surface and bulk regions, the average risetime as a function of the (r, z) position has been calculated for a variety of t_{min} and t_{max}. In these calculations, t_{min} has been varied between 1 and 4% whilst t_{max} has been varied from 10 to 90%. The average risetimes calculated at four different z slices are shown in Figures B.8 to B.11.

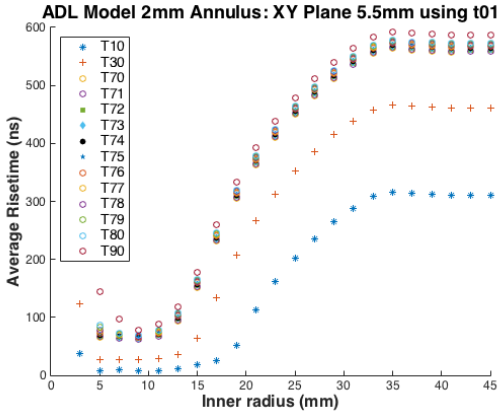

(a)

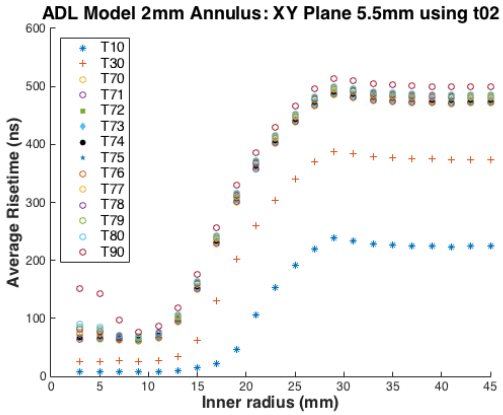

(b)

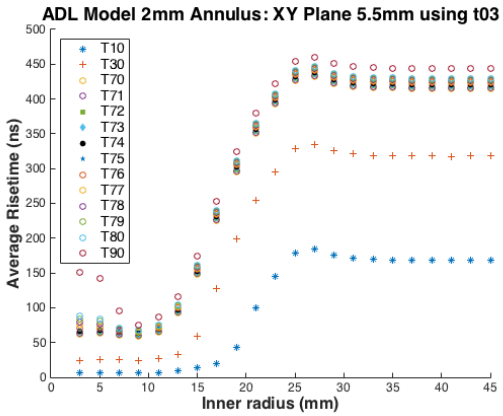

(c)

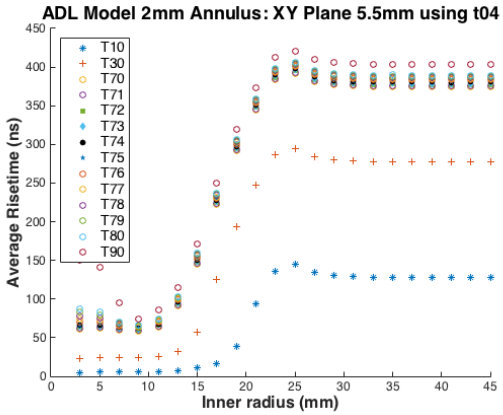

(d)

Figure B.8: Average risetimes at a height of 5.5 mm from the contact for t_{min} = (a) 1%, (b) 2%, (c) 3%, (d) 4%.

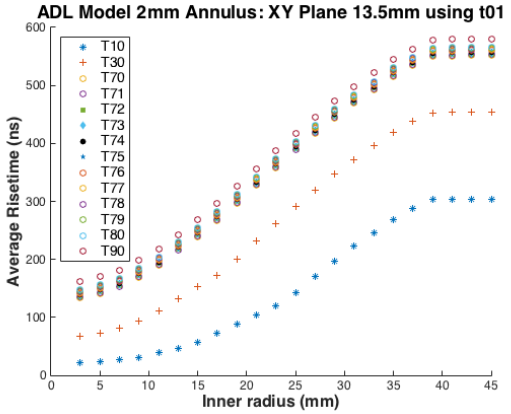

(a)

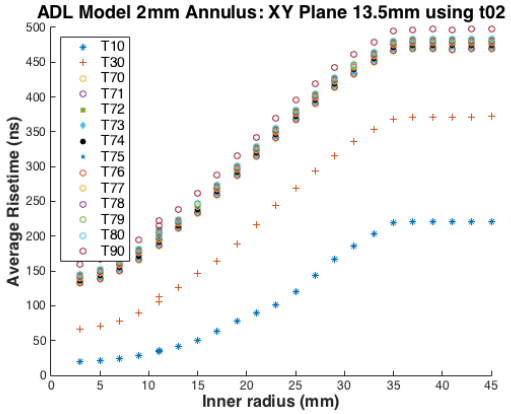

(b)

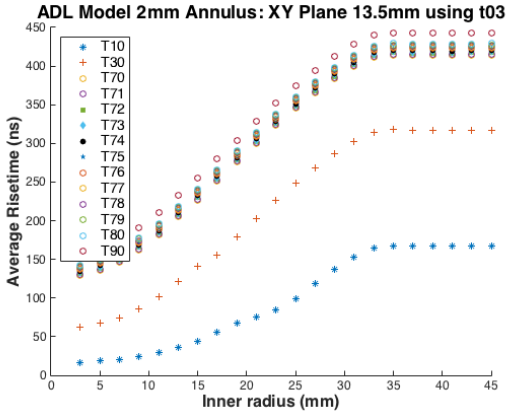

(c)

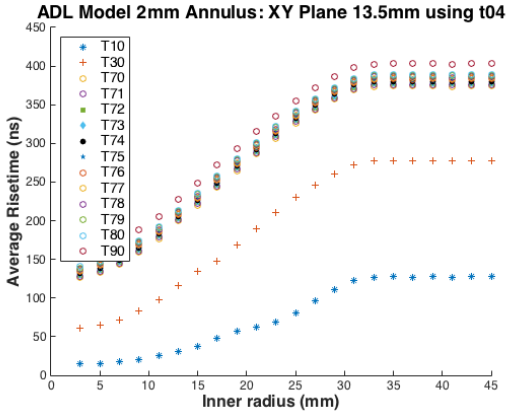

(d)

Figure B.9: Average risetimes at a height of 13.5 mm from the contact for t_{min} = (a) 1%, (b) 2%, (c) 3%, (d) 4%.

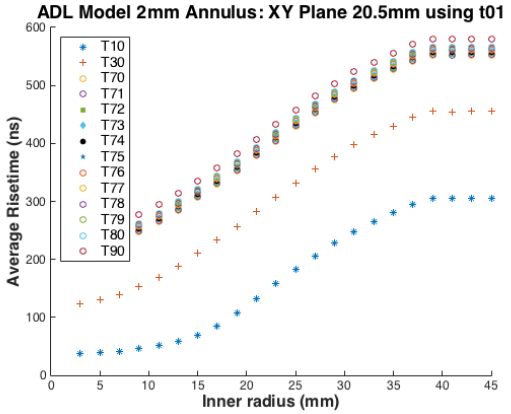

(a)

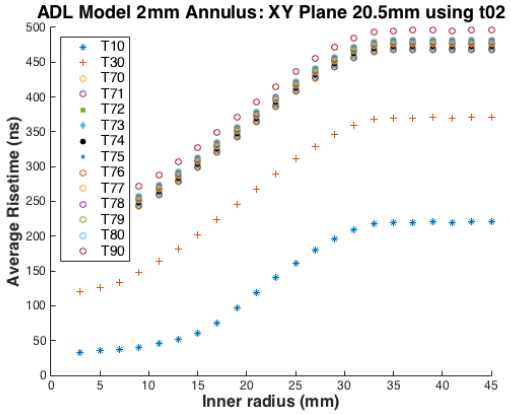

(b)

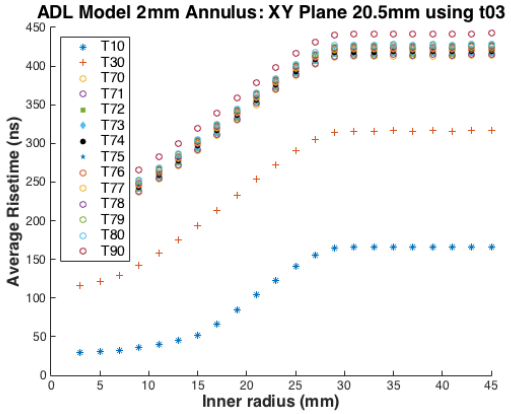

(c)

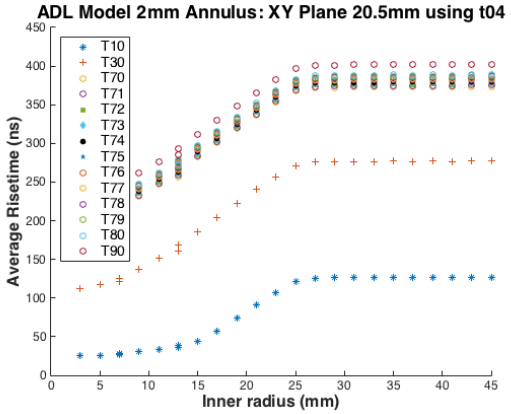

(d)

Figure B.10: Average risetimes at a height of 20.5 mm from the contact for t_{min} = (a) 1%, (b) 2%, (c) 3%, (d) 4%.

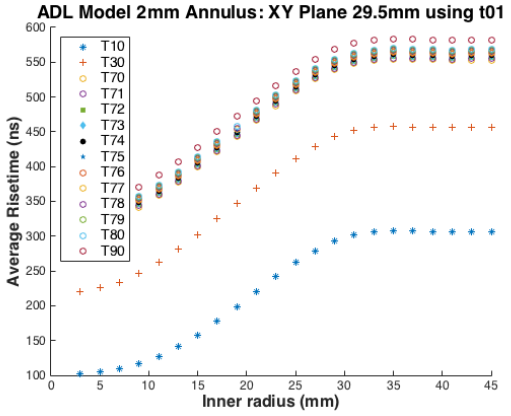

(a)

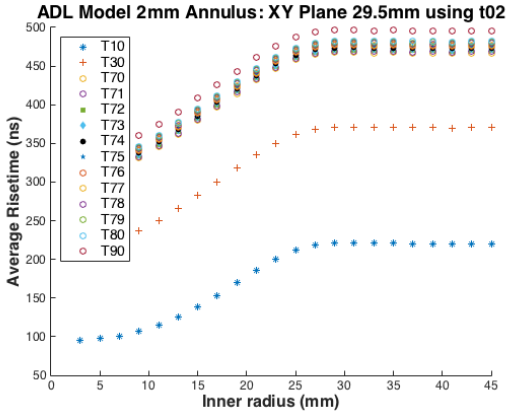

(b)

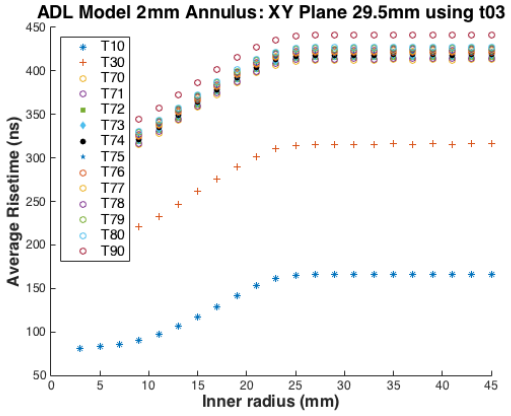

(c)

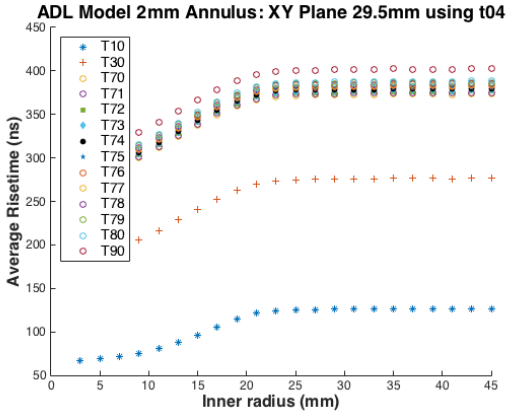

(d)

Figure B.11: Average risetimes at a height of 29.5 mm above the contact for t_{min} = (a) 1%, (b) 2%, (c) 3%, (d) 4%.

We can see that at a height of 5.5mm above the contact, the anomalous region is apparent in the plot for T90 for all of the t_{min} calculations and to a lesser extent for T79 and T80. There is also a trend, in all of the other heights, for the plots to rise to a maximum value and then plateau without the slight ridge that is apparent in the plots for 5.5 mm at a radius of approximately 25 mm. As discussed previously, this is attributable to the effects of the weighting field on the drift velocities of the charge carriers in the region above the point contact. The broadening of the region of change in the weighting potential gradient, with a corresponding increase in its distance from the point contact accounts for the smoother change between the rising slope of the remaining plots and the plateau regions. It is also noted that the start of the plateau region decreases as the value for t_{min} is reduced with the longest plateau region evident in the $t_{min} = 1\%$ plots. This would seem to suggest that the obvious choice for t_{min} would be 1%. However, as we shall see in the next chapters, this is not necessarily the case.